A SEARCH FOR WARM-HOT INTERGALACTIC MATTER IN THE LOCAL SHEET OF GALAXIES

RYAN DENEAULT

A THESIS SUBMITTED TO THE FACULTY OF GRADUATE STUDIES IN PARTIAL FULFILLMENT OF THE REQUIREMENTS FOR THE DEGREE OF MASTER OF SCIENCE

GRADUATE PROGRAM IN PHYSICS AND ASTRONOMY
YORK UNIVERSITY
TORONTO, ONTARIO

June 2015

Abstract

30-40% of all baryons in the Universe are thought to reside in the warm-hot intergalactic medium (WHIM) at temperatures in the range of 10^5-10^7 K. If the oxygen abundance is comparable to expectations, then OVI absorption from the WHIM associated with the Local Sheet of galaxies should have been detected in background sources observed by the Far-Ultraviolet Spectroscopic Explorer (FUSE). FUSE spectra of targets spanning the entire sky have been examined to distinguish the WHIM in the Sheet from other sources. These observations suggest that the Sun is offset from the plane of the Local Sheet WHIM, defining a theoretical framework against which the data was compared. By looking for a correlation of the OVI absorption equivalent widths with latitude and comparing the results to hydrodynamical simulations, strong constraints have been placed on the properties of the WHIM. With a hydrogen number density equal to that predicted by the simulations, the upper limit to the oxygen abundance for the WHIM in the Local Sheet must be $0.05 \pm 0.01\ Z_\odot$. If instead a metallicity of $0.1\ Z_\odot$ is adopted for the WHIM, the upper limit to the hydrogen number density must be 0.64 ± 0.02 times that predicted by the simulations.

Acknowledgements

I would like to extend a sincere and heartfelt thank you to my supervisor, Marshall McCall, for providing me with this opportunity. His unending enthusiasm is a breath of fresh air, rivaled only by his positivity and excitement to teach. Such positivity fostered an ideal learning environment for which I cannot even begin to express my gratitude.

I would also like to thank my office mates, Lewis Wei Lin, Jesse Rogerson, and George Conidis for their unending support, kindness, and friendship. I would like to thank Lewis for his constant support over the last two years, providing me with the inspiration I needed to complete my thesis in a timely manner. To Jesse, I would like to express both admiration and gratitude. Jesse has been an endless source of guidance and advice over the past two years, all while being one of the most pleasant people I have ever had the fortune of meeting. Finally, I would like to thank George for his friendship and support. Although I am very grateful for his support and guidance with regards to my thesis, I am most thankful to him for showing interest in me and my life outside of astronomy. Our conversations would allow me to escape an otherwise hard and frustrating day, and for that I cannot thank him enough.

Finally, I would like to thank my family and friends. Without their support and encouragement I would have never made it this far in my academic career. To the greatest mother in the world, thank you for always supporting me in everything that I do and for being on the receiving end of all of my frustrations while writing this thesis without ever expressing a single complaint. To my father, thank you for showing genuine interest in my work, for being someone that I could talk physics with outside of my office, and for your encouragement to pursue my academic career.

TABLE OF CONTENTS

LIST OF TABLES

LIST OF FIGURES

Chapter 1

Introduction

Thanks to the efforts of missions such as the Wilkinson Anisotropy Probe (WMAP) and, more recently, the Planck mission, we have been able to measure small temperature fluctuations in the cosmic microwave background (CMB) with ever-increasing precision. By measuring the anisotropy of these fluctuations, it has been possible to constrain the expected energy budget of the Universe. It is concluded that our Universe is composed of 69% dark energy, 26% dark matter, and 5% baryonic matter (Ade et al. 2013). Assuming that these values are correct, it would be reasonable to expect that this composition would be reflected in the nearby Universe as well, and so by extension it should be possible to use local observations to corroborate the Planck data.

The baryonic component of our Universe is readily observed through its electromagnetic interactions, and as such a large number of observations regarding the abundance of baryonic matter in our Universe have been made over time, spanning a large range of redshifts. When observing at large redshifts, early in the Universe's history, it has been found that the number of hydrogen atoms corresponding to the neutral hydrogen absorption lines produced by the

transition from their ground state to their first excited state (Lyα forest) can account for the majority of the baryons that are predicted by the CMB data. When looking at lower redshifts, however, we have only been able to observe half of the baryons that are predicted (Tripp et al. 2004). There is a seeming local discrepancy between the abundance of baryonic matter predicted by the Planck and WMAP missions and that which is observed. This is what is known as the missing baryon problem, and it is the focus of many studies in modern day astronomy.

Cosmological hydrodynamical simulations indicate that there are four possible phases in which the baryons may reside (Davé et al. 2001). They are: a diffuse phase, with overdensity $\delta \equiv \frac{\rho}{\bar{\rho}}$<1000 (where $\bar{\rho}$ is the mean baryonic density) and temperature T<10^5 K; a condensed phase, with overdensity δ >1000 and temperature T<10^5 K; a warm-hot phase, with temperature 10^5<T<10^7 K; and a hot phase with temperature T>10^7 K. Davé et al. (2001) make use of six simulations of randomly selected volumes in a Universe dominated by cold-dark matter and a non-zero cosmological constant and arrive at a time-dependent baryonic composition for our Universe. Figure 1.1 shows the results for 4 of these simulations, from which it can be seen that at larger redshifts the baryonic constituents are primarily diffuse, as is observed in the Lyα forest, while at lower redshifts the warm-hot component dominates with an abundance of 30-40% of the total number of baryons.

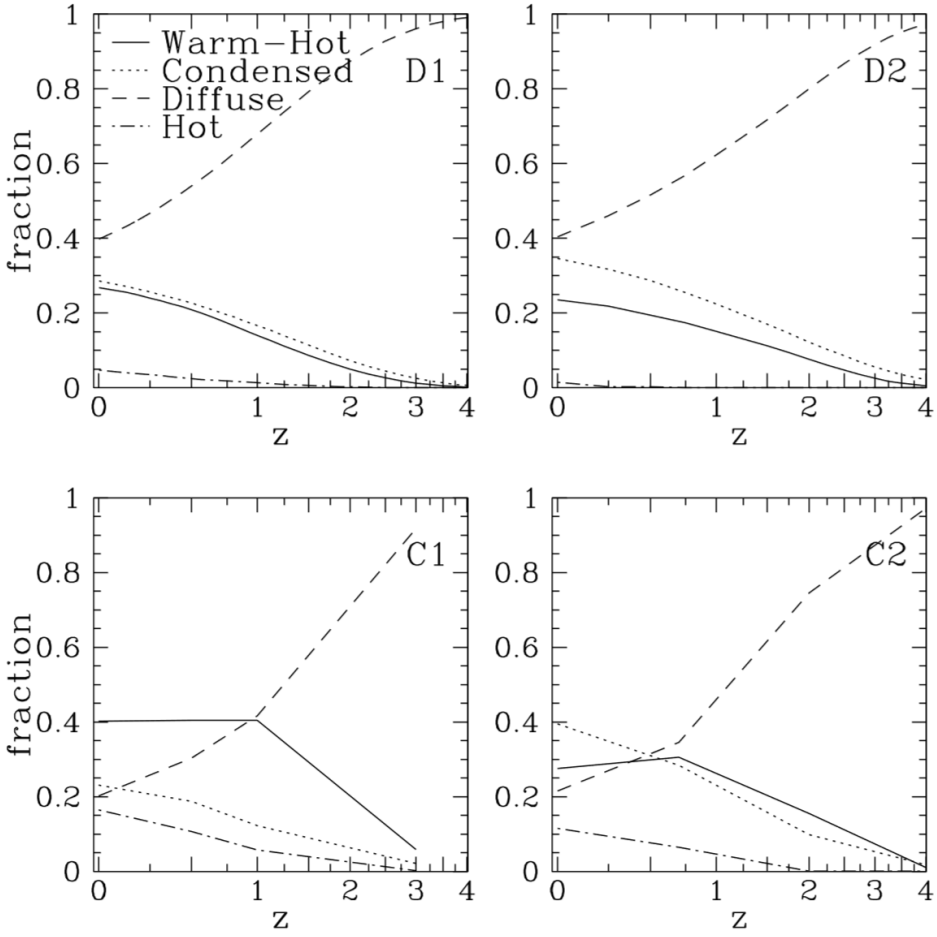

Figure 1.1: Four simulations showing the evolution of the four baryonic phases and their mass fraction as a function of redshift, taken from Davé et al. (2001).

The condensed, diffuse, and hot phases are seen in photoionized intergalactic gas (Lyα absorption), stars and cool galactic gas, and gas in galaxy clusters and large groups, respectively, and are all observed at the predicted abundancies. Warm-hot phase gas predicted to reside in the intergalactic medium, on the other hand, has not been observed at the predicted abundance likely due to difficulties in detecting it.

Simulations suggest that the warm-hot phase formed as a result of infalling diffuse gas during the early phases of structure formation in our Universe. At that time, baryons fell into the large gravitational potential wells of galactic struuctures, being shock heated to extreme temperatures

as they sped up and collided with other particles (Davé et al. 2001). Thus, the missing baryons in the local Universe are likely in the warm-hot phase. The simulations done by Davé et al. (2001) additionally suggest that the majority of the warm-hot phase baryons (70-90%) reside in the intergalactic medium, away from virialized groups such as galaxies and clusters. For this reason, the warm-hot phase baryons will be referred to as the warm-hot intergalactic medium (WHIM) for the remainder of this work.

Due to its high temperature, the WHIM is best observed in the far ultraviolet and low energy x-ray spectral regions. There have not been any other telescopes throughout history that have been able to observe this region of the electromagnetic spectrum at such a high resolution and so there is a relative lack of quality data with regards to the WHIM. For this reason, from an observational standpoint, we do not have a strong understanding as to how many baryons there are contained within the WHIM. Missing baryons may well be located in the WHIM but have yet to be observed or identified.

By the very nature of its formation, the WHIM must follow large-scale structure in our local Universe. By looking for relationships between structure and the presence of the WHIM, it should be possible to identify evidence for the WHIM that may have otherwise been missed, simply because the observers were not looking for this underlying relationship. Currently, most research involving the search for warm-hot gas is focused either on the warm-hot gas associated with the Milky Way and other galaxies (eg., Wakker et al. 2003; Semach et al. 2003, and references therein), or on very large structures such as the Sculptor Wall (Buote et al. 2009). Structure at intermediate scales has been relatively unexplored. This is likely because, at the time, there was no well-defined structure smaller than the Local Supercluster known in which to look for the WHIM.

Recently, it was discovered that out to a distance of about 6 Mpc, all bright galaxies including the Milky Way are confined to a pancake-like structure known as the Local Sheet. Based upon

the standard deviation of the positions of giants vertically, the thickness of the Sheet is only 465 kpc (see Figure 1.2). The Local Sheet is the nearest example of structure in our Universe. It was not really recognized as an entity until 2008 (Tully, et al. 2008), and it was not until 2014 that its geometry was characterized (McCall 2014). Consequently, no search for WHIM in the Local Sheet has been done yet. The structure of the Local Sheet offers a unique opportunity in which to search for the WHIM. Being so thin, a strong latitudinal dependence on the column density of WHIM gas would be expected, which opens up a new avenue in which to seek it. If the WHIM is found to trace the Local Sheet, it would be a breakthrough in locating the missing baryons of the Universe, and would serve to better our understanding of the behaviour of the WHIM throughout the Universe. Table 1.1 presents parameters describing the geometric properties of the Local Sheet relevant to this work.

Table 1.1: Geometric properties of the Local Sheet Adopted from McCall (2014).

Parameter	Value	Units
Thickness[1]	0.456	Mpc
Diameter[2]	10.4	Mpc
(x,y,z) Position of Sun with Respect to the Adopted Centre of the Local Sheet[3]	(-0.36,-0.72,+0.13)[4]	Mpc

1) This thickness is twice the vertical standard deviation of the positions of the giants about the plane.

2) This is the diameter of the Council of Giants, which may be smaller than the Local Sheet by up to 4Mpc if dwarf members are accommodated.

3) The adopted centre of the Local Sheet is taken to be the centre of the Council of Giants.

4) The (x,y,z) position of the Sun given in rotated Sheet coordinates. The defining features of the rotated Sheet coordinate system are that its origin coincides with the centre of the Council of Giants, with a North pole at the supergalactic position (L,B)=(241.74^o±0.74^o,82.05^o±0.12^o), and an x-axis rotated by 106.74^o with respect to its non-rotated position in which x-axis parallel to the line of nodes (the intersection between the Sheet plane and the supergalactic plane) along L=151.74^o.

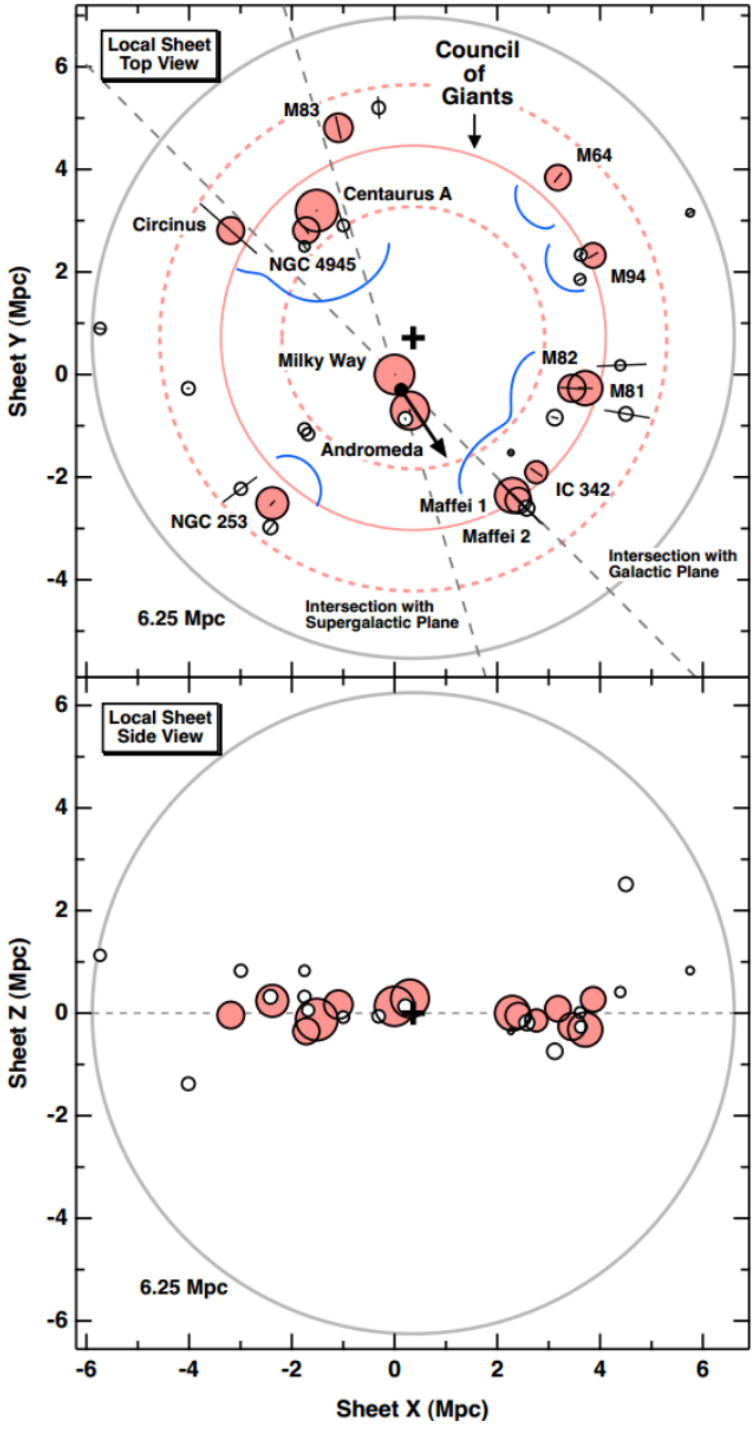

Figure 1.2: Spatial distribution of bright galaxies out to 6.25 Mpc from the centre of the Council of Giants, taken from McCall (2014).

The WHIM is composed primarily of hydrogen and helium gas left over from the Big Bang, but it is also enriched in heavier elements stripped from galaxies as they move through the

intergalactic medium, expelled by galactic winds, or injected into the WHIM from supernova explosions. Currently, the best way to detect the WHIM is through the five-times-ionized oxygen (O^{5+}) doublet at wavelengths 1031.926 Å and 1037.617 Å, which is visible in absorption against background continuum sources. The transition that produces these lines is the $2s^2S\text{-}2p^2P^o$ transition from the ground state of the ion, as can be seen in the Grotrian diagram in Figure 1.3. The O^{5+} ion is dominant for temperatures on the order of $3x10^5$ K (Wakker et al. 2003) and thus, the OVI absorption lines are a strong indicator of the WHIM in that temperature range.

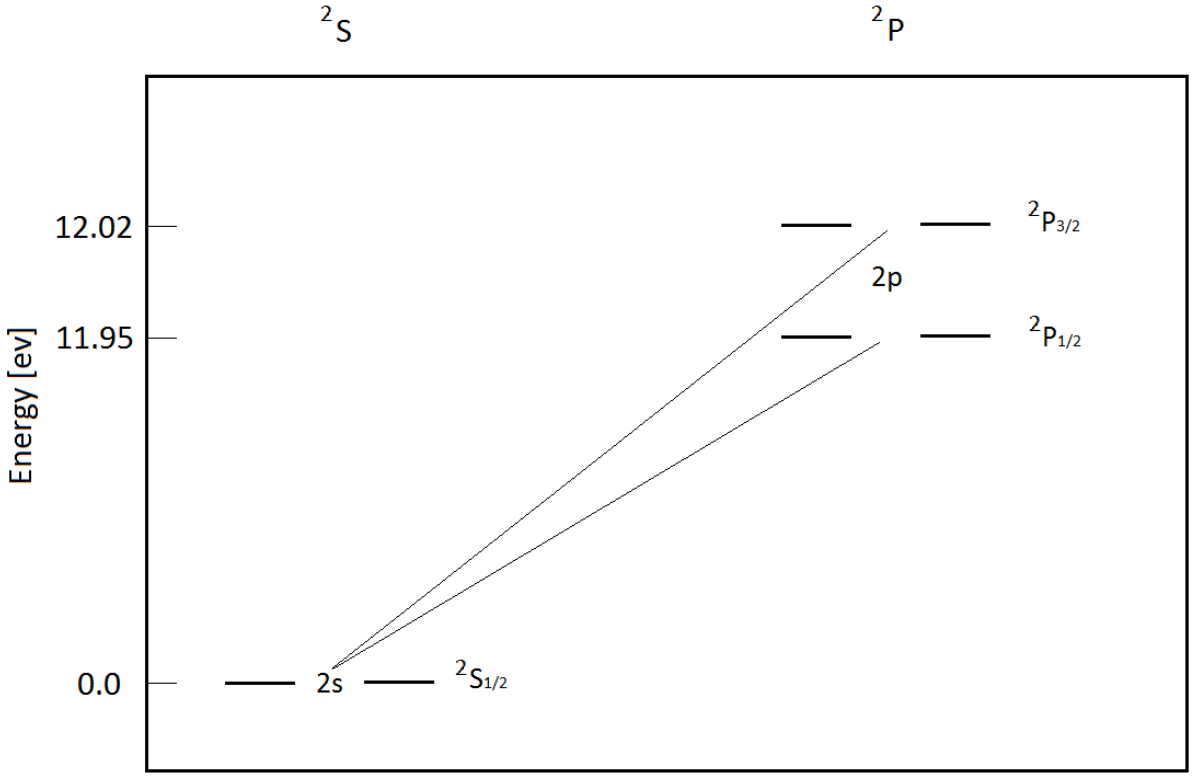

Figure 1.3: Grotrian diagram of the $2s^2S\text{-}2p^2P^o$ absorption doublet transition for OVI gas. Not to scale.

In order to probe the O^{5+} content and, by extension, the WHIM of the Local Sheet, quasars and distant galaxies can be used as background light sources. As the light from a distant target passes through the Local Sheet, any O^{5+} gas along the line of sight will remove flux from the beam in a manner that is dependent on the amount of gas along that particular line of sight.

The extent to which light is absorbed by the gas is described by

$$I_\lambda = I_{o\lambda} \exp[-\tau_\lambda] \quad [1.1]$$

where I_λ is the radiance of the electromagnetic radiation after it is absorbed by the intervening medium, $I_{o\lambda}$ is the initial radiance of the source, and τ_λ is the optical depth at wavelength λ. The wavelength dependence of the absorption is described by the wavelength dependence of the optical depth. What is most important for quantifying the column density of absorbing material is the equivalent width. The equivalent width, W, is defined as the width of a rectangle extending from the continuum down to zero radiance which covers the same amount of flux as the absorption line itself, specifically.

$$W = \int \left(1 - \frac{I_\lambda}{I_{o\lambda}}\right) d\lambda \quad [1.2]$$

Where I_λ is the radiance at λ.

It is expected that the WHIM associated with the Local Sheet follows the same pancake-like structure as the Sheet, and as such any observations at low latitudes above the plane of the Local Sheet should traverse more of the WHIM than at higher latitudes, resulting in larger equivalent widths. It is this relationship between the equivalent widths of the lines and the latitude of the targets with respect to the plane of the Local Sheet which allows one to constrain the amount of WHIM associated with the Sheet. If the WHIM were found to trace out the Local Sheet, there would be a means to identify other Sheet like structures in our Universe, constraining the amount of WHIM present within those systems as well.

Of particular benefit to searching for the WHIM in the Local Sheet is our location. Figure 1.2 shows that the Milky Way is situated near the centre, as is defined by the surrounding giants. From our vantage point, the Sheet traverses the entire sky, providing us with the maximum

amount of viewing angle possible over which to make the observations required to identify the WHIM.

In what follows, the selection criteria, processing, and analysis of background sources will be thoroughly explained. The relationships between these data and the structure of the Local Sheet will be explored in detail in an effort to better our understanding of the WHIM in our local Universe and, by extension, the missing baryon problem.

Chapter 2 begins by outlining the expected behaviour of the equivalent width with respect to the Sheet latitude on the basis of hydrodynamical simulations of Sheet-like objects. From there, it continues on to explore the consequences that the Hubble flow has on the predicted shape of the OVI absorption lines. With the observables indicative of the WHIM associated with a sheet well defined, the two following chapters are dedicated to the description of how the observations required in identifying the WHIM were made. Chapter 3 introduces the Far Ultraviolet Spectroscopic Explorer (FUSE) as the instrument of choice for the observational data, while Chapter 4 deals with the processing of the FUSE data and the removal of contamination sources. The analysis of the fully processed data is dealt with in Chapter 5, where the results of the observations are compared to the theoretical predictions of Chapter 2. A summary of the work and the results are given in the final chapter, Chapter 6. Concluding remarks as well as a statement of future work pertaining to the thesis are presented here as well.

Chapter 2

Theoretical Expectations

2.1 Equivalent Width as a Function of Heliocentric Sheet Latitude

Before going about the data selection and analysis, it is important to first get a better understanding of the expected relationship between the equivalent widths of the OVI absorption lines and the latitude above the plane of the Local Sheet at which the background probes are being observed. To accomplish this goal, one must first understand how the O^{5+} gas is distributed perpendicularly to the plane of the Local Sheet.

The presence and abundance of O^{5+} gas is dependent on the temperature of the gas, the number density of hydrogen, the oxygen abundance, and the fraction of oxygen which is five times ionized. Temperature and hydrogen number density profiles were obtained from the work done by Klar and Mücket (2010), who used hydrodynamical simulations to predict the WHIM distribution around galactic sheet structures at a redshift of zero. For one-dimensional collapse (which produces a sheet-like structure), the temperature and density profiles along the collapse direction were calculated for a wide variety of initial perturbation length scales, L, which is the

horizontal size of the sheet-like structure that is produced as a result of the initial perturbation in the Cosmic Microwave Background (CMB). Radiative cooling, heating due to a UV background, and thermal conduction effects were taken into account in the calculation of these profiles, allowing for an accurate representation of WHIM as it pertains to a sheet-like structure.

In a follow up paper (Klar and Mücket, 2012), Klar and Mücket extend their simulations to three dimensions, resulting in structures consisting of sheets, filaments, and gaseous halos. In reality, the structures observed are dependent on the initial conditions of their formation. For one-dimensional collapse, the orientation of the sheets is determined by the highest eigenvalue of the deformation tensor (Klar and Mücket, 2010). The probability that more than one of the initial eigenvalues are nearly equal to one another is extremely low and so therefore it is less likely that two or three dimensional collapse will occur over one-dimensional collapse (Doroshkevich and Shandarin, 1978). The distribution of galaxies in the Local Sheet does not seem to suggest the existence of filaments or a halo, but is completely indicative of the sheet structure produced by the one-dimensional collapse from Klar and Mücket (2010). Thus the results of the one-dimensional collapse simulations will be used to model the Local Sheet for the remainder of the thesis.

Since the size of the Local Sheet is not precisely established, two length scales were adopted in the calculations that follow in an effort to best represent the range of possible O^{5+} number density profiles that could describe the Local Sheet in reality. A lower limit to the Sheet diameter is given by McCall (2014), having a value of roughly 11 Mpc, while the upper limit to the Sheet diameter is given by Tully et al. (2008), with a value of 14 Mpc. Values of L given by Klar and Mücket (2010) are in units of Mpc/h, where h is the Hubble parameter, $\mathrm{H_o}/(100\ \mathrm{km\ s^{-1}Mpc^{-1}})$, for a Hubble constant $\mathrm{H_o}$. A Hubble parameter value of 0.716 ± 0.029 was used in accordance with the distance scale adopted by McCall (2014) for describing the Local Sheet, which is founded on the latest nuclear maser distance to NGC4258 (Riess et al. 2011, 2012; Humphreys

et al. 2013). The reason for using nearby galaxies rather than WMAP or Planck to establish h is because we are concerned with the possibility that the local expansion rate may be different than the average on large scales, which has been measured to be $h = 0.673 \pm 0.012$ (Ade et al. 2014).

Sheets with $L = 8$ Mpc/h and $L = 10$ Mpc/h were utilized, which correspond to 11.2 Mpc and 14.0 Mpc respectively, close to the lower and upper limits observed for the Local Sheet. These will be referred to as the 11 Mpc and 14 Mpc Sheets throughout this Thesis. Figures 2.1 and 2.2 show the vertical temperature and hydrogen number density profiles for each Sheet.

The temperature profiles from Figure 2.1 have three distinct regions: the inner isothermal core, a shocked region of higher temperature, and an outer region at low density and temperature. The shock region is produced as the infall velocity of the collapsing gas reaches the speed of sound, at which point faster moving gas begins to take over slower moving gas, converting kinetic energy into heat energy and creating a discontinuous change in density, velocity, and temperature. The increase in density brought upon by the shock can be seen in Figure 2.2. It is found that the size of the shocked region is directly proportional to L, as can be seen in Figures 2.1 and 2.2.

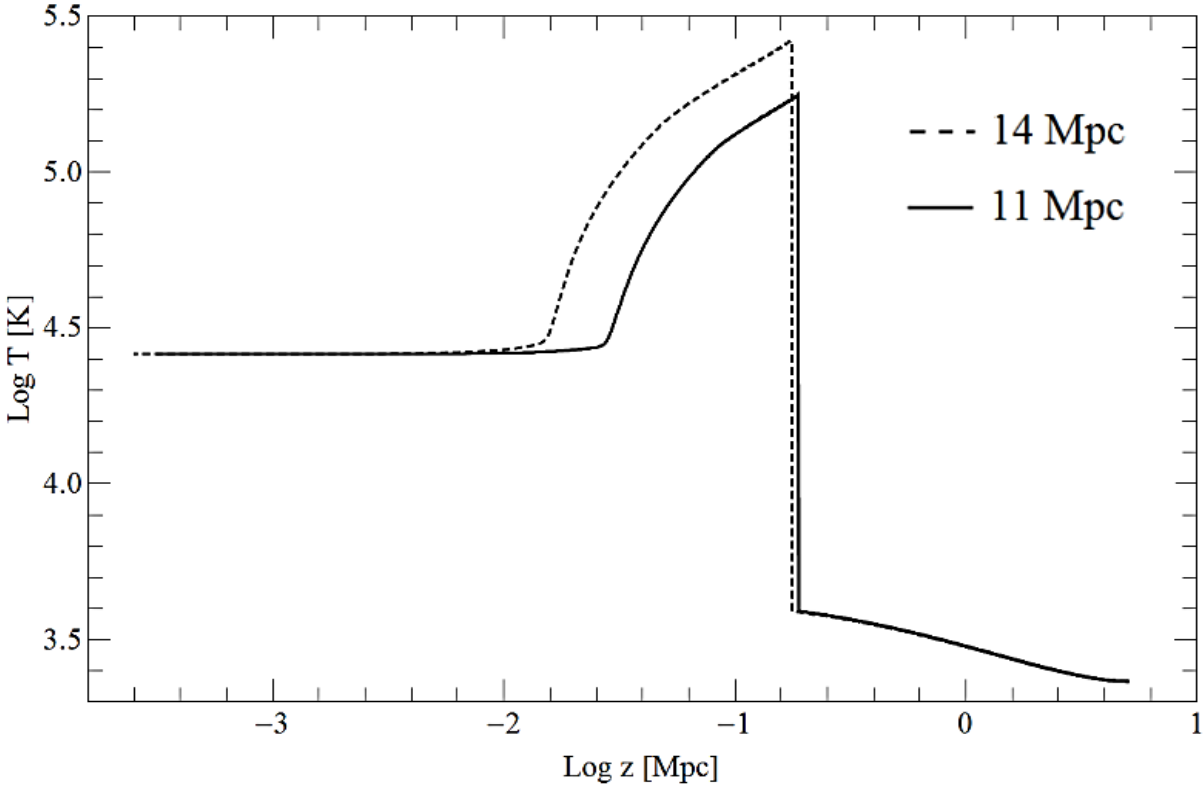

Figure 2.1: Vertical temperature profiles for initial perturbation length scales, L, of 11 and 14 Mpc.

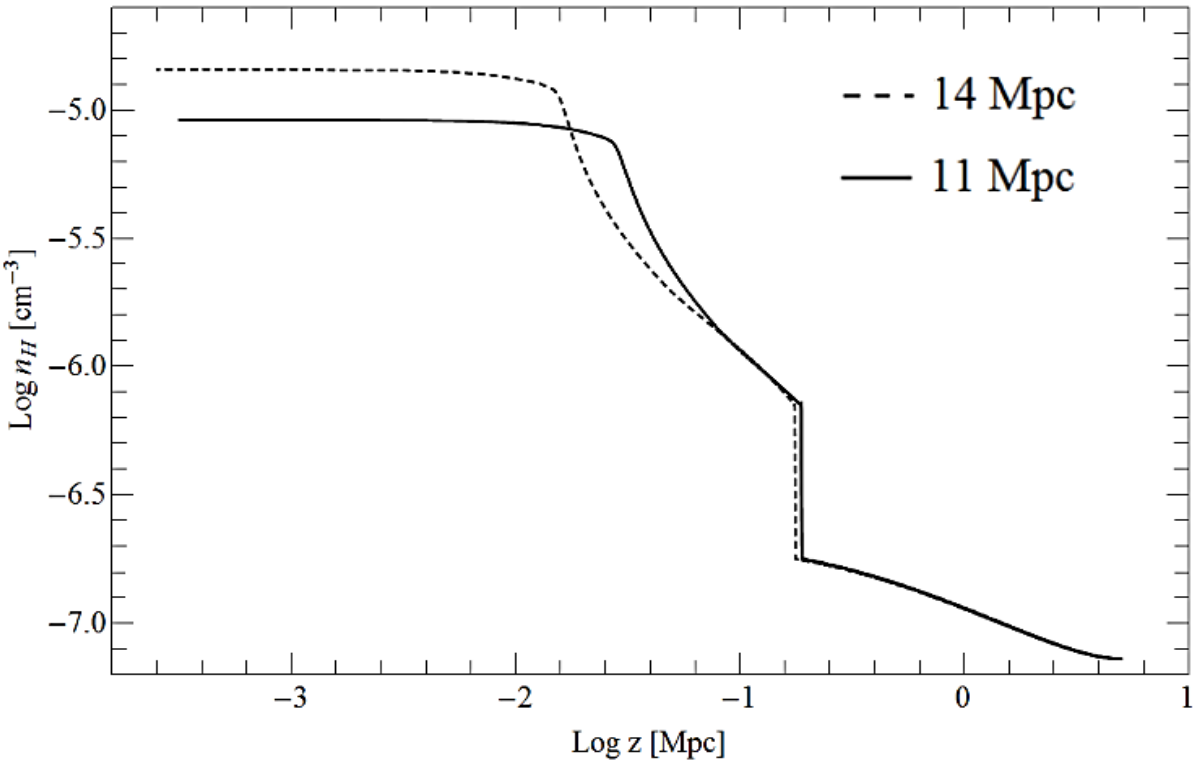

Figure 2.2: Vertical hydrogen number density profiles for initial perturbation length scales, L, of 11 and 14 Mpc.

The ultimate goal is to determine how the equivalent widths of OVI absorption lines are dependent on the latitude above the plane of the Local Sheet at which they are observed in background sources, and as such it is important to know how many OVI absorbers there are along any given line of sight. In order to do this, the O^{5+} number density profile has to be determined. The first step necessary to construct this profile is to convert the hydrogen number density profile into an oxygen number density profile. In order to do so, the hydrogen number density profile was simply scaled by the expected oxygen fraction of the WHIM, which is related to its metallicity. The metallicity is the percentage by mass of matter which is not hydrogen or helium. While it is unknown what the exact metallicity of the WHIM is, there is a consensus that the value is somewhere around $0.1Z_{\odot}$ (Danforth and Shull, 2005; Cen and Ostriker, 2006; Shull et al. 2012), where $Z_{\odot}$ is the solar metallicity. Although an assumption as to the metallicity of

the WHIM is being made here, this value is only a place holder since the eventual goal is to be able to compare the theoretical results to the results obtained from the observational data from FUSE. When that comparison is done, it will be possible to go back and constrain the metallicity of the WHIM that would be required in order to reproduce the observational results.

In order to evaluate the proportion of atoms which are oxygen from the metallicity, it is necessary to know the abundance of oxygen in the Sun. The logarithmic abundance, $\log \varepsilon_x$, of any element x is defined by

$$\log \varepsilon_x = \log\left(\frac{n_x}{n_H}\right) + 12 \qquad [2.1]$$

Where n_x and n_H are the number densities of x and hydrogen respectively. The solar logarithmic abundance of oxygen is 8.69 ± 0.05 (Asplund et al. 2009). The number density ratio of the Sheet relative to the Sun and the mass density ratio of the Sheet relative to the Sun are related via the hydrogen mass fraction of the Sheet relative to the Sun, $X/X_\odot$. Equation 2.2 expresses this relation:

$$\frac{n_O/n_H}{[n_O/n_H]_\odot} = \frac{\rho_M/\rho}{[\rho_M/\rho]_\odot}\frac{X}{X_\odot} = 0.1\frac{X}{X_\odot} \qquad [2.2]$$

where n_O is the number density of oxygen, ρ_M is the mass density of all metals, and ρ is the total mass density. Note that it has been approximated that $(\rho_O/\rho)/(\rho_O/\rho)_\odot = (\rho_M/\rho)/(\rho_M/\rho)_\odot$, i.e., that the mass density of oxygen scales with that of all metals. The $X/X_\odot$ ratio is very close to one due to the large number density of hydrogen with respect to the metals, thus the number density profile for oxygen follows from equation 2.1 and the metallicity of the Sheet relative to the Sun.

$$n_O = 0.1 n_H 10^{[log\varepsilon_O]_\odot - 12} \quad [2.3]$$

Plots are given in Figure 2.3.

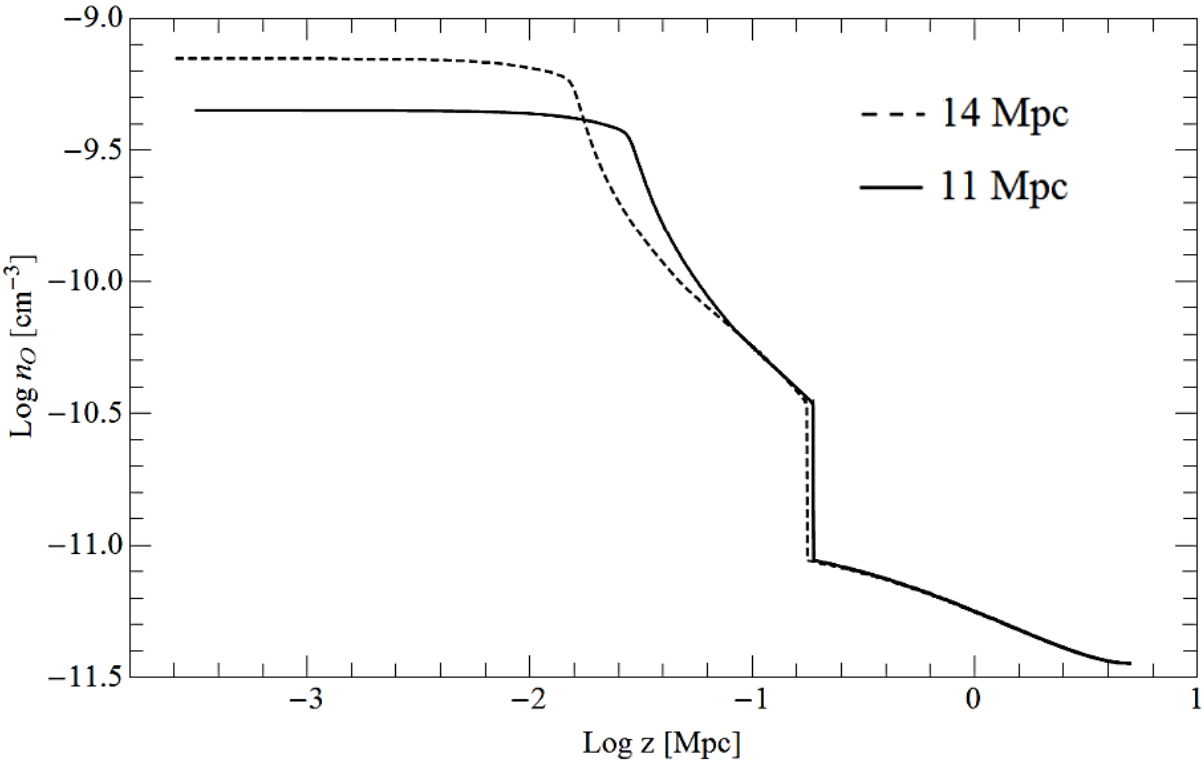

Figure 2.3: Oxygen number density profiles for initial perturbation length scales, L, of 11 and 14 Mpc.

The next step is to figure out what fraction of oxygen is in the form of O^{5+}. Yoshikawa and Sasaki (2006) present the ionization fractions of O^{5+} (in addition to other oxygen ions) as a function of temperature for the WHIM. Figure 2.4 shows the ionization fractions for O^{5+} as a function of temperature and number density.

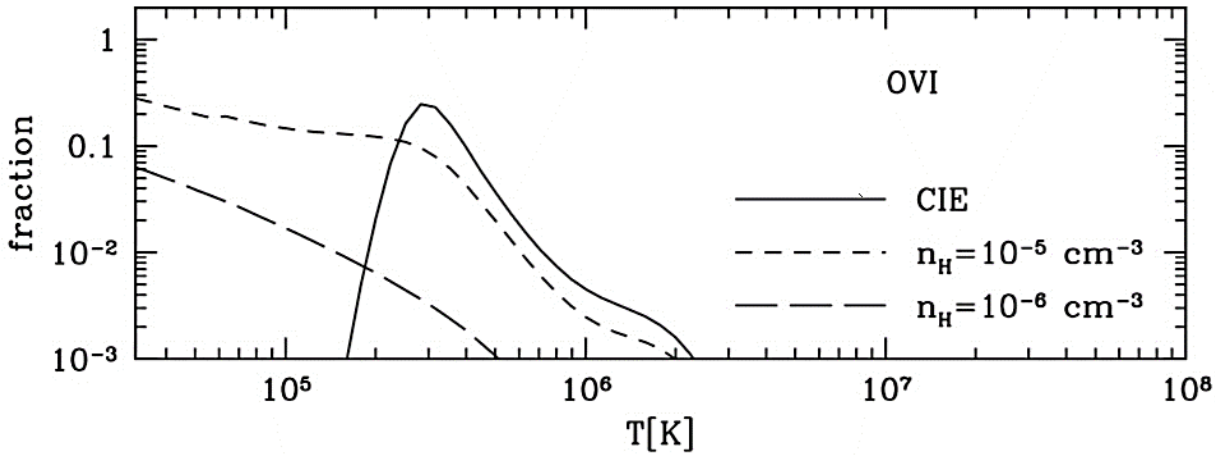

Figure 2.4: Ionization fractions for O^{5+} as a function of temperature for both a state of collisional ionization equilibrium and under the influence of photoionization effects (Yoshikawa and Sasaki 2006).

The dashed lines in figure 2.4 represent the ionization fractions in the presence of photoionization, while the solid line does not, only showing the ionization fraction that would occur as a result of collisional ionization equilibrium. The WHIM is not in a state of ionization equilibrium (Yoshikawa and Sasaki 2006) and therefore the solid line is of no interest for this thesis.

The ionization fraction is dependent on two factors: the temperature and the hydrogen number density, both profiles of which are, of course, provided by Klar and Mücket (2010). Yoshikawa and Sasaki (2006) only provide the ionization fractions as a function of temperature for two hydrogen number densities, those being $\log(n_H) = -5$ atoms/cm^3 and $\log(n_H) = -6$ atoms/cm^3. Fortunately, as can be seen in Figure 2.2, the number density of hydrogen varies, for the most part, between these two values. Therefore, in order to best estimate an O^{5+} ionization fraction profile for the Local Sheet, a linear interpolation of the two profiles from Yoshikawa and Sasaki (2006) was performed.

To compute the O^{5+} fraction as a function of vertical distance above the Sheet, the variation with temperature was transformed using the vertical temperature profile provided by Klar and Mücket (2010). The resulting profiles can be seen in Figure 2.5.

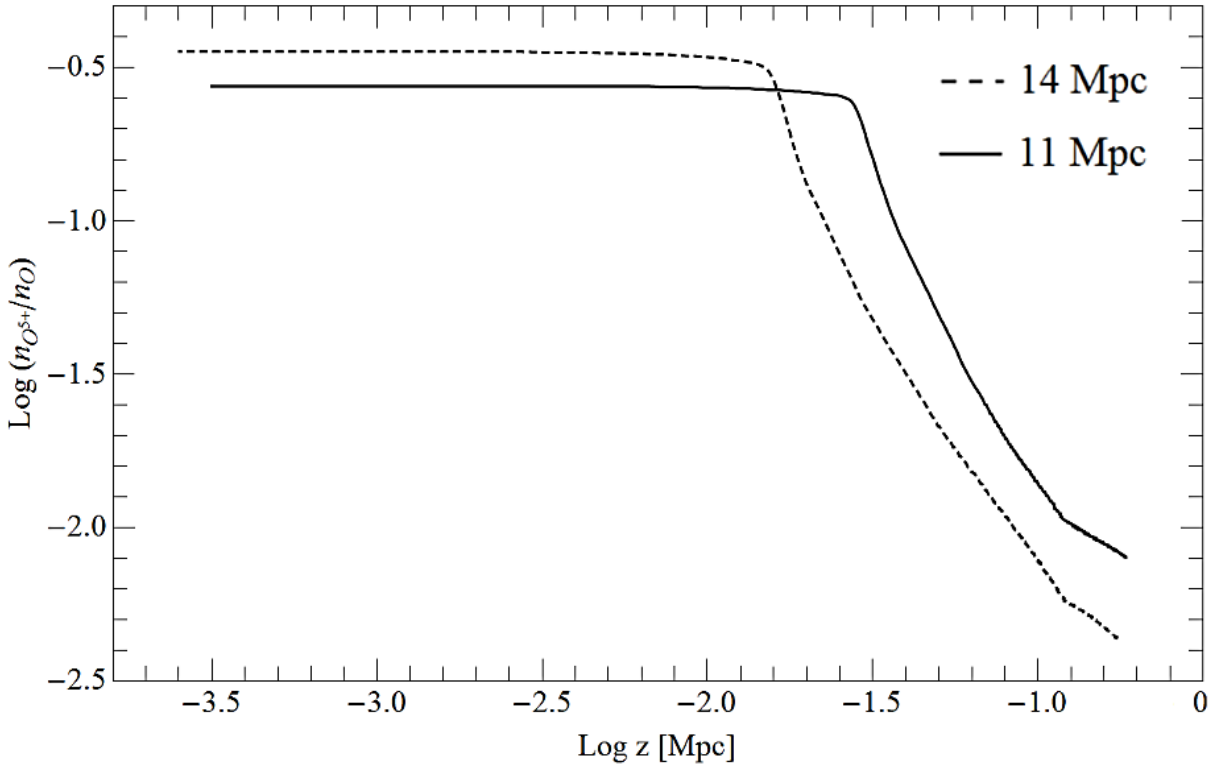

Figure 2.5: O^{5+} ionization fraction profiles for initial perturbation length scales, L, of 11 and 14 Mpc.

Having the O^{5+} ionization fraction as a function of perpendicular height above the Sheet as well as the oxygen number density as a function of that same height, the product of the two produces the O^{5+} number density profile for the Local Sheet. The resulting profiles can be seen in Figure 2.6.

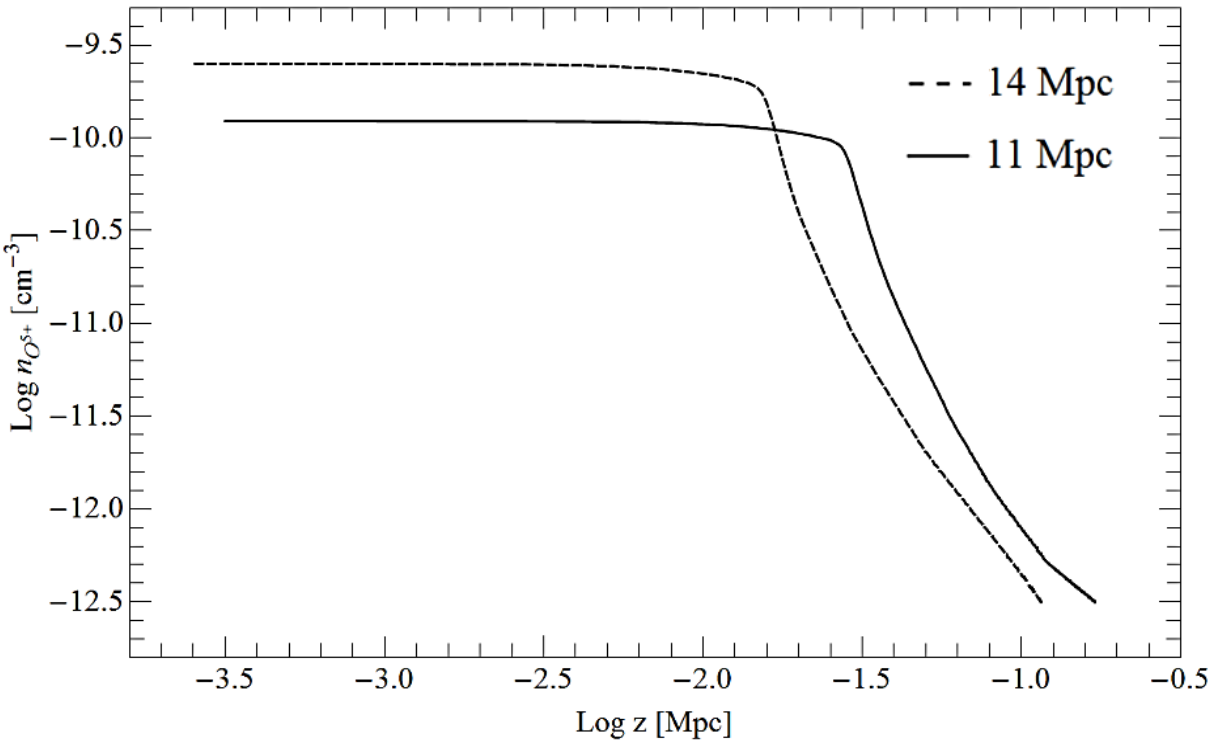

Figure 2.6: O^{5+} number density profiles for initial perturbation length scales, L, of 11 and 14 Mpc.

With the O^{5+} number density profile in hand, the expected equivalent widths of the OVI absorption lines as a function of Sheet latitude can be determined by constraining the geometry of the WHIM in three dimensions. For simplicity, the WHIM is approximated as a cylindrical slab of gas with edges defined to be at the same distance from the centre as half the perturbation length scale L. Unfortunately, this geometry likely fails near the edges of the Sheet, where it is uncertain what effects the edge has on the distribution of the WHIM. For this reason, in establishing equivalent widths, a lower limit on the latitude is imposed, which corresponds to the top or bottom edge of the cylindrical slab. This lower limit serves to avoid the gas at the edges of the Sheet and thus averts problems with the gas distribution there.

The adopted geometry for the WHIM is shown in Figure 2.7, in which the radius, height, and minimum latitude angle are labelled as r, h, and θ_{min}, respectively, with values dependent on the choice of perturbation scale length L. The height of the cylinder was defined as being the height

at which 99.8% of the O^{5+} ions by number are contained within the cylinder. The coordinate system shown in Figure 2.7 is the rotated sheet coordinate system.

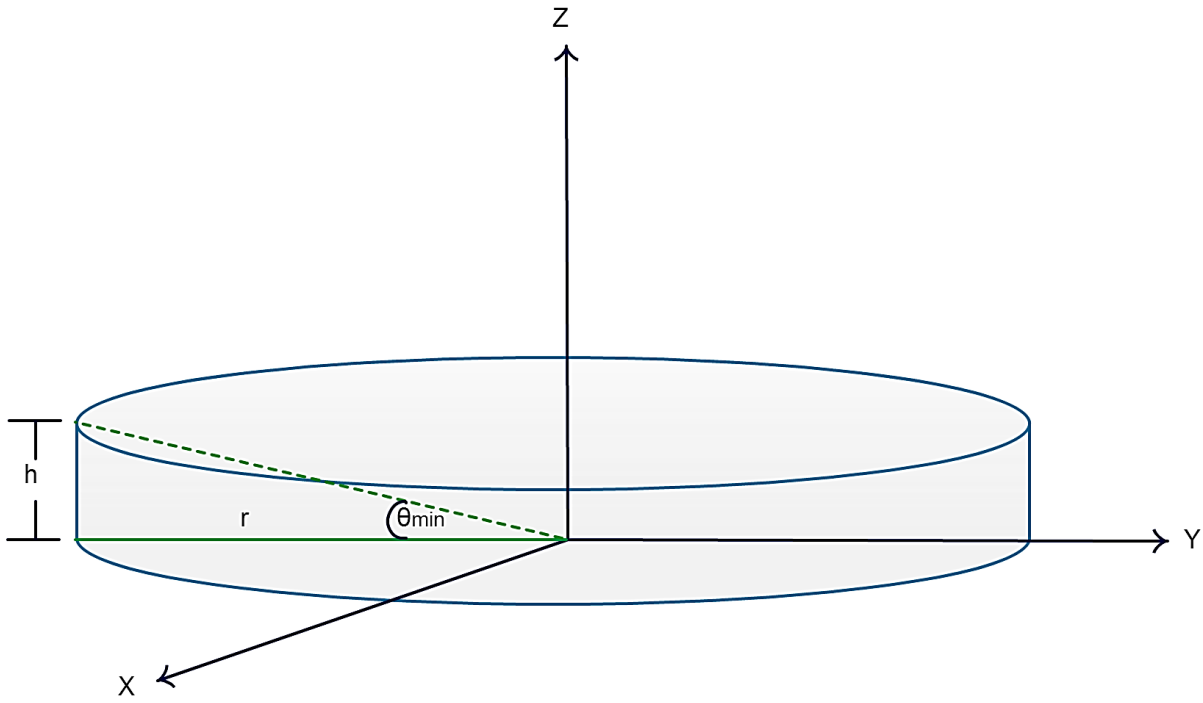

Figure 2.7: Depiction of the WHIM located above the plane of the Local Sheet (not to scale).

The values for the height, h, and radius, r, were calculated for each of the 11 Mpc and 14 Mpc Sheet sizes. The results are summarized in table 2.1.

Table 2.1: Cylindrical Sheet dimensions.

Sheet Size (Mpc)	Radius r (Mpc)	Height h (Mpc)
11	5.59	0.188
14	6.98	0.176

From these values, it is possible to determine the minimum latitude, θ_{min}:

$$\theta_{min} = \arctan\left(\frac{h}{r}\right) \quad [2.4]$$

The resulting values are 1.93° and 1.44° for the 11 Mpc and 14 Mpc cases, respectively.

In order to look at the dependence of the equivalent width on the latitude of the probe above the plane of the Local Sheet, a relationship between the O^{5+} number density and the equivalent width of OVI absorption has to first be defined. By combining equations 1.1 and 1.2, the equivalent width of an absorption line can be expressed as

$$W = \int (1 - \exp[-\tau_\lambda]) d\lambda \quad [2.5]$$

with a general expression for the optical depth given by

$$\tau_\lambda = \int_0^{\mathcal{L}} \eta(\lambda) n_i(\ell) d\ell \quad [2.6]$$

where $\eta(\lambda)$ is the wavelength-dependent cross section, ℓ is the path length through the absorbing medium, and $n_i(\ell)$ is the number density profile of the absorbing population (i.e. the population of the lower level of the transition) along the line of sight to the probe. On the basis of the classical oscillator model, the cross section can be expressed as the product of a line profile and a factor which is dependent on the quantum mechanical properties of the absorbing atoms (Tatum 2011):

$$\eta(\lambda) = \frac{e^2 \lambda^2}{4\varepsilon_o m c^2} \Phi_\lambda \quad [2.7]$$

Here, Φ_λ is the absorption line profile, e is the fundamental electric charge, λ is the rest wavelength of the line in question, ε_o is the permittivity of free space, m is the mass of an electron, and c is the speed of light.

The line profile for any given absorption line is determined by many different factors, all of which create small velocity differences between absorbers, resulting in a distribution on absorption along a range of wavelengths. Some such factors include, but are not limited to, natural broadening brought upon by Heisenberg's uncertainty principle, pressure broadening due to the close proximity of absorbing particles, and thermal broadening brought upon by the relative motions of the absorbing particles at a particular temperature. The effects of natural broadening are very small and can be ignored for our purposes. Pressure broadening can similarly be ignored since it should be small due to the low hydrogen density and correspondingly low frequency of interactions of the ions. Thus, out of these three line broadening effects, thermal broadening is expected to dominate the line shape profile.

Ions have a velocity distribution due to their temperature, and as such, any radiation absorbed or emitted is broadened by the combined effect of all of their Doppler shifts. Treating the O^{5+} gas as being ideal, the temperature-velocity relation can be described by the Maxwell-Boltzmann distribution, which expresses the probability, $f(v)$, that a gas particle of mass m will have a velocity v at a specific temperature T. A requirement of the Maxwell-Boltzmann distribution is that the system be in thermodynamic equilibrium, and so the assumption that the WHIM is uniform in temperature had to be made in order to make use of it. Thus, the thermal broadening being calculated is an estimate of the true value, however it will still provide a strong indication of the expected OVI line shapes. Since all motion relevant to thermal broadening is directed radially with respect to the observer, only the one-dimensional Maxwellian distribution is required. The one-dimensional Maxwellian distribution is given by

$$f(v) = \sqrt{\left(\frac{m}{2\pi kT}\right)} \exp\left(-\frac{mv^2}{2kT}\right) \qquad [2.8]$$

where k is the Boltzmann constant.

The wavelength at which the particle absorbs is shifted by $\Delta\lambda$ with respect to the rest wavelength λ_o as a result of the Doppler effect:

$$\Delta\lambda = \lambda_o \left(\frac{v_r}{c}\right) \quad [2.9]$$

By substituting the radial velocity, v_r, from equation 2.9 into equation 2.8, it is then possible to obtain a probability function defining the Doppler shift as a function of particle mass and temperature:

$$f(\lambda) = \sqrt{\left(\frac{m}{2\pi kT}\right)} \exp\left(\frac{-mc^2(\lambda - \lambda_o)^2}{2kT\lambda_o^2}\right) \quad [2.10]$$

It is clear that the probability function is Gaussian in nature. The standard deviation, σ, is given by equation 2.11.

$$\sigma = \lambda_o \sqrt{\frac{kT}{mc^2}} \quad [2.11]$$

An estimate as to the upper limit of thermal broadening for O^{5+} gas in the Local Sheet can be made using equation 2.11 and the upper limit of the temperature of the O^{5+} gas, which was obtained from the temperature profile. The temperature upper limits have values of 1.77×10^5 K and 2.64×10^5 K for the 11 and 14 Mpc sheets, respectively. The resulting values of σ are 0.033 Å and 0.040 Å for the 11 and 14 Mpc sheets, respectively.

The thermal broadening is characterized by a Gaussian absorption profile with the form

$$I_\lambda = I_{o\lambda} \exp\left[-a \exp[-\frac{(\lambda - \lambda_o)^2}{2\sigma^2}]\right] \quad [2.12]$$

where a is the amplitude of the absorption, λ is the independent wavelength variable, λ_o is the position of the line, and σ is the standard deviation of the line. By comparing equation 2.12 to

equation 1.1, it can be seen that the Gaussian absorption profile is simply equation 1.1 with an optical depth, τ, varying as a Gaussian with λ. In this work, the thermal broadening is approximated by fixing T at the upper limit of the O^{5+} temperature, i.e. assuming σ to be invariant with height (z'). The thermally broadened line profiles for each of the 11 and 14 Mpc sheet sizes are plotted in Figure 2.8.

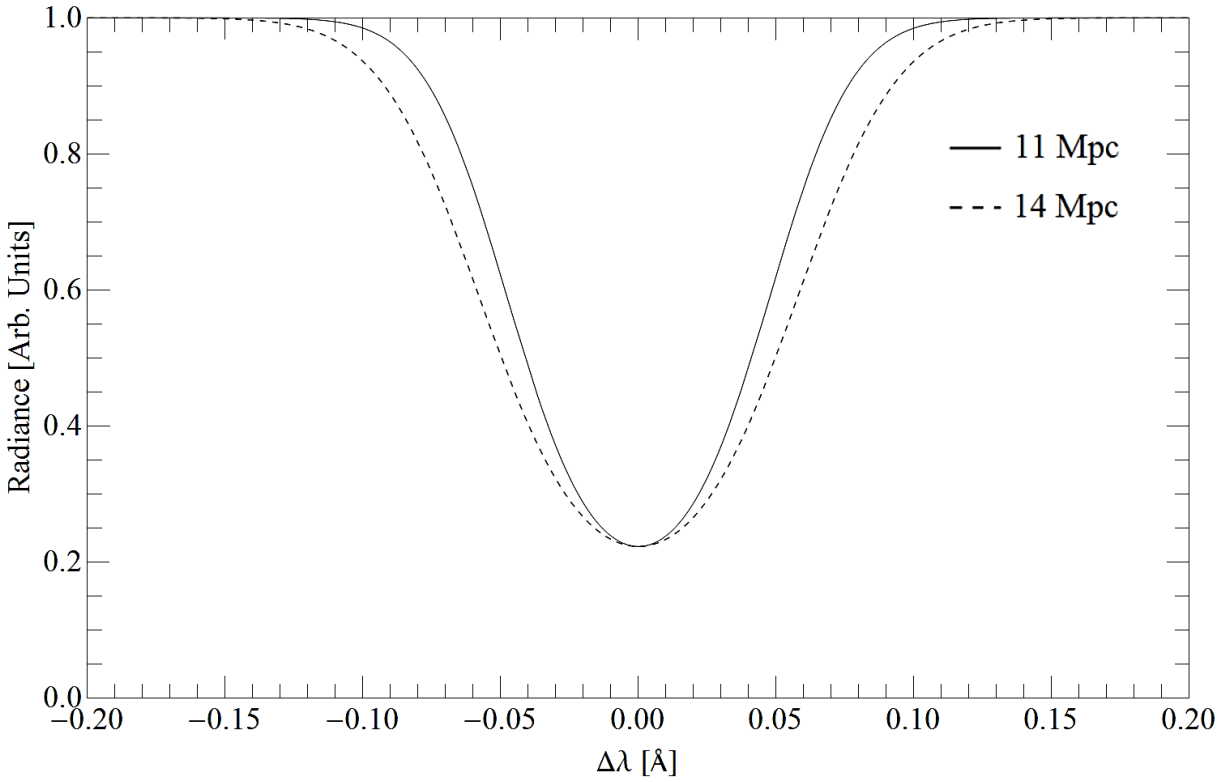

Figure 2.8: Thermally broadened line profiles expected for OVI absorption lines for 11 and 14 Mpc sheet sizes. The line profiles are depicted with arbitrary, but equal depths.

In addition to the thermal broadening, there is another line broadening effect that must be considered, occurring as a result of the Sun's offset from the plane of the Sheet. The WHIM is collapsing perpendicular to the Sheet. From the perspective of the Sun (offset from the mid-plane), absorption should have two velocity components, one receding from the Sun and another approaching it. Thus, for high latitude observations, it might be expected that OVI line splitting that is dependent on the velocity, v, of the collapsing gas would be observed.

Klar and Mücket (2010) provide the velocity profiles for the 11 and 14 Mpc sheets that will be used to predict the line splitting (see Figure 2.9).

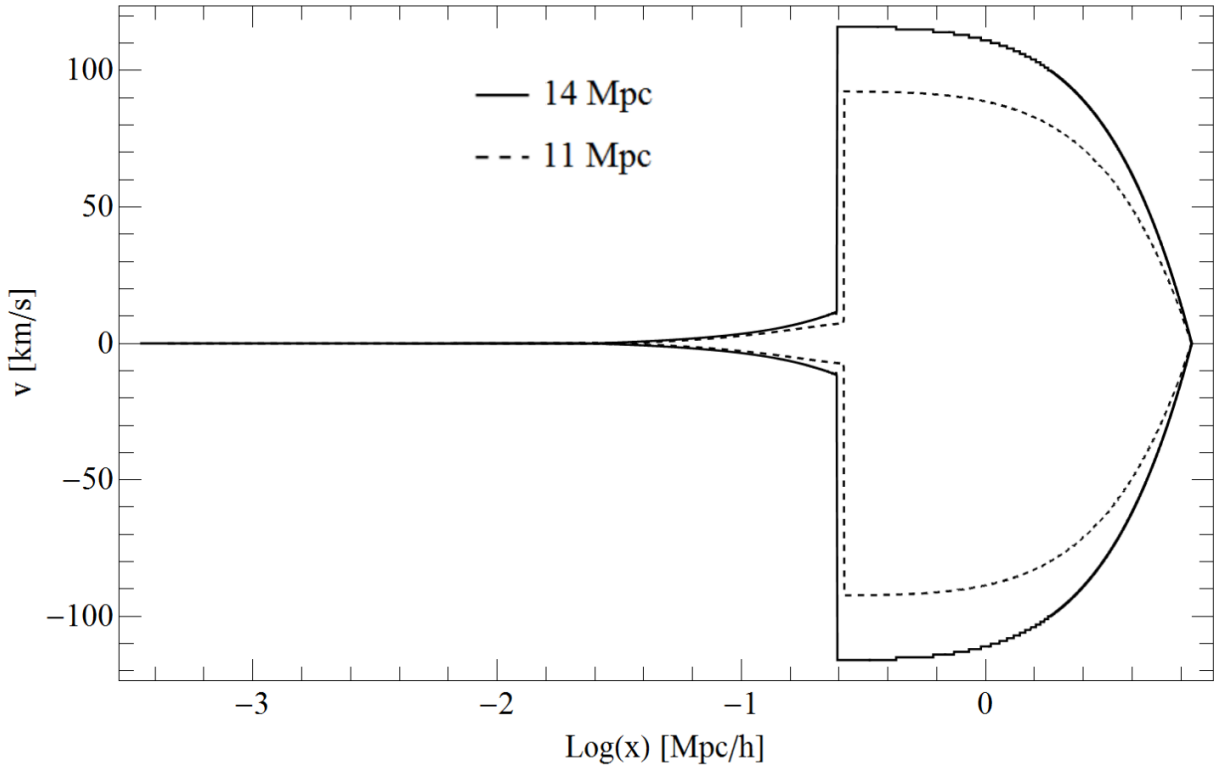

Figure 2.9: Velocity profiles for initial perturbation length scales, L, of 11 and 14 Mpc.

It can be seen from Figure 2.9 that the infalling gas has extremely high velocities outside of the shock region, at which point the velocities drastically decrease as kinetic energy is converted to heat through shock heating. The velocities of greatest interest are those where the number density of O^{5+} ions are greatest since the majority of the OVI absorption will be occurring at these velocities. Comparing Figures 2.6 and 2.13, it can be seen that the inner region of highest O^{5+} number density corresponds to relatively low velocities, approaching zero. The velocity increases outward through the shock heated region up to the sound speed in the gas, while the number density drops off. Since the region of highest velocity is outside of the shock heated region, there is very little O^{5+} gas that is moving at large enough speeds for there to be an

observable effect on the OVI absorption line shapes. At lower latitudes, the broadening from the Hubble flow dominates and the infall velocity broadening becomes even less significant. Thus, it can be concluded that the infalling gas does not significantly contribute to the absorption line profile and so it will not be included in the equivalent width calculations.

There is a final line broadening effect left to consider, which is brought upon by the expansion of space. At low Sheet latitudes, the WHIM that is associated with the Local Sheet extends out to distances of several megaparsecs away from the Sun. This large distance, coupled with the fact that the Local Sheet is not virialized, leads one to conclude that the OVI absorption lines along those lines of sight must be redshifted with respect to the rest frame of the Local Sheet in accordance with the Hubble flow. This redshift would manifest itself in equation 2.12 as a shift in λ_o. Using Hubble's Law, the absorption line profile can be expressed as

$$\Phi_\lambda = \frac{1}{\sqrt{2\pi}\sigma} \exp\left\{ -\frac{\left(\lambda - \left[\lambda_o\left(1 + \frac{H_o \ell}{c}\right)\right]\right)^2}{2\sigma^2} \right\} \qquad [2.13]$$

where H_o is the Hubble constant and $\frac{1}{\sqrt{2\pi}\sigma}$ is a normalization constant.

By substituting the thermal plus Hubble flow broadened absorption line profile back into equations 2.7 and 2.6, an expression for the optical depth along any line of sight was derived to be

$$\tau_\lambda = \frac{e^2\lambda^2}{4\varepsilon_o m c^2 \sqrt{2\pi}\sigma} \int_0^{\mathcal{L}} \exp\left\{ -\frac{\left(\lambda - \left[\lambda_o\left(1 + \frac{H_o \ell}{c}\right)\right]\right)^2}{2\sigma^2} \right\} n_i(\ell) d\ell \qquad [2.14]$$

It is expected that the spontaneous rate of emission of the O^{5+} gas is much larger than the rate of excitation, especially since the gas is so diffuse that collisional excitations are rare, so it is

safe to assume that the number density of the absorbing population is equal to that of the O^{5+} ion as a whole, i.e. $n_1(\ell) \cong n_{O^{5+}}(l)$.

By substituting equation 2.14 into equation 2.5, a final expression for the equivalent width of an OVI absorption line along any line of sight was obtained,

$$W = \int_{-\infty}^{\infty} \left(1 - \exp \left[\frac{-e^2 \lambda^2}{4\varepsilon_o mc^2 \sqrt{2\pi}\sigma} \int_0^{\mathcal{L}} \exp \left\{ - \frac{\left(\lambda - \left[\lambda_o \left(1 + \frac{H_o \ell}{c} \right) \right] \right)^2}{2\sigma^2} \right\} n_{O^{5+}}(l) d\ell \right] \right) d\lambda \quad [2.15]$$

Before being able to integrate equation 2.15 over the appropriate path lengths, the position of the Sun relative to the centre of the Local Sheet (as defined optically), and by extension the centre of the Local Sheet WHIM, must be considered when defining the limits of integration. The Sun has rotated Sheet coordinates of (x,y,z)=(-0.36,-0.72,+0.13) and is thus offset from the centre of the Local Sheet. The coordinates of any object viewed from FUSE would be in a heliocentric coordinate frame. In such a frame, the path length that the electromagnetic radiation takes through the absorbing medium, and thus the Hubble broadening, depends on both the longitude and latitude of the target. Figure 2.9 shows the relative position of the Sun within the WHIM of the Local Sheet, and the positioning of the heliocentric rotated sheet coordinate system relative to the rotated sheet coordinate system anchored to the Sheet centre. Figure 2.10 shows the position of the Sun relative to the entire Sheet, not just the upper half of it as was shown in Figure 2.7.

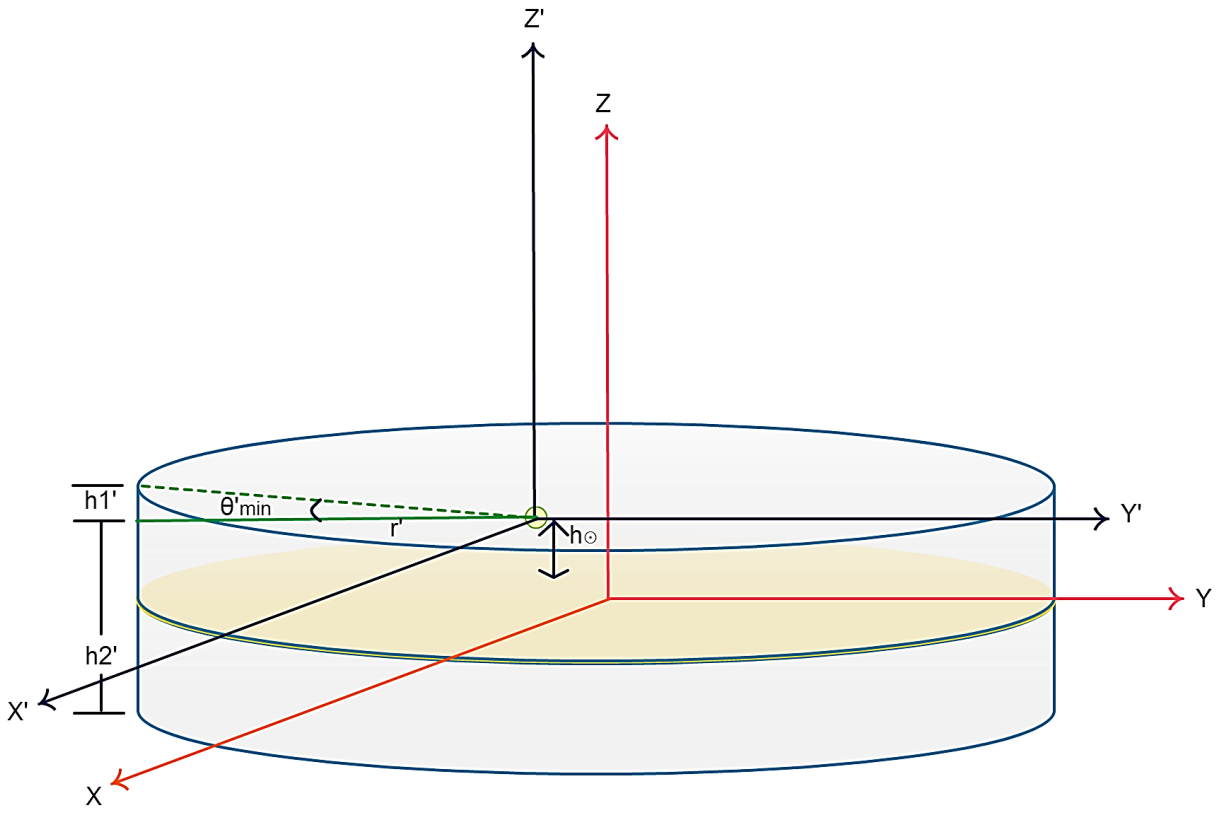

Figure 2.10: Depiction of the WHIM above and below the plane of the Local Sheet. The heliocentric coordinate system is marked by (x',y',z') coordinate axes, shown in black.

With the Sun offset from the centre of the Sheet, the values for h, r, and θ_{min} are no longer independent of direction. The key dimensional parameters for the 11 and 14 Mpc Sheets are summarized in table 2.2 and will be explained in what follows.

Table 2.2: Key dimensional parameters for the 11Mpc and 14Mpc Sheets.

Parameter	11 Mpc Sheet	14 Mpc Sheet
Positive Latitude h'_1 (Mpc)	0.059	0.047
Negative Latitude h'_2 (Mpc)	0.317	0.305
r'_{max} (Mpc)	6.39	7.79
r'_{min} (Mpc)	4.78	6.18

In the heliocentric coordinate system, there are only two possible values for h′, one for positive latitudes ($\mathrm{h'}_1$) and one for negative latitudes ($\mathrm{h'}_2$). The value of r', on the other hand, varies depending on the longitude, ϕ', of the observed target. Defining $\mathrm{x}_\odot$ and $\mathrm{y}_\odot$ to be the rotated Sheet coordinates of the Sun, then $\mathrm{d} = \sqrt{\mathrm{x}_\odot^2 + \mathrm{y}_\odot^2} = 0.804$ Mpc is the projected distance between the centre of the Sheet and the position of the Sun. The r′ values then vary between $\mathrm{r'}_{\max} = \mathrm{r} + \mathrm{d}$ and $\mathrm{r'}_{\min} = \mathrm{r} - \mathrm{d}$. The longitude that corresponds to the direction in which $\mathrm{r}' = \mathrm{r'}_{max}$ is given by $\arctan\left(\frac{\mathrm{y}_\odot}{\mathrm{x}_\odot}\right) = 63.2^{\mathrm{o}}$. The relationship between r' and ϕ' can be found using the cosine law:

$$r' = \sqrt{r^2 - d^2 + 2r'dcos\left(\phi' - arctan\left(\frac{y}{x}\right)\right)} \qquad [2.16]$$

With an expression for r′, it was then possible to constrain how θ'_{min} must vary with longitude:

$$\theta'_{min} = \arctan\left(\frac{h'}{r'}\right) \qquad [2.17]$$

Where r′ is given by equation 2.16.

With the geometrical limits of the Sheet defined, it was possible to derive an expression for the path length as a function of θ'. Above θ'_{min}, the path length does not depend on ϕ' due to the uniform and symmetrical WHIM profile associated with the Sheet. No matter the value of ϕ', the line of sight still passes through a gas slab of constant height h′. With the values for both h′ and θ' known, the path length follows:

$$\ell = \frac{h'}{\sin(\theta')} \qquad [2.18]$$

Knowing how the path length depends on h' and θ' makes it possible to re-write the integration over the path length as an integration over the thickness of the Sheet. The result is a piecewise function that is dependent on the latitude of the observation:

$$\int_0^{\mathcal{L}} \exp\left\{-\frac{\left(\lambda-\left[\lambda_o\left(1+\frac{H_o\ell}{c}\right)\right]\right)^2}{2\sigma^2}\right\} n_{O^{5+}}(l)\,d\ell \qquad [2.19]$$

$$= \begin{cases} \displaystyle\int_{h_\odot}^{h_1'+h_\odot} \exp\left\{-\frac{\left(\lambda-\left[\lambda_o\left(1+\frac{H_o z}{c\sin(\theta')}\right)\right]\right)^2}{2\sigma^2}\right\}\frac{n_{O^{5+}}}{\sin(\theta')}\,dz & \theta'>0 \\ \displaystyle\int_0^{h_\odot} \exp\left\{-\frac{\left(\lambda-\left[\lambda_o\left(1+\frac{H_o z}{c\sin(\theta')}\right)\right]\right)^2}{2\sigma^2}\right\}\frac{n_{O^{5+}}}{\sin(\theta')}\,dz & \theta'<0 \\ \quad + \displaystyle\int_{-(h_2'-h_\odot)}^{0} \exp\left\{-\frac{\left(\lambda-\left[\lambda_o\left(1+\frac{H_o z}{c\sin(\theta')}\right)\right]\right)^2}{2\sigma^2}\right\}\frac{n_{O^{5+}}}{\sin(\theta')}\,dz & \end{cases}$$

Here $\mathrm{h}_\odot = 0.129$ Mpc is the height of the Sun above the plane of the Sheet. The range of integration is dependent on the sign of θ'.

By substituting equation 2.19 into 2.15 and performing the integration, it was possible to determine the expected equivalent widths of the OVI absorption lines as a function of $\csc(\theta')$ for both positive and negative latitude observations. The results can be seen in Figure 2.11 where the predicted equivalent widths are plotted as a function of $\csc(\theta')$ for the 11 Mpc and 14 Mpc Sheets.

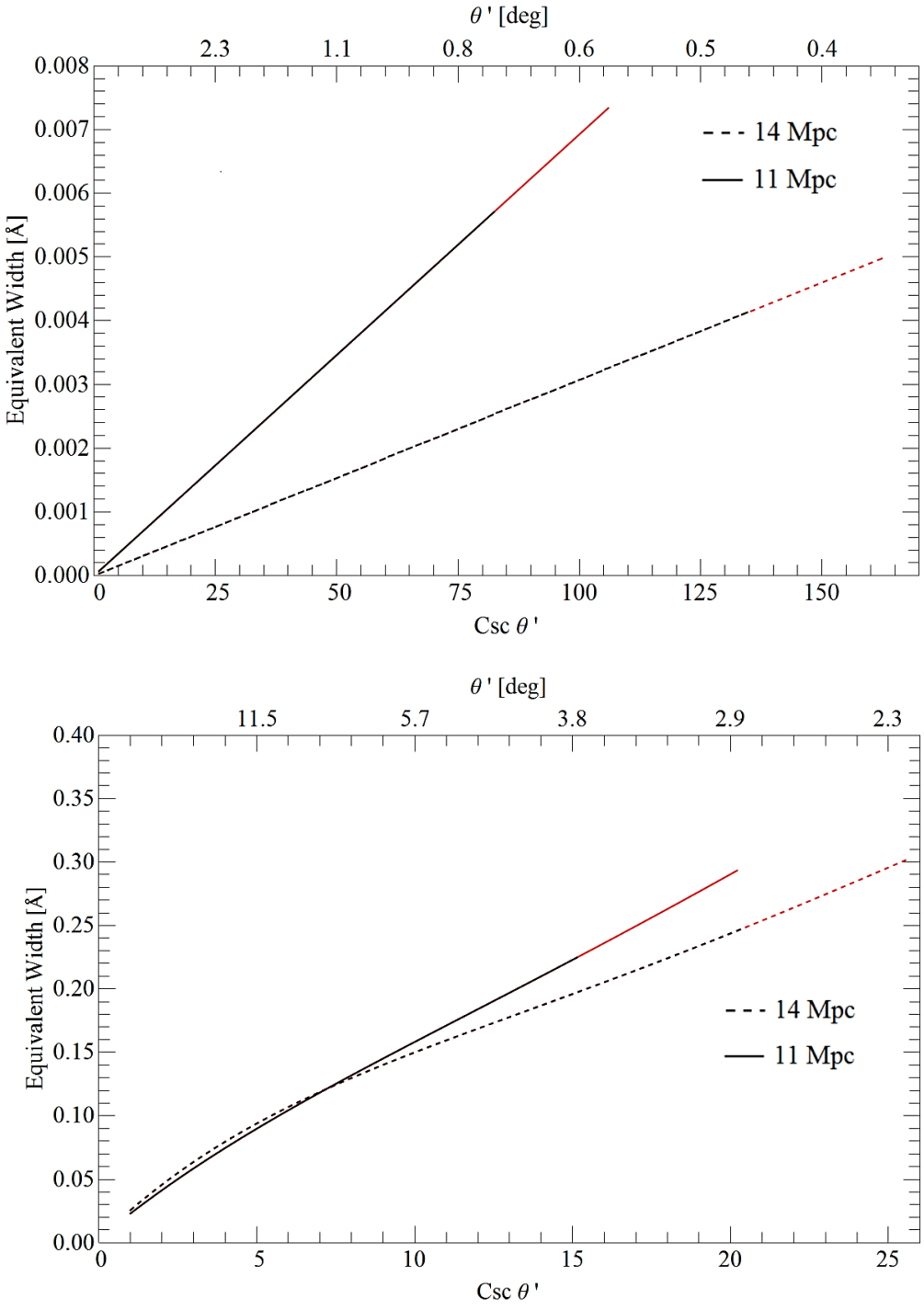

Figure 2.11: Theoretical equivalent widths as a function of the cosecant of the absolute value of the heliocentric Sheet latitude. The top plot shows the results for latitude directed along the same direction as the offset between the Sun and the plane of the Sheet (positive z′), while the bottom plot shows the results for latitude directed in the opposite direction (negative z′). The csc(θ′) axis range is set by θ'_{min}. The black lines apply to all ϕ', while the red lines apply only for ϕ' values where θ' is between the maximum and minimum θ'_{min} values.

Along lines of sight in the same direction that the Sun is offset perpendicularly from the plane of the Sheet, h′ is small, and the equivalent widths are correspondingly low, regardless of the observing angle. They are so low in fact that it would be impossible to observe OVI lines using FUSE, since they would be buried in the noise of the spectrum. As an example, in order for a line with a full-width at half-minimum (FWHM) equal to that of the FUSE resolution of 20 km/s, or 0.069 Å (Wood et al. 2002), to have an equivalent width as low as 0.006 Å, the depth of that line would be on the order of only 3% the continuum intensity.

The reasoning behind the large discrepancy in equivalent widths with respect to the sign of the latitude in which they are observed is made clear when looking at the number density profile as a function of redshift from the Sun, as seen in Figure 2.12.

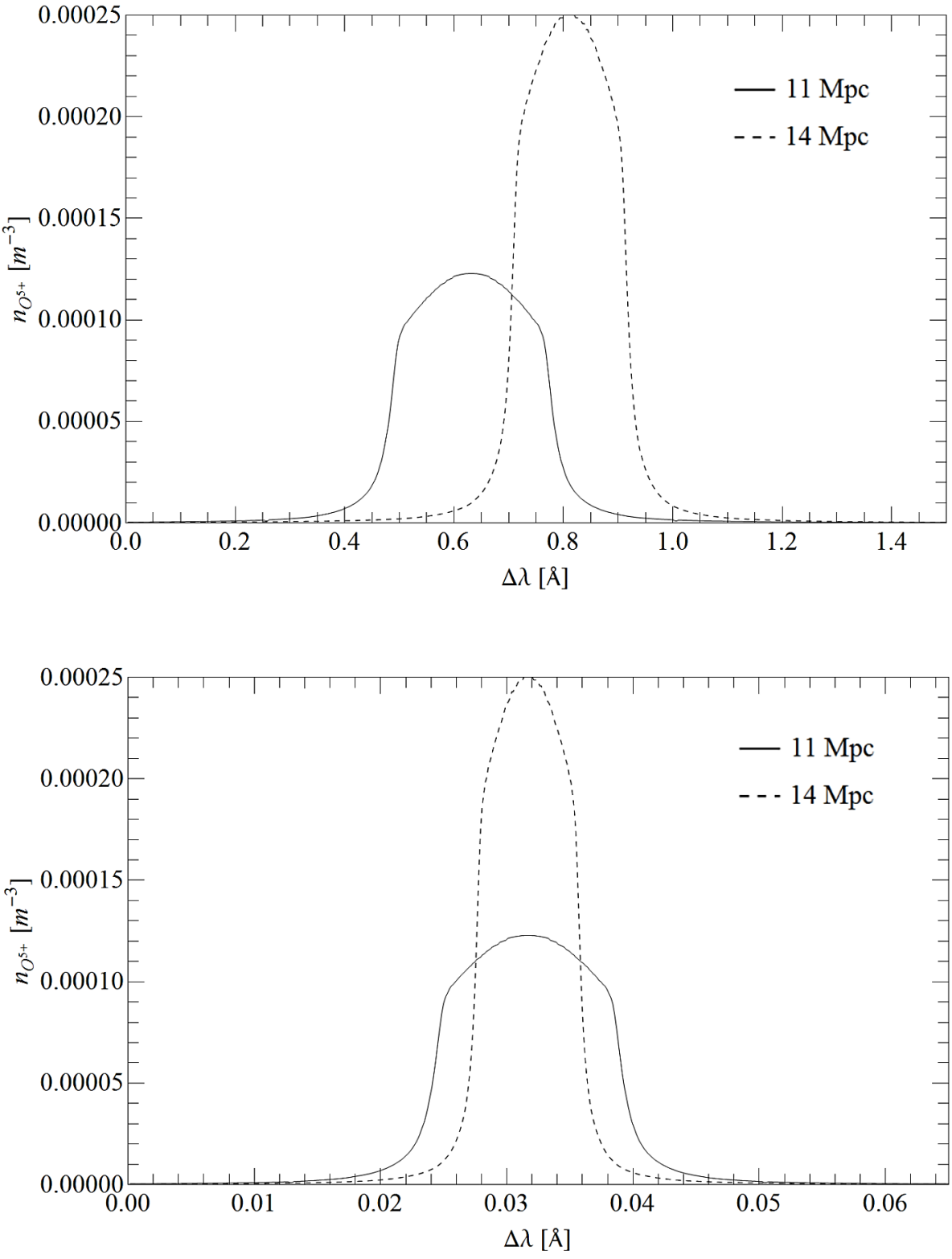

Figure 2.12: O^{5+} number density as a function of heliocentric redshift for both the maximum (top) and minimum (bottom) path lengths through the 11 and 14 Mpc Sheets as seen from the Sun.

Along lines of sight directed opposite to the Sun's offset from the plane of the Sheet, h′ is much larger, and the equivalent widths are on the order of 100 times greater. Such lines would not be buried in the noise, and so it would be expected that they could be observed using FUSE, subject of course to the metallicity of the WHIM. If the metallicity were a factor of 10 lower than expected, it would be impossible to detect any of the OVI absorption lines associated with the WHIM.

To summarize, it is predicted that if the metallicity of the WHIM associated with the Local Sheet is on the order of one tenth solar, then it should be possible to observe a dependence in OVI equivalent width as a function of csc(θ'). Furthermore, it is predicted that this dependence will be asymmetric with θ', and that the OVI lines will only be detectable along the negative θ' direction.

2.2 Absorption Line Shapes

2.2.1 Theoretically Expected Shapes

Although the trend of equivalent width with latitude is the clearest way to discern WHIM associated with the Local Sheet, there are other tracers that can also be explored. One is the shape of the OVI absorption lines.

By substituting equation 2.14 into equation 1.1 and integrating over the maximum and minimum possible path lengths through the simulated sheets, the absorption line profiles with both thermal and Hubble-flow broadening were calculated for both the 11 and 14 Mpc sheets. They are plotted in Figure 2.13. The FWHM and the redshifts of the absorption minima are presented in Table 2.3.

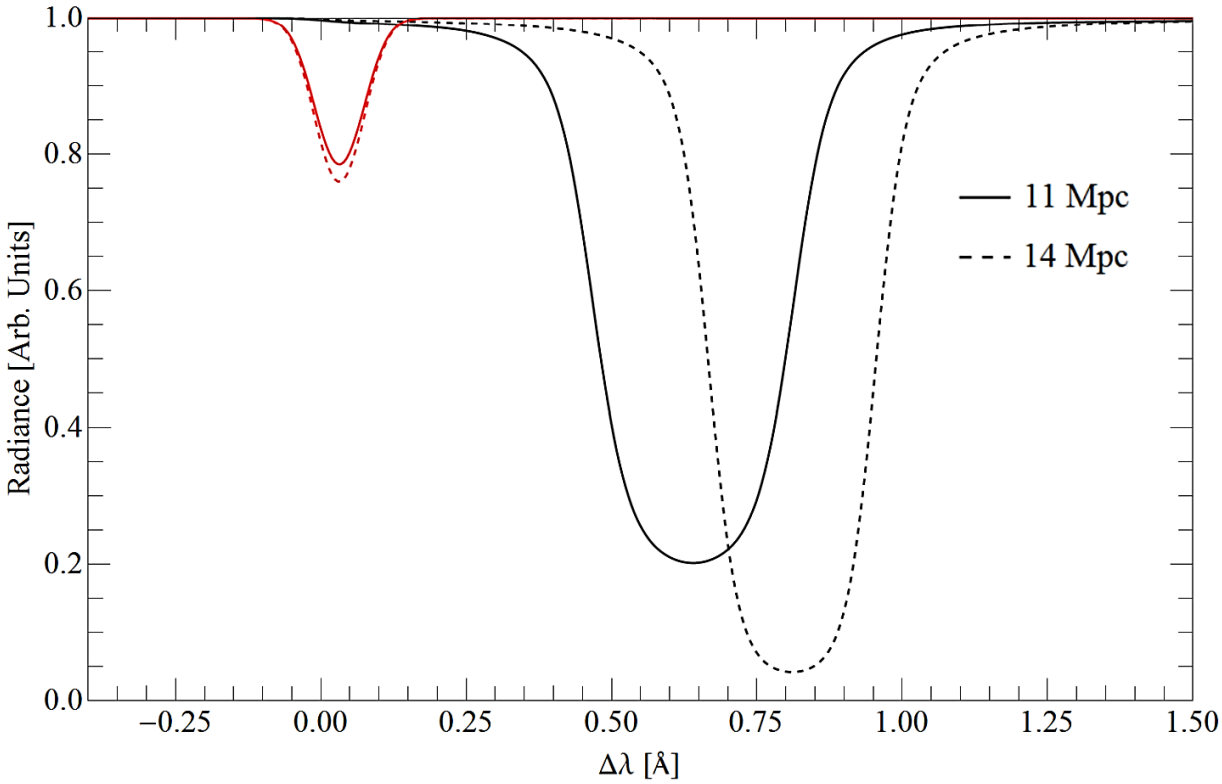

Figure 2.13: Radiance of OVI lines as a function of heliocentric redshift for both the maximum and minimum path lengths through the 11 and 14 Mpc sheets. The maximum path lengths are coloured black and the minimum path lengths are coloured red.

Table 2.3: Full widths at half minimum and redshifts of OVI absorption lines for the minimum and maximum path lengths through the WHIM for both the 11Mpc and 14Mpc sheets as a result of thermal and Hubble broadening effects.

Sheet	Path Length	Full-Width at Half-Minimum [Å]	Absorption Minimum Redshift [Å]
14	Max	0.248	0.814
14	Min	0.097	0.032
11	Max	0.309	0.637
11	Min	0.091	0.032

By comparing the calculated widths to the standard deviations of the thermally broadened Gaussian profiles (Figure 2.8), it can be seen that the effects of the Hubble broadening are

relatively insignificant for the minimum path lengths through the WHIM. For the maximum path lengths, however, the standard deviations of the absorption lines are on the order of 2-3 times as large as that due to thermal broadening alone. Additionally, the shapes of these lines are affected by the O^{5+} number density profile and are no longer truly Gaussian, having a more rounded base and more extended wings.

The calculations predict an OVI line profile that is dependent on the altitude of a target above the plane of the Sheet. Both the redshift of the absorption minimum and the width vary and offer observational means of differentiating between OVI absorption by WHIM found in the Local Sheet and similarly absorbing gas found in the Milky Way. Additionally, observed full widths at half minimum and redshifts could be used to constrain the geometry and composition of any WHIM associated with the Local Sheet, since they are tied to the number density profile and the oxygen abundance.

2.2.2 Deviations from the Baseline Model

All of the statements about the line shape up to this point have been made under the assumption that the theoretical construct from section 2.1 is exact. Here, the effects of some possible departures from the model are discussed.

If the vertical distribution of the WHIM associated with the Local Sheet had a greater extent, so that the Sun was inside the O^{5+} gas layer, or if the plane of the WHIM associated with the Sheet were shifted closer to the Sun (away from the plane as defined by the giants of the Local Sheet), then there would be a greater density of absorbing gas near to the Sun. Taking into account the Hubble flow, maximum absorption would take place nearer the rest wavelength of the OVI lines, and absorption lines would be skewed redward.

The magnitude of the skew is directly dependent on the distance through the WHIM that a particular line-of-sight traverses, which is in turn related to the latitude of the target. For this reason, it would be expected that there would be a larger skew along the larger path lengths through the WHIM than the shorter ones. By centering the z=0 position of the $n_{O^{5+}}$ profile on the Sun and integrating equation 2.14 over the maximum and minimum possible path lengths through the simulated sheets, the skewed absorption line profiles including thermal broadening and Hubble flow effects were calculated using equation 1.1. They are plotted in Figure 2.14.

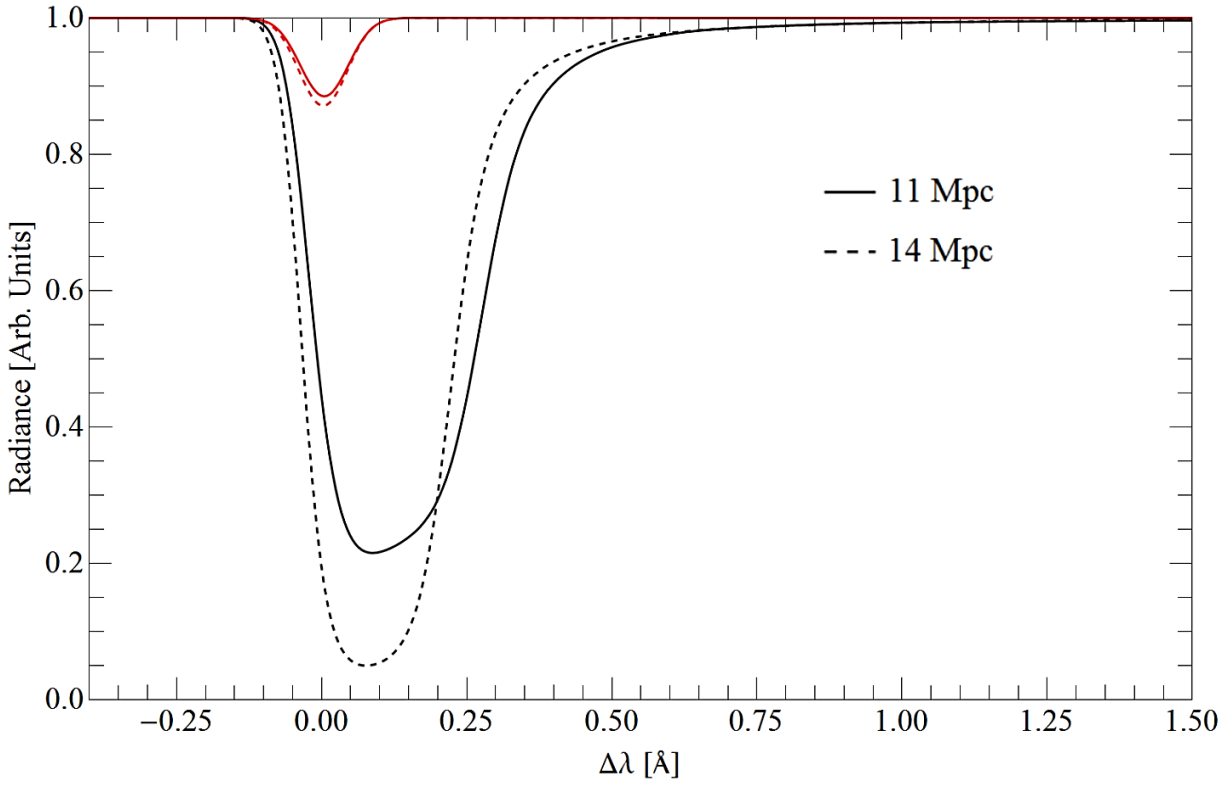

Figure 2.14: Radiance of OVI lines as a function of heliocentric redshift for both the maximum and minimum path lengths through the 11 and 14 Mpc sheets for paths originating from the mid-plane of the WHIM. The maximum path lengths are coloured black and the minimum path lengths are coloured red.

Having the mid-plane of the WHIM aligned with the z position of the Sun would also change the expected equivalent width to csc(θ') relationship. With the mid-plane of the WHIM centered on the Sun, the path lengths through the O^{5+} gas would be systematically lower than those

observed at negative Sheet latitudes for the case in which the Sun is offset from the plane of the WHIM, resulting in a decrease in the equivalent width over all csc(θ') values. Since the WHIM is symmetric about z=0, a modified version of equation 2.19 was used when integrating over all path lengths through the Sheet in order to calculate the equivalent width as a function of csc(θ'):

$$\int_0^{\mathcal{L}} \exp\left\{-\frac{\left(\lambda-\left[\lambda_o\left(1+\frac{H_o\ell}{c}\right)\right]\right)^2}{2\sigma^2}\right\} n_{O^{5+}}(l)\,d\ell \qquad [2.20]$$

$$= \int_0^{h} \exp\left\{-\frac{\left(\lambda-\left[\lambda_o\left(1+\frac{H_o z}{c\,\sin(\theta')}\right)\right]\right)^2}{2\sigma^2}\right\} \frac{n_{O^{5+}}}{\sin(\theta')}\,dz$$

The results for both the 11 and 14 Mpc sheets are plotted in Figure 2.15.

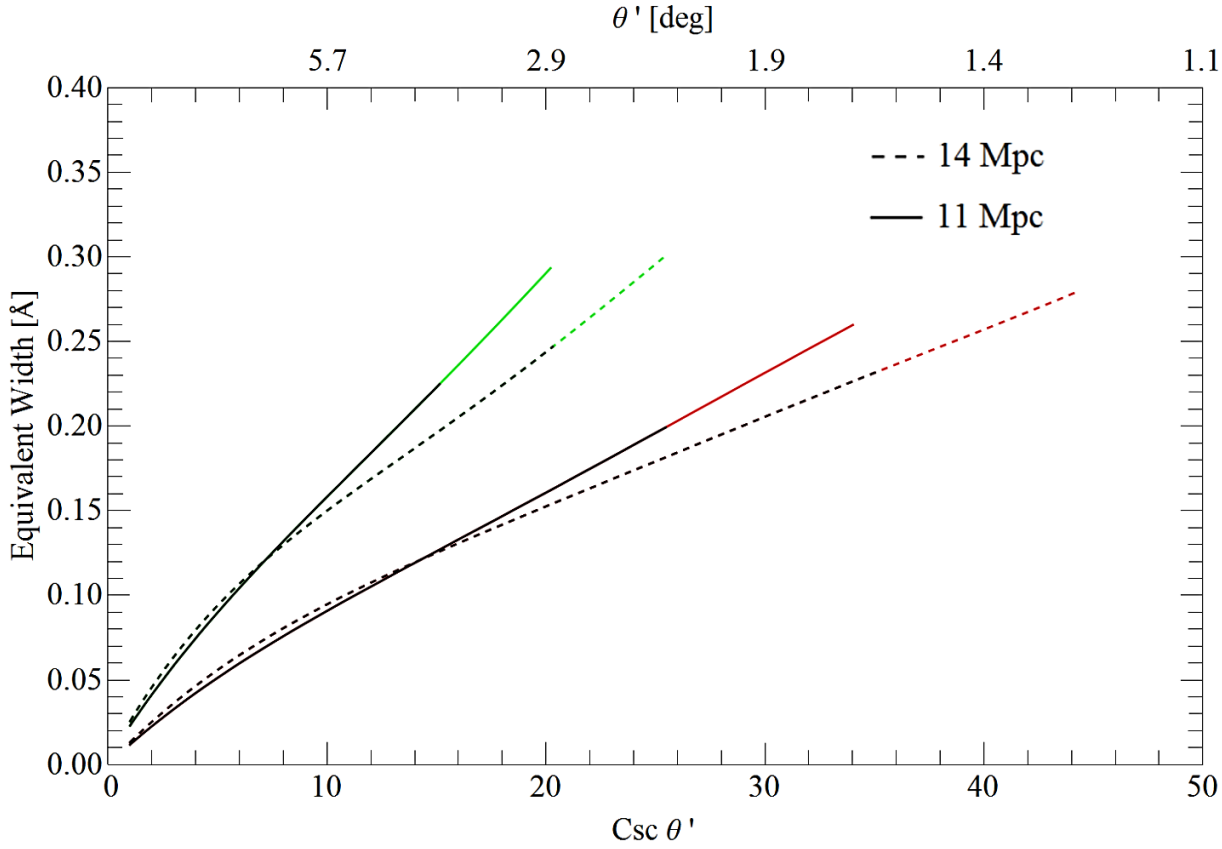

Figure 2.15: Theoretical equivalent widths as a function of the cosecant of the absolute value of the Sheet latitude with the Sun in the mid-plane of the WHIM. The csc(θ') axis range is set by θ'_{min}. The black lines apply to all ϕ', while the red lines apply only to ϕ' values where θ' exceeds θ'_{min}. The bottom plot of Figure 2.11 is plotted in green for comparison.

An additional consideration is that the number density profile of OVI absorbers may not be as uniform as was assumed in sections 2.1 and 2.2.1. It could be that the O^{5+} gas associated with the WHIM is distributed in clumps at varying distances and positions. Hubble broadening would disappear if there were a dense clump of O^{5+} gas confined to a narrow range of redshift. Additionally, clumping could result in the appearance of several OVI absorption lines along a given line-of-sight, separated in redshift. The problem with clumps is that it is hard to differentiate them from O^{5+} gas associated with the Milky Way, especially if the redshift is low.

If there truly are clumps of OVI absorbers that are associated with the WHIM, the best way to go about differentiating them from the Milky Way absorbers would be to look for differences

between spectra taken at negative and positive latitudes. It was predicted in section 2.1 that absorption should be weak along lines-of-sight towards positive latitudes because of the Sun's offset from the WHIM mid-plane. If there were multiple OVI absorptions along sightlines with a negative latitude versus few to none for the positive latitudes, that may be taken as evidence of clumps of O^{5+} that are associated with the WHIM rather than the Milky Way. Additionally, by correcting redshifts for the orbit of the Sun around the Milky Way centre, it may be possible to differentiate between clumps that are associated with the Milky Way and those associated with the WHIM.

Chapter 3

Data Selection and the FUSE Instrument

3.1 Data Selection

It has been over 7 years since the FUSE telescope was last operational, so it is no longer possible to make new observations for the purpose of this study. For this reason, past FUSE data that have since been made publicly available in the anonymous ftp area, archive.stsci.edu (Dixon et al. 2007), were used to conduct our survey of the WHIM in the Local Sheet.

The goal when selecting data for this research was to include as many extragalactic targets as possible over the largest possible range of Sheet latitudes, the reason simply being to seek out systematic evidence for the WHIM. The only restriction was that galaxies found within the Local Sheet be excluded. In total, spectra for of 331 distant galaxies and quasars were selected for study.

3.2 FUSE

The FUSE spectrograph consisted of four separate optical channels, each comprised of a mirror, a diffraction grating, and a far UV detector (see Figure 3.1). Each of the constituent mirrors was an off-axis paraboloid, with a 352 x 387 mm clear aperture, a 2245 mm focal length, and a 5.5^{o} off-axis angle. The corresponding diffraction gratings were holographically ruled and of the Rowland circle design with a diameter of 1652 mm. The two detectors that were used were double-delay line (DDL) detectors, which collected the incoming photons and measured their corresponding positions (Moos et al. 2000). In order to cover the entire spectral region of interest with high resolution, the optics in two of the channels were coated with silicon carbide (SiC), which optimally reflects at wavelengths less than 1000Å, while optics in the other two channels were coated with aluminum (Al) and lithium fluoride (LiF), which are optimized to reflect wavelengths greater then 1000Å. Spectra from both a SiC and a LiF/Al channel were imaged onto each detector, offset from each other perpendicular to the dispersion direction so as to make sure that they did not overlap with one another. Having two functionally independent segments for each of the detectors allowed for the ability to individually optimize them, and additionally gave the insurance that if one segment were to fail, the other would remain unaffected. With the four separate optical channels, along with the two detector segments, the result was a total of eight spectral segments which spanned a wavelength range of 905.0 to 1187.7 Å. Of these eight segments, four of them cover a wavelength range that includes the OVI absorption doublet of interest to this study. These segments are labeled LiF1A, LiF2B, SiC1A, and SiC2B, where the number and letter after the coating name refers to the detector and the detector segment, respectively. The full spectral ranges of each of the four segments of interest can be seen in Table 3.1.

Table 3.1: Relevant FUSE detector segments and their spectral ranges (Moos et al. 2000).

Detector Segment	Wavelength Range (Å)
LiF1A	988-1083
LiF2B	979-1075
SiC1A	1003-1090
SiC2B	1016-1104

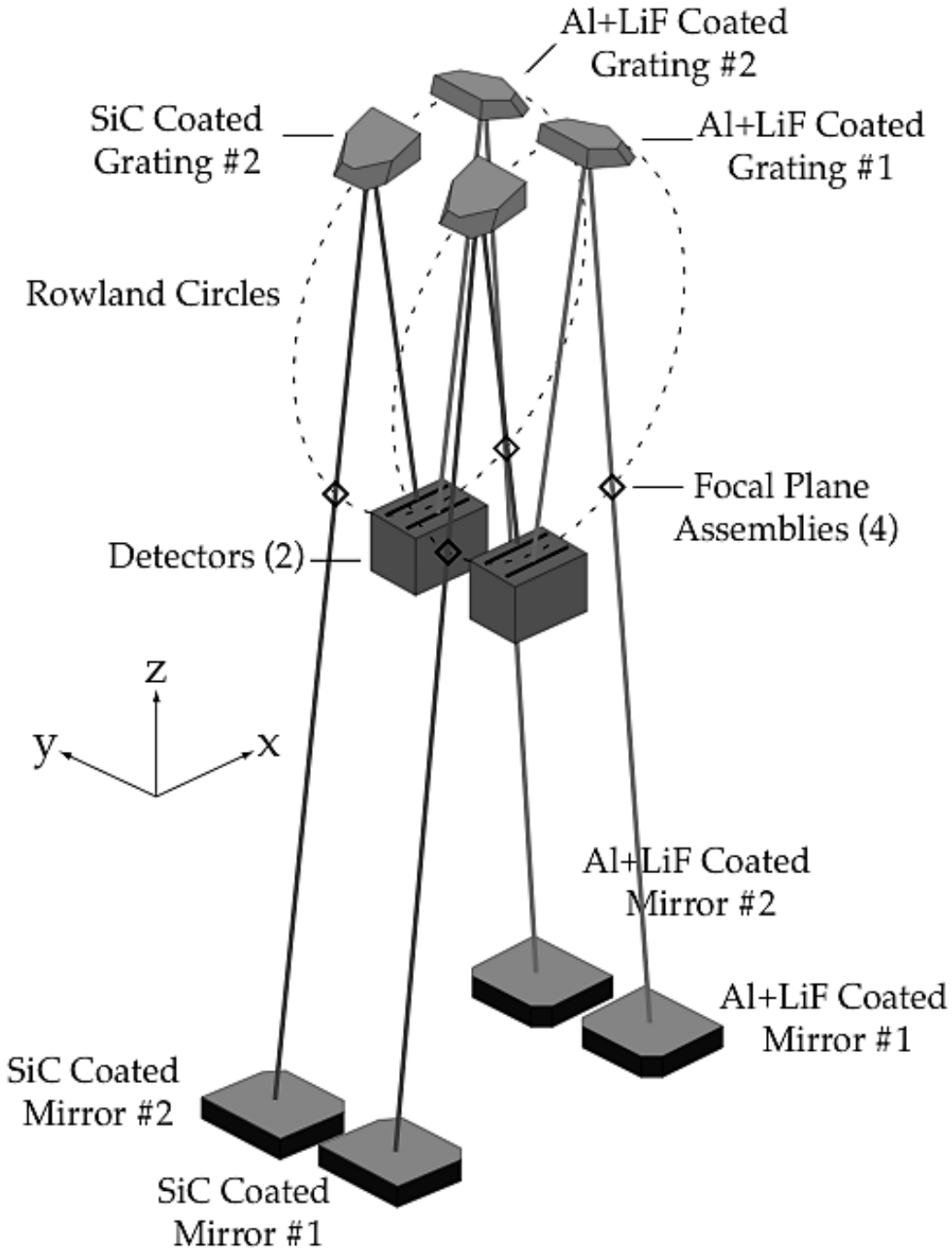

Figure 3.1: FUSE telescope optical design (Moos et al. 2000).

The original idea behind having four detector segments covering the same spectral region was not only to compare and contrast spectral features, but with the added intention of combining segments to achieve a higher signal-to-noise ratio. Unfortunately, however, small

motions in the mirrors and gratings due to thermal effects worked to smear out the spectra along the dispersion direction in a way that was unique to each of the different segments. This effect, along with the relative differences in spectral resolution for each of the segments, resulted in combined spectra with a degraded spectral resolution, albeit with an increased signal-to-noise ratio. On top of this, there were additional sources of error when combining the different spectra that were a direct result of the uncertainties involved in aligning the segments. These errors lead to further degradation of both the signal-to-noise ratio and the resolution of the spectra. In fact, Wakker et al. (2003) found that when the uncertainties in the spectral alignment were large, as is the case for segments with a low signal-to-noise ratio, the result was a combined spectrum with a signal-to-noise ratio that was actually less than that of the highest-quality original.

This research is focused on finding and measuring OVI absorption lines. This is done by fitting the lines with a profile function and extracting the necessary measurements from the parameters of the fit, which is always possible so long as the line exists. What it means for a line to exist is essentially related to a confidence level that is set by the signal-to-noise ratio of the line. If, for example, a line composed of one pixel has a signal-to-noise ratio of 3σ, where σ is the standard deviation of the noise in the continuum, then one could claim with 99.8% confidence (based on a Gaussian normal distribution) that the line is indeed real, and that it is not due to the noise in the continuum. As the signal-to-noise ratio becomes worse and worse, certainty as to the existence of the line will rapidly diminish. It is up to the researcher to determine what a reasonable certainty cut-off, below which a line can no longer be said to exist with any certainty, would be for their particular data. It is in this case, where the existence of a line is becoming uncertain, that it would be particularly valuable to be able to combine segments together in order to increase the overall signal-to-noise ratio of the data, in the hope that it may pull out a line that would otherwise be buried in the noise of the spectrum. However, Wakker et al. (2003) have shown that combining segments of low signal-to-noise ratio only serves to further

reduce the quality of the spectrum. It is easy, therefore, to conclude that combining multiple spectral segments would not be helpful to our research, as it does not promote the identification and fitting of lines.

Since we chose not to combine the different segments, we therefore had to choose the one segment that offered the best spectral data with which to make our measurements. In general, the SiC segments have a much lower signal-to-noise ratio than the LiF/Al segments simply because they are less sensitive to wavelengths beyond 1000 Å. For this reason, no data from the SiC segments were used. Of the two remaining LiF/Al segments, the LiF1A segment offers a slightly higher signal-to-noise ratio of about 1.4 times that of the LiF2B segment (Wakker et al. 2003). Additionally, the resolution of the LiF1A segment is on the order of 20km/s (Wood et al. 2002), which is again slightly higher than that of the LiF2B segment, which is 22km/s. Thus, the LiF1A segment was regarded as providing the optimal data for this research and, as such, all of the data presented in this thesis was taken from it.

Chapter 4

Data Processing and Measurements

4.1 Processing

All data recorded by FUSE were pre-processed by the principal investigator team at the Johns Hopkins University using a suite of computer programs called CalFUSE. After removing instrumental effects, extracting spectra, and applying wavelength and flux calibrations, CalFUSE outputs final spectra (flux versus wavelength) suitable for analysis. Upon the termination of the FUSE instrument operations, all of the existing FUSE data were re-processed using the final version of CalFUSE, version 3.2.3 (Dixon et al. 2007), and so any issues with past versions of CalFUSE were amended. CalFUSE, however, is not perfect and so the program has been made publicly available so that researchers can examine and customize the pipeline to best fit their goals. Specifically, CalFUSE is not optimized for very faint or extended targets (Dixon et al.

2007). For this research, we did not make modifications to the CalFUSE pipeline since we are concerned with what are mostly bright point-source targets.

The FUSE instrument followed a low-Earth orbit at an altitude of between 752 and 767km with a period of roughly 100 minutes (NASA). Since FUSE exposures could be on the order of tens of kiloseconds in length, there would be moments when Earth would get in the way of a target during the time in which it was being observed. In order to combat this, long exposures were broken apart into "chunks". In the FUSE database, exposure "chunks" are provided and it is left up to the user to combine them into a single spectrum. Although the CalFUSE pipeline placed all spectra on a heliocentric wavelength scale, it is very possible that small shifts in the wavelength scales between the different exposures remain due to the jitter experienced by the spacecraft as it moves through its orbit. Fortunately, they are, for the most part, counteracted by the CalFUSE pipeline. In an attempt to remove any residual shifts, the individual exposures were cross-correlated before being summed. Whether or not it was possible to do a cross-correlation was set by the strength of features common to the individual exposures. The quality of the features was determined by eye, and so any feature that was not easily identifiable would be decidedly insufficient to use in a cross-correlation. In the cases where there were no strong features present, the individual exposures were simply summed without any shift and the result was taken to be the final spectrum. If, however, cross-correlation was found to be possible, then each of the constituent exposures was shifted in wavelength towards the mean of the feature position. For example, if there were 4 exposures and a particular feature that they all shared was present at 1020 Å, 1021 Å, 1023 Å, and 1018 Å, then the respective spectra were shifted in wavelength to move the feature to 1020.5 Å.

Any and all cross-correlation was done using the FXCOR task in IRAF, which is a standard Fourier cross-correlation task based on the standard Tonry and Davis algorithm (Tonry and Davis 1979). By specifying one of the exposures as a template image and giving a range over

which to do the cross-correlation, the FXCOR task would return the corresponding shifts in wavelength space with respect to the template image.

In addition to the multiple exposures that could make up a single observation of an object, there is the additional possibility that the object could have been observed on more then one occasion. Consequently, there could be multiple data sets, each with their own set of exposures. Just as with the individual exposures for a single pointing, it is entirely within reason that these separate observations could be added together as well, resulting in a final spectrum that contains all of the recorded FUSE data for the object. Thus, spectra from different pointings were also cross-correlated when possible and summed. Spectra for which a cross-correlation was performed were shifted in wavelength so that they were aligned with the mean wavelength of the individual alignment features. For objects lacking features strong enough to cross-correlate, we simply summed the data sets without performing any shifts.

In all, spectra could be generated for 107 targets. Note that this number is much less than the original sample size of 331 targets. This is because any spectrum with an extremely low signal (bottoming out at zero intensity) or with anomalous behaviour such as periodic spikes in intensity, was removed, the reason simply being that the signal was either too weak to provide any information about the OVI absorption lines or downright unreliable. Evidence for OVI absorption was seen in 90 targets, while another 17 seemed to lack OVI absorption (or there was too much contamination present to identify any OVI absorption). The latter provide useful upper limits to OVI absorption along their respective lines of sight. Information about the sample, including the data set IDs and exposure times, is included in Appendix A (Table A.1).

The final step in the processing of the FUSE spectra was to bin the data in wavelength space. As previously mentioned, the resolution of the FUSE instrument is on the order of 20 km/s, or 0.069 Å. Pixels are spaced 0.013 Å apart, meaning that there are roughly 5 pixels per resolution

element. The Sampling Theorem states that the rate at which a periodic function should be sampled must be greater than or equal to twice the frequency of the function if there is to be no loss of information. This means that a resolution element only needs to be sampled twice, implying that only half of the FUSE pixels per resolution element are actually required and that the other half are redundant. For this reason, all spectra were binned with a bin size of two pixels, or 0.026 Å, so as to improve the signal-to-noise ratio without compromising information about line profiles.

4.2 Defining the Continuum

The continuum of a spectrum refers to the continuous background intensity of a target without the presence of absorption or emission lines. Emission and absorption lines add to and subtract from the continuum, and so any measurements of spectral features must be made with respect to the continuum. Before measurements of spectral lines could be accomplished, the continuum had to be rectified and normalized to unity. This was done using the IRAF task “continuum”. By identifying different regions of the spectrum devoid of any spectral features as the continuum, the IRAF task would fit a pre-defined function to them and normalize the spectrum. The shape of a spectrum’s continuum is dependent on many factors, including instrumental effects. For this reason, a cubic spline function was chosen to fit the data as it proved to work well with the relatively linear continua that were common, while also being able to follow any curvature, however subtle. The IRAF continuum task would divide the original spectrum by the fit to the continuum, resulting in a normalized spectrum with the continuum level at unity.

Appendix B presents the reduced and continuum-normalized spectra, complete with the identification of and fits to absorption lines (see below).

4.3 Removing Contaminants

There are several possible sources of spectral contamination that could potentially affect a line of OVI. If a spectrally proximate, but otherwise unrelated absorption line appeared near to the rest wavelength, the equivalent width and shape of the OVI line would increase, possibly leading to false conclusions. In order to combat this, all possible forms of contamination must be examined. The most important sources of contamination are: the interstellar medium of the Milky Way; nearby galaxies; the targets themselves. Each is dealt with in detail in what follows.

4.3.1 Interstellar Contamination

Interstellar contamination arises from molecular hydrogen (H_2) and other trace constituents of the nearby interstellar medium that happen to have absorption features close enough to the OVI absorption lines to possibly contaminate them. This form of contamination can effect either of the OVI absorption lines to some degree, but it is much more detrimental to the detection of the 1037.617 Å line. There are a total of three hydrogen absorption lines, namely 5-0 R(1) at 1037.146 Å, 5-0 P(1) at 1038.156 Å, and 5-0 R(2) at 1038.690 Å, along with a CII line at 1037.018 Å, that could contaminate the line. Because of the large number of possible contaminants, coupled with the relative weakness of the 1037.617 Å OVI line when compared to the 1031.926 Å OVI line, the 1037.617 Å OVI line was only used to corroborate the identification of the 1031.926 Å OVI line. Only the stronger 1031.926 Å OVI line was used in our analyses.

Interstellar H_2 absorption also can appear near to the 1031.926 Å OVI line in the form of two lines, 6-0 P(3) and 6-0 R(4), which are located at wavelengths 1031.191 Å and 1032.356 Å, respectively. Since these lines are so close to the rest wavelength of the 1031.926 Å OVI line, any small redshift or blueshift introduced by the relative velocities of the intergalactic and

interstellar media could result in overlap. Having half the number of interstellar contaminants, coupled with the greater strength of the 1031.926 Å OVI line, removal of the interstellar contamination is much more manageable then for the 1037.617 Å line.

The first step in identifying/removing H_2 contamination was to find the highest rotational level of H_2 (J) for which there was absorption in the particular spectrum being examined. For J values of 4 or greater, both 6-0 R(4) and 6-0 P(3) must be present, for J=3 only 6-0 P(3) must be present, and for J<3 neither line is present. The highest value of J was determined by looking over the entire range of the spectrum. The rotational line list was adopted from Morton and Dinerstein (1975). The largest J value that was found was referred to as the "J value for the spectrum". The J value for each target can be found in Appendix A (Tables A.2, A.3, and A.4). Note that any spectrum with a J value greater than 4 is listed as having a J value of 4.

If a spectrum was found to have a J value of 3 or greater, then the next step was to see if the H_2 lines 6-0 P(3) or 6-0 R(4) could be identified by eye. If it was possible to identify the expected H_2 lines then the lines were left to be fitted simultaneously along with the OVI lines, after all other contamination has been dealt with. This was done to avoid any negative effects one feature may have had on the accuracy of the fit of the other. The fit to the H_2 lines was done using a Gaussian absorption profile, which was defined in section 2.2.1 in equation 2.16. Mathematica 8 was used to do the fits, specifically using the NonlinearRegress package.

There were situations where, upon visual inspection, it was apparent that the H_2 lines were not distinct and that they overlapped with a possible OVI absorption feature, or where the overlap was so severe that the H_2 line was not even visible. When the contamination was so severe as to completely overlap with the OVI absorption, the only way to remove it was by creating a pseudo H_2 line based upon other uncontaminated H_2 lines with the same J value in the same spectrum. To do this, each of the other H_2 lines was fit with a common Gaussian

absorption profile (equation 2.16). By scaling the fit parameters by the oscillator strengths of the individual lines, an average Gaussian absorption profile was created for that J value. A pseudo H_2 line was then constructed, scaling by the oscillator strength of the H_2 line contaminating OVI. The spectrum was then divided by this pseudo H_2 line to remove the overlapping contamination.

4.3.2 Contamination from Nearby Galaxies

The second source of contamination comes in the form of OVI absorption from nearby galaxies. If the line of sight between FUSE and a distant target happens to pass near a local galaxy, absorption by O^{5+} gas associated with that galaxy may contaminate the OVI absorption from the WHIM. In order to determine whether or not such contamination was possible, it was first important to define the radius out to which O^{5+} gas associated with a galaxy might extend. Prochaska et al. (2011) present data from FUSE and the UV-sensitive spectrometers on the Hubble Space Telescope (HST) that can be used to determine how the equivalent widths of OVI absorption lines depend on the proximity of the line-of-sight to an intervening galaxy. By looking at how the equivalent widths of the lines depend on the impact parameter, it is possible to constrain an upper limit for the extent of the galactic O^{5+} gas in general.

The data set from Prochaska et al. (2011) contains galaxies of various sizes, and so it would be nonsensical to examine the equivalent width as a function of the impact parameter in absolute units. The impact parameter must be scaled by the size of the intervener in order to be able to compare absorption introduced by different galaxies. Scaling was accomplished by using the virial radius.

The virial radius of a galaxy is defined by the virial theorem, which states that the total kinetic energy of a self-gravitating system of particles in gravitational equilibrium is directly proportional to the gravitational potential energy of that system. In particular, the gravitational potential

energy of a system in virial equilibrium is equal to twice the total kinetic energy of that system. The kinetic energy has two components: that due to the rotational velocity and that due to the velocity dispersion brought upon by random motions. The temperature dependent velocity dispersion is

$$\sigma = \sqrt{\frac{3}{2}\frac{kT}{m_p}} \quad [4.1]$$

where m_p is the proton mass. Substituting the sum of the velocity dispersion and the rotational velocity, ω, into the expression for the kinetic energy (which is the sum of the rotational and translational components),

$$\frac{1}{2}\sum m\,\sigma^2 + \frac{1}{2} I\omega^2 \quad [4.2]$$

and equating that to half the gravitational potential energy leads to

$$3\sigma^2 + \frac{I}{\sum m} v^2 = \frac{GM}{R} \quad [4.3]$$

Here v is the average rotational velocity, σ is the average radial velocity dispersion, I is the moment of inertia of an ensemble of all particles, m is the mass of a packet of particles, M is the mass contained within the radius R, and G is Newton's gravitational constant.

Equation 4.3 can be used to define a virial mass, M_{vir}, and radius, R_{vir}, that can be used to universally and equally describe any given galaxy. Specifically, assuming most kinetic energy is in the form of random motions,

$$3\sigma^2 = \frac{GM_{vir}}{R_{vir}} \quad [4.4]$$

Knowledge of the virial mass of a galaxy, be it theoretical or observational in nature, can be used with the velocity dispersion to calculate the virial radius.

The virial radius can be defined in terms of a characteristic luminosity, L*. The characteristic luminosity is, in turn, defined by the Schechter Function, which gives the number of galaxies per unit luminosity per unit volume as a function of the luminosity:

$$\phi(L) = \left(\frac{\phi^*}{L^*}\right)\left(\frac{L}{L^*}\right)^{\alpha} \exp\left[\frac{-L}{L^*}\right] \quad [4.5]$$

Here ϕ^* is the normalization density and α is the power law slope at low L. L* is defined as the luminosity at which the power-law form of the function breaks. The parameter α can take on different values for different populations and environments, however it is always negative.

Prochaska et al. (2011) make predictions for the virial radius for different galaxy types based on mass-luminosity relations for dark matter haloes. For low-luminosity galaxies and dwarf galaxies, they adopt a value on the order of 100 kpc. For brighter, but still sub-L^* galaxies, they adopt a value on the order of 160 kpc, and for L^* galaxies, they adopt a value on the order of 250 kpc. They relate the virial radius of an L^* galaxy to the virial radius of an arbitrary one,

$$R_{vir} = R^*_{vir}\left(\frac{L}{L^*}\right)^{\beta} \quad [4.6]$$

Here L is the luminosity, β is a dimensionless constant, and the * superscripts refer to values that correspond to a typical L^* galaxy. β is defined by how virial radii vary with luminosity. Prochaska et al. (2011) adopt a value of 0.2.

By plotting the equivalent width of OVI absorption as a function of the impact parameter, ρ, normalized to the virial radius, it is possible to determine how far the line of sight to a background target must be from a nearby galaxy in order for its spectrum not to be contaminated by associated OVI absorption. Equivalent widths of OVI lines are plotted versus normalized

impact parameters in Figure 4.1. Relationships are plotted for three luminosity ranges. The observations suggest that to avoid significant contamination by an intervening galaxy, $\rho \geq \rho_{\min} = 2.0R_{\rm vir}$.

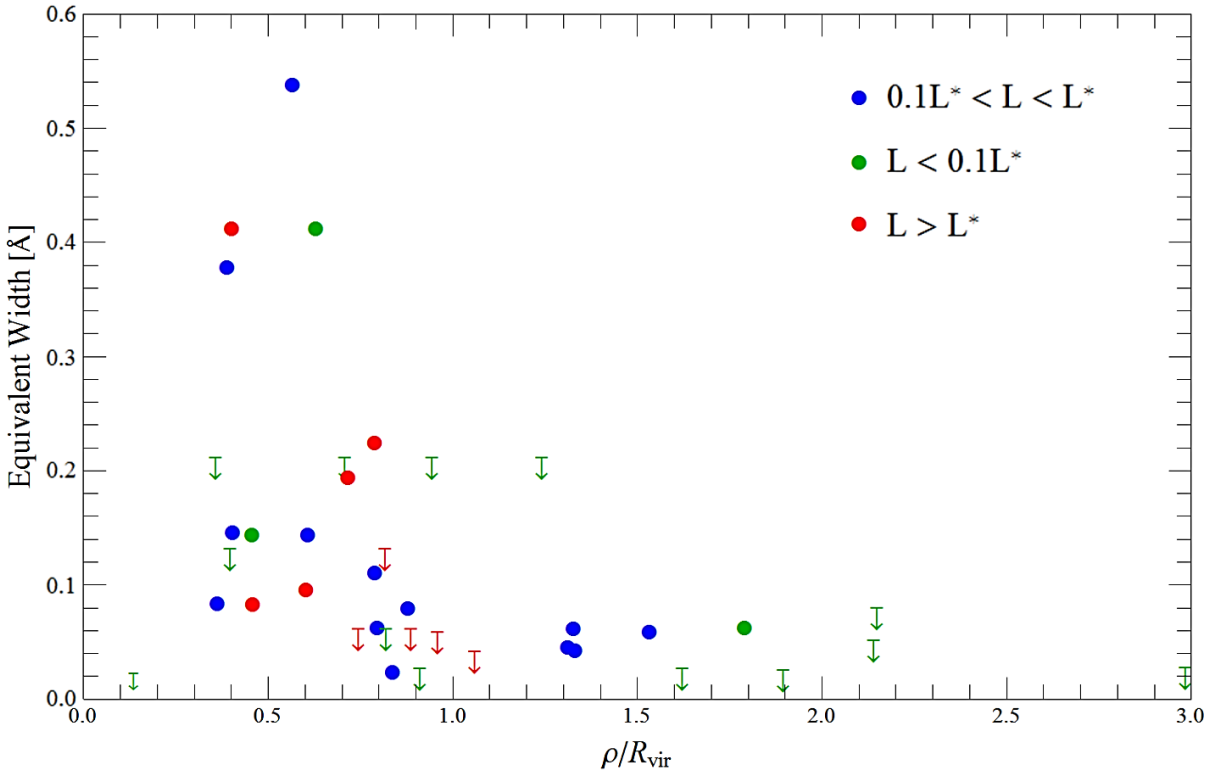

Figure 4.1: Equivalent width versus impact parameter normalized to the virial radius for intervening galaxies. Closed circles represent detections and downward pointing arrows represent upper limits.

In order to identify whether or not there is nearby galactic contamination, $\rho_{\min}$ for each intervening galaxy must be expressed in angular units so as to be easily compared with the positions of the targets. In order to do this, the distance must be taken into account. Using simple geometry, the angular impact parameter of a galaxy can be calculated as follows:

$$\psi_{min} = \arctan\left[\frac{\rho_{min}}{D}\right] = \arctan\left[\frac{2R_{vir}}{D}\right] \qquad [4.7]$$

Here ψ_{min} is the angular value of the impact parameter and D is the distance to the target object.

For each target, α_{min} was computed for every possible intervening galaxy within 11 Mpc of the Milky Way. The Updated Nearby Galaxy Catalog (Karachentsev et al. 2013) provided distances and absolute B magnitudes, the latter of which could be used to solve for the luminosity relative to L*:

$$\frac{L_B}{L_B^*} = 10^{\frac{M_B^* - M_B}{2.5}} \quad [4.8]$$

Here $\mathrm{M_B^*}$ is the absolute B magnitude of a galaxy with characteristic luminosity L* in B.

The value for $\mathrm{M_B^*}$ used in equation 24 was calculated from $\mathrm{M_{Bj}^*}$, the photographic B magnitude. Norberg et al. (2008), found $\mathrm{M_{Bj}^* - 5log_{10}h = -19.66 \pm 0.07}$, where h is the Hubble parameter. In order to endure that $\mathrm{L_B/L_B^*}$ is independent of distance, the Hubble parameter was adopted to be that used in the Updated Nearby Galaxy Catalog, which was 0.73 (Karachentsev et al. 2013). Norberg et al. (2002) show that

$$M_B^* = M_{Bj}^* + (0.267 \pm 0.019)(B-V)^* \quad [4.9]$$

where (B-V)* is the average B-V colour for an L* galaxy. Adopting (B-V)* to be 0.7, the value for $\mathrm{M_B^*}$ obtained from equation 4.9 is -20.16 ± 0.08. Virial radii of the galaxies within 11 Mpc followed by substituting equation 4.8 into equation 4.6. Then, equation 4.7 yielded the angular impact parameters.

Through the use of spherical trigonometry, the angular distance, ψ, between each of the targets and the catalogue galaxies was found from their supergalactic coordinates:

$$\psi = \arccos[\sin(B_c)\sin(B_t) + \cos(B_t)\cos(L_c - L_t)] \quad [4.10]$$

Here B_c is the supergalactic latitude of the catalogue galaxy, B_t is the supergalactic latitude of the target, L_c is the supergalactic longitude of the catalogue galaxy, and L_t is the supergalactic longitude of the target.

If the angular distance between a target and a catalogue galaxy was less than ψ_{min}, then there was a possibility that there could be some form of spectral contamination from the galaxy. However, if the intervening galaxy was a dwarf spheroidal or dwarf elliptical galaxy, it was assumed that there would be no significant contamination. By mass, there is very little gas associated with dwarf galaxies in general, and even less is expected to be O^{5+}. Additionally, observations of escape velocities suggest that gas lost from dwarf spheroidal galaxies is much colder and less highly ionized than that of the WHIM, implying that the abundance of O^{5+} ions was minuscule (McCall et al. 2012; McCall 2015, personal communication). Dwarf irregulars, however, are actively forming stars, so O^{5+} gas may be present as the result of supernova explosions. Thus, dwarf irregulars were included as possible sources of OVI contamination. Only massive galaxies have a sufficiently deep gravitational well for gas to be heated globally to a high enough temperatures to produce O^{5+} ions in abundance. If the redshift of such a galaxy was found to be within the full width at half maximum of an identified OVI absorption feature (determined from fits to the lines as discussed in Section 4.4), then that feature was considered to be contaminated and was removed from the final compilation of OVI measurements suitable for investigating the WHIM in the Local Sheet.

In total, there were 26 contaminated targets and 29 contaminated OVI absorption features. Table 4.1 lists the contaminated targets, the velocities of the OVI absorption features identified as possible contaminants, the catalogue galaxies that are the source of the contaminants, and the velocities of the contaminating galaxies.

Table 4.1: Contaminated targets and their corresponding contaminating galaxies.

Contaminated Target Name (1)	Target Type	Velocity of Contaminated OVI Absorption Line (km/s) (2)	Contaminating Galaxy Name	Velocity of Contaminating Galaxy (km/s)
TONS180	Galaxy	270.37 ± 13.08	NGC0253	243
			DDO006	292
			LMC	278
VIIW118	Galaxy	-23.26 ± 9.05	IC0342	29
			UGA092	-95
PG1259+593	QSO	14.54 ± 13.16	ESO384-016	150
			DD0190	-57
3C273	QSO	8.72 ± 12.81	NGC6822	-57
MKN59	Galaxy	-40.70 ± 4.13	DD0190	-57
TON28	QSO	34.89 ± 6.31	IC2574	24
			DDO084	43
MRK734	Galaxy	84.31 ± 10.23	NGC4449	201
			DDO133	134
			KK151	-57
PG1307+085	QSO	-20.35 ± 11.28	NGC6822	-57
MRK54	Galaxy	-20.35 ± 9.46	DDO190	-57
MRK79	Glaxy	2.91 ± 0.94	DDO053	19
PG1116+215	QSO	29.07 ± 14.01	UGC07639	-57
PG1211+143	Galaxy	34.89 ± 11.12	NGC6822	-57
T1247-232	Galaxy	75.59 ± 2.67	DDO120	140
HE0226-4110	Galaxy	5.81 ± 53.18	SMC	-52
		203.50 ± 7.55	Phoenix	158
			LMC	278
IRAS_F22456-5125	Galaxy	212.22 ± 2.76	SMC	158
			LMC	278
NGC1068	Galaxy	290.72 ± 1.60	SMC	158

			LMC	278
2MASX-J21362313-6224008	Galaxy	40.70 ± 11.65	SMC	158
PKS0405-12	QSO	23.26 ± 8.09	SMC	158
PKS2005-489	QSO	49.42 ± 2.40	SMC	158
MRK509	Galaxy	313.98 ± 5.22	SMC	158
PKS0558-504	QSO	290.72 ± 12.23	SMC	158
			LMC	278
ESO265-G23	Galaxy	90.12 ± 1.29	SMC	158
		276.18 ± 14.66	LMC	278
MRK1044	Galaxy	360.49 ± 5.03	LMC	278
PG2349-014	QSO	66.87 ± 0.60	SMC	158
NGC7714	Galaxy	58.14 ± 1.03	SMC	158
HE0238-1904	QSO	20.35 ± 4.82	SMC	158
		206.41 ± 6.44	SMC	158
			LMC	278

1) The FUSE designations are given for the target names.
2) The velocities and their errors were obtained from the OVI absorption line fitting process (see Section 4.4).

4.3.3 Target Contamination

Since we are making use of distant sources of light such as quasars to probe the WHIM in the Local Sheet, we must consider the possibility that an absorption line associated with the target may be redshifted by the Hubble flow to the wavelength of OVI absorption from the WHIM. Contamination of this kind had to be dealt with on a case by case basis since it is completely dependent on the redshift of the target being observed.

In order to identify possible contaminating lines, a database of atomic spectra (NIST 2014) was used. By taking the redshift of each of the targets, as given in Appendix A (Tables A.2, A.3,

and A.4), and shifting spectral lines accordingly, it could be seen whether or not any of the lines in the NIST database would be shifted into the region near the OVI absorption lines. If it was found that one of these features was indeed shifted onto or near the OVI absorption line, then the target spectrum was inspected by eye to see if the feature could be visually identified. If the line was present but visually distinct enough from OVI absorption, it was fitted simultaneously using a Gaussian absorption profile. If instead, the contaminating line was found to overlap with the OVI absorption line, it was impossible to separate it with confidence from intergalactic OVI absorption, so the measurement of OVI was excluded from the sample to be subjected to analysis.

With all of the possible OVI absorption line contamination identified, a total of 74 of the starting 90 targets were found to have contamination free OVI absorption lines, with a total of 100 OVI absorption lines identified. The heliocentric rotated Sheet coordinates of the 74 targets and the 17 upper limit targets are plotted in figure 4.2.

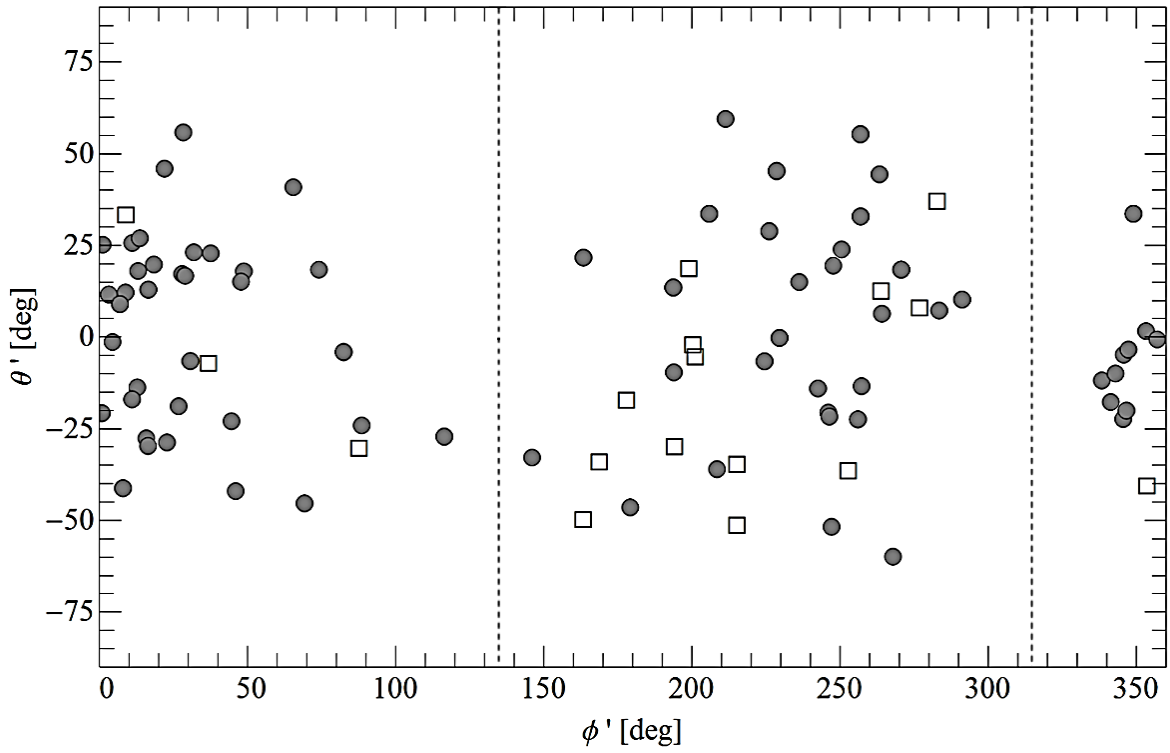

Figure 4.2: The heliocentric rotated Sheet coordinates of the 74 targets with OVI detections and 17 targets with upper limits are plotted with shaded circles and squares, respectively. The dashed lines represent the positions of the plane of the Milky Way.

The gaps where there are no observed targets in Figure 4.2 is clearly due to the presence of the plane of the Milky Way, where the dust of the Milky Way plane obscures observations along those lines of sight.

4.4 Fitting OVI Lines

Line shapes that can result at different latitudes from the O^{5+} number density profile of the WHIM can be complex. At any given point along the line of sight, thermal broadening transforms the natural Lorentzian profile into a near Gaussian. The Hubble flow broadens the Gaussian profile to have extended wings and a flattened base. A redward skew develops from the redshift bias. To model observed profiles of OVI lines well enough to characterize positions, widths, and asymmetries, a skew normal distribution was employed:

$$I_\lambda = I_o \exp\left\{-a \exp\left[\frac{-(\lambda - b)^2}{2c^2}\right]\left(1 + \operatorname{erf}\left[\frac{\kappa(\lambda - b)}{\sqrt{2}c}\right]\right)\right\} \quad [4.11]$$

Here a, b, c, and κ are all parameters to be fit. The skewed shape comes from the error function. The dimensionless parameter that determines the extent of the skew is κ, with a positive value corresponding to a redward skew and a negative value corresponding to a blueward skew. In the event that there is no skew present, $\kappa = 0$ and the error function goes to zero, resulting in the reduction of equation 4.11 to equation 2.16, a Gaussian profile.

Any spectrum may have multiple 1031.926 Å OVI absorption lines redshifted with respect to one another due to clumping in the WHIM or the relative motions of different absorption sources, such the Milky Way. If a contaminant or another OVI absorption feature was near to any of the feature being fit, there was a risk that simultaneously fitting would distort the magnitude of the skew parameter. For such a case, a Gaussian profile was employed instead. Once the appropriate function was determined for each OVI component, be it a Gaussian or skew normal distribution, all components were simultaneously fitted along with any previously identified extragalactic contaminants, and any interstellar H_2 lines that have not already been removed from the spectrum. Fit parameters for all of the spectra can be found in Appendix A (Tables A.2 and A.3).

4.5 Non-Detections and Upper Limits

It was not always possible to clearly detect OVI absorption features in a spectrum. For any such line-of-sight, an upper limit to the OVI line strength was estimated.

As mentioned in Section 3.2, the certainty with which one can determine a line's existence is determined by its signal-to-noise ratio. For a line that is defined by a single pixel, a signal-to-noise ratio of 3σ (where σ is the noise in the spectrum) implies a 99.8% chance of being a real

spectral feature rather than a consequence of random noise. If a line consists of more than one pixel, then the certainty with which it can be considered a real feature increases for a given signal-to-noise ratio. This increase in certainty is governed by the increase in sample size. If a line is sampled by a total of N pixels, the signal-to-noise ratio of 3σ that corresponds to a 99.8% confidence level for a single pixel will be reduced by a factor of $\sqrt{N}$, i.e., to $3\sigma/\sqrt{N}$.

The average line width (i.e., twice the standard deviation of a Gaussian) measured for the highest quality OVI detections was 12.67 ± 2.32 pixels Therefore, the minimum signal-to-noise ratio (per pixel) required to detect a line with 99.8% confidence was $0.84\sigma \pm 0.08\sigma$. For 17 spectra with a suspected OVI absorption feature with a depth below 0.84σ, the OVI feature was indistinguishable from contamination sources, or in which there appeared to be no OVI absorption feature at all, an upper limit for the equivalent width of OVI absorption was estimated using the average line width estimated above, and a line depth equal to 0.84σ. The limits are included in Appendix A (Table A.4).

Chapter 5

Analysis

5.1 Identifying OVI Absorption Associated with the WHIM

There is one source of contamination that still remains: absorption by O^{5+} gas in the Milky Way. In order to distinguish it, we looked for trends in the velocities of the OVI lines that are indicative of the relative motion of their source with respect to the Sun. If, for example, it is found that some or all of the OVI lines have velocities expected for the Milky Way with respect to the Sun (reflex of the Sun's motion in the Milky Way), then those lines may originate in the Milky Way, and must be rejected.

The motion of the Sun through space should make it possible to identify and differentiate between three sources of OVI absorption: the matter in the Milky Way at rest with respect to the Local Standard of Rest (LSR), the matter in the Milky Way at rest with respect to the Milky Way centre, and the matter in the Local Sheet at rest with respect to the Local Group. Each of these potential OVI absorption sources appears to move relative to the Sun with a velocity pointed toward a well-defined apex in the sky. The redshift varies sinusoidally with the angular distance

of the target from the apex, resulting in a redshift for a target in the direction of the apex and a blueshift for targets positioned on the opposite side of the sky. Table 5.1 gives the apex velocities and directions for the three OVI absorption sources (McCall 2014; McCall 2015, personal communication).

Table 5.1: Apex velocity information for possible OVI absorption sources.

OVI Source	Heliocentric Apex Velocity (km/s)	Heliocentric Rotated Sheet Latitude (deg)	Heliocentric Rotated Sheet Longitude (deg)
Matter at Rest with Respect to Local Standard of Rest	18.0	-65.28	215.63
Matter at Rest with Respect to Milky Way Centre	251.6	-46.09	137.91
Matter at Rest with Respect to Local Group	284.9	-40.23	132.31

The angular distances, δ, between the apices and the targets were calculated using the spherical cosine law,

$$\cos(\delta) = \cos\left(90 - \theta'_{apex}\right)\cos(90 - \theta') + \sin\left(90 - \theta'_{apex}\right)\sin(90 - \theta')\cos(\phi'_{apex} - \phi') \qquad [5.1]$$

where θ' and θ'_{apex} are the latitudes of the target and apex, respectively, and ϕ' and ϕ'_{apex} are the longitudes of the target and apex, respectively, all in the heliocentric rotated Sheet system.

Figure 5.1 plots the OVI velocities as a function of the angular distance from the apex of the LSR motion.

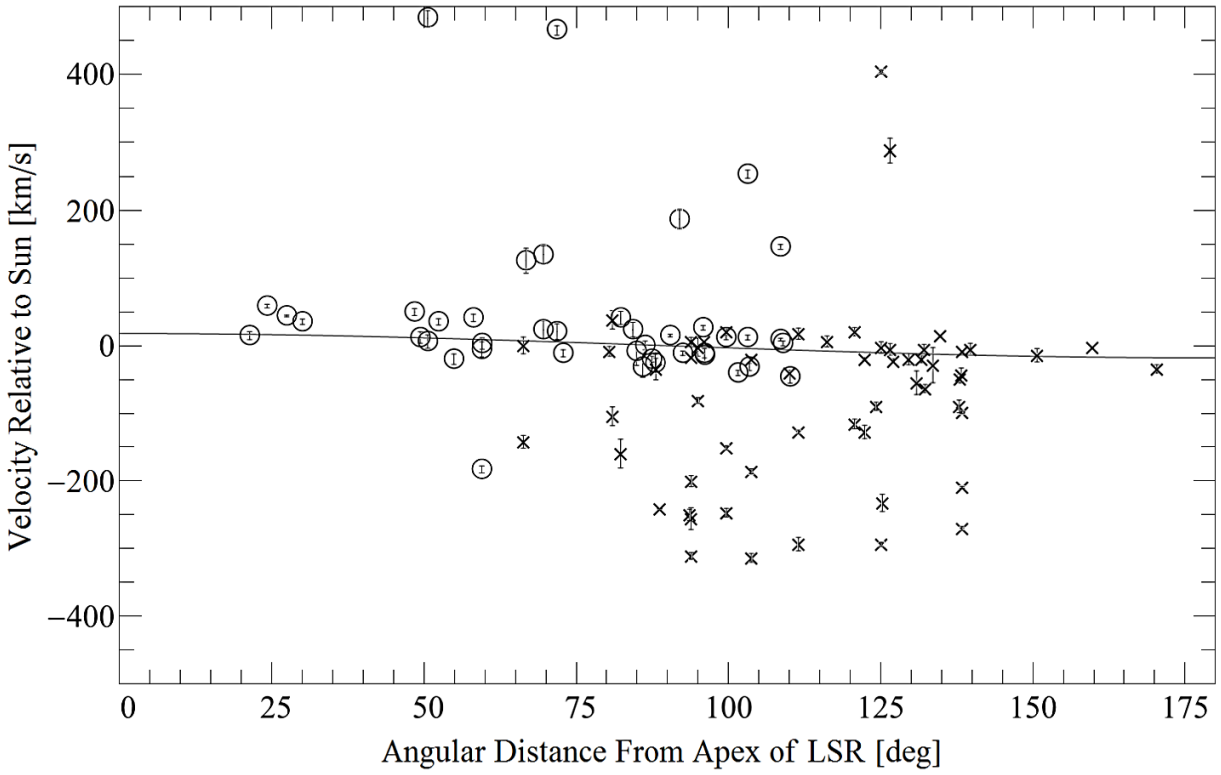

Figure 5.1: Velocities of the OVI absorption lines are plotted as a function of the angular distance of the target from the apex of the LSR's motion with respect to the Sun. The expected sinusoidal curve for absorbers moving with the LSR is plotted for comparison. Lines from positive Sheet latitudes are indicated by crosses and lines from negative Sheet latitudes are indicated by circles. Error bars derived from the fits are shown for all points.

It can be seen that the motion of the LSR with respect to the Sun overlaps with a large number of OVI absorption lines near zero velocity. This would suggest that these lines arise from a hot interstellar medium in the immediate vicinity of the Sun, and that they are not associated with the WHIM. In order to identify the OVI lines associated with the hot interstellar medium, the LSR's motion relative to the Sun was subtracted from the OVI velocities, which centered the velocities of the lines associated with the LSR about zero velocity (Figure 5.2). The standard deviation and mean of the velocities between -100 and 100 km/s were computed to be 28.8 km/s and -2.9 km/s respectively. All OVI lines that lay within 3 standard deviations of the mean were considered to be associated with the hot interstellar medium in the immediate vicinity of the Sun (see Figure 5.2).

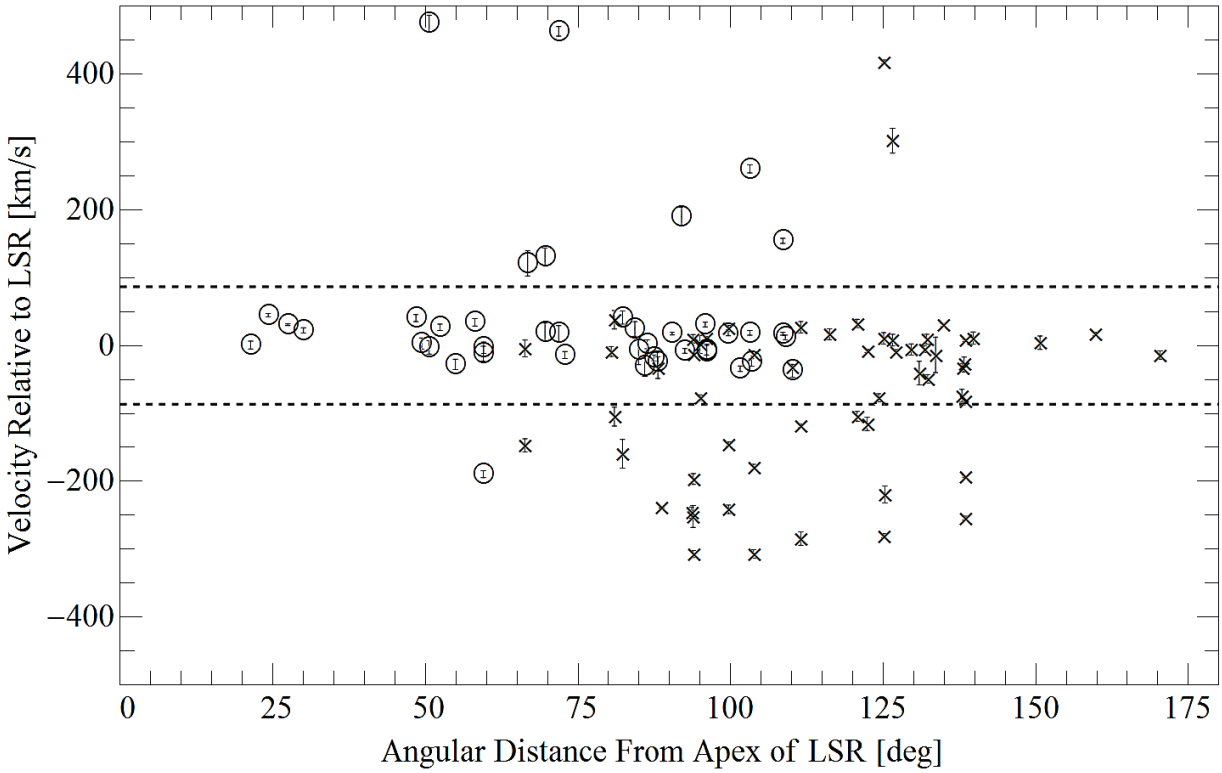

Figure 5.2: Velocities of the OVI absorption lines are plotted as a function of the angular distance of the target from the apex of the LSR's motion with respect to the Sun, after the motion of the LSR is subtracted. The region in which the OVI lines associated with the LSR were identified is bounded by the dashed lines. Lines from positive Sheet latitudes are indicated by crosses and lines from negative Sheet latitudes are indicated by circles. Error bars derived from the fits are shown for all points.

The predicted trend of equivalent width with $\csc(\theta')$ for the WHIM is largely defined by low-latitude lines, since the equivalent widths of lines at high latitudes are expected to be too small to be measured. Furthermore, as will be seen shortly, there may be lines genuinely from the WHIM which have velocities which overlap with those matter associated with the LSR. Therefore, rather than remove all OVI lines associated with the LSR, lines in targets with a latitude less then 30° ($\csc(\theta') \geq 2$) were retained, but expressed as upper limits to OVI absorption from the WHIM.

With the local OVI lines dealt with, the next possible OVI line source to be examined is matter at rest with respect to the Milky Way centre. Just as before, equation 5.1 was used to calculate the angular distances of the targets with respect to the apex of motion of the Milky Way centre

relative to the Sun. Figure 5.3 plots the heliocentric velocities of the OVI lines (excluding contaminants associated with the LSR) as a function of angular distance from the apex, along with the sinusoidal reflection of the motion of the Milky Way centre with respect to the Sun. The Figure reveals evidence that some of the absorbers with negative velocities may reside in the Milky Way.

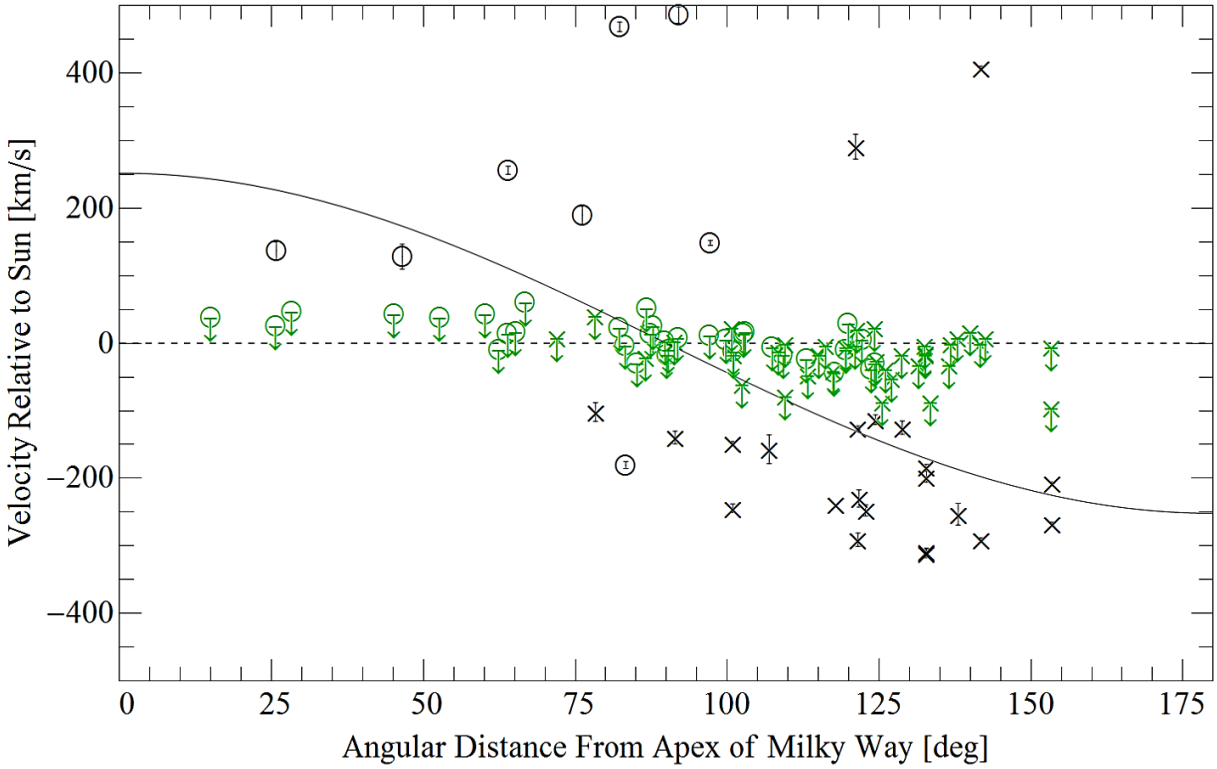

Figure 5.3: Heliocentric velocities of the OVI absorption lines are plotted as a function of the angular distance of the target from the apex of the Milky Way centre's motion with respect to the Sun. The expected sinusoidal curve for absorbers at rest with respect to the Milky Way centre is plotted for comparison. Lines from positive Sheet latitudes are indicated by crosses and lines from negative Sheet latitudes are indicated by circles. Lines at latitudes within 30^o of the Sheet plane that are likely to be associated with the LSR are coloured green and marked as upper limits. Error bars derived from the fits are shown for all points.

The sinusoidal curve predicted to be imposed by the motion of the Milky Way centre with respect to the Sun was subtracted from the OVI line velocities so as to centre the absorption lines associated with the Milky Way about zero velocity. The resultant velocities are plotted versus the apex angle in Figure 5.4.

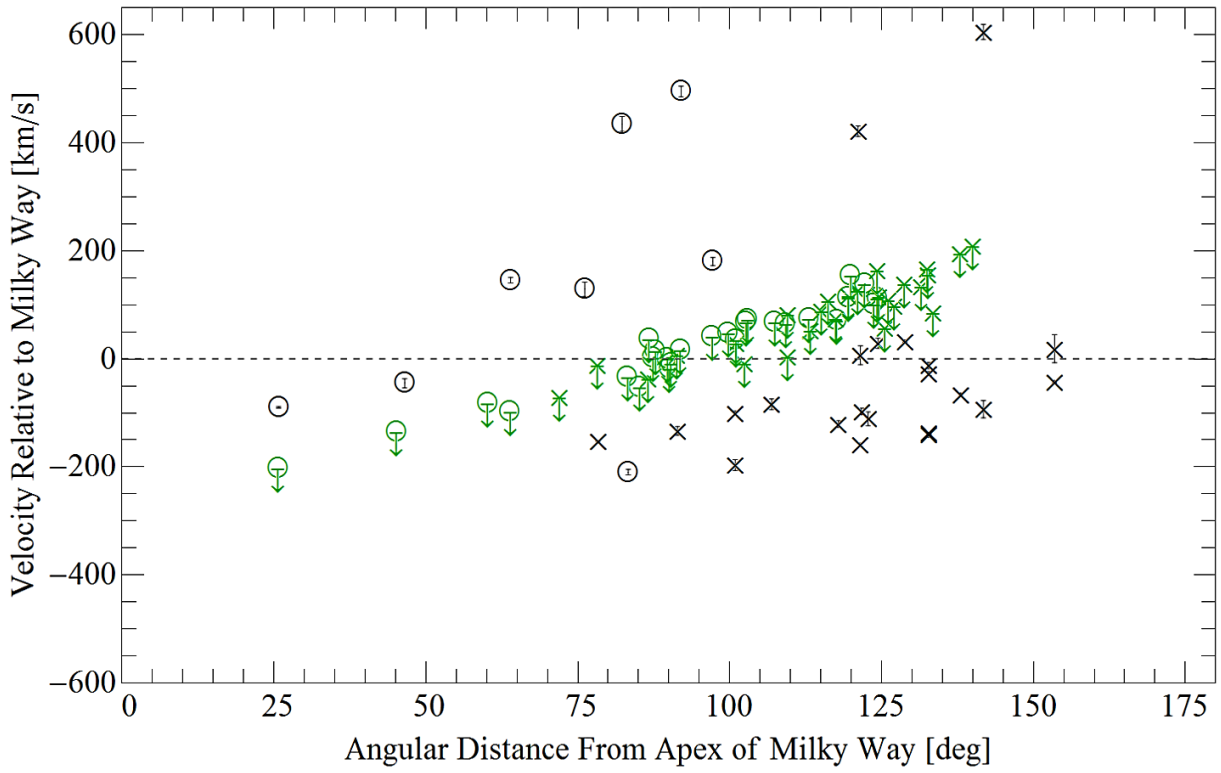

Figure 5.4: Velocities of OVI absorption lines are plotted as a function of the angular distance of the target from the apex of the Milky Way centre's motion with respect to the Sun after the relative motion of the Milky Way centre is subtracted. Lines from positive Sheet latitudes are indicated by crosses and lines from negative Sheet latitudes are indicated by circles. Lines at latitudes within 30° of the Sheet plane that are likely to be associated with the LSR are coloured green and marked as upper limits. Error bars derived from the fits are shown for all points.

At positive latitudes, the majority of the lines displayed in Figure 5.4 have negative velocities. Considering also the relatively low magnitudes of the velocities, the lines probably originate from Milky Way gas which is infalling, rather than the WHIM. Thus, they probably trace a subset of high-velocity clouds (HVC's). Further insight into the origin of these lines can be gained by examining the locations of the targets on the sky (Figure 5.5).

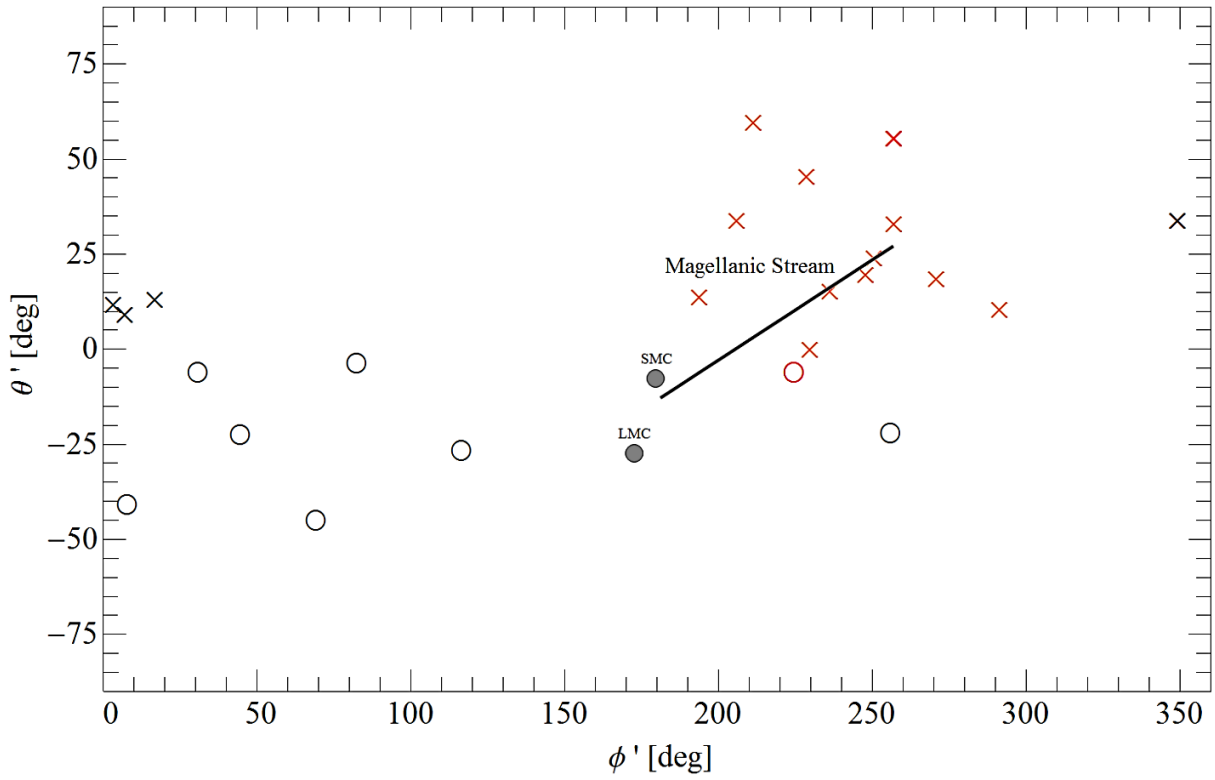

Figure 5.5: The heliocentric Sheet coordinate positions of the remaining OVI line sample are plotted. OVI lines that are associated with the Magellanic Stream and were ultimately removed from the sample are coloured red. The positions of the SMC and LMC, as well as a line connecting the head and tail of the Magellanic Stream are also plotted.

There is a clumping of OVI lines within Sheet longitude and latitude ranges of 190°-300° and 0°-70°, respectively. Given their proximity to the Magellanic Clouds, we reason that the clump is likely tracing hot gas located in the Magellanic Stream.

The Magellanic Stream is a long filament of gas trailing the Large Magellanic Cloud (LMC) and the Small Magellanic Cloud (SMC) that extends across the sky. The Stream is likely the result of tidal interactions between the Magellanic Clouds and the Milky Way. The core of the stream is marked by the black line in Figure 5.5. The Stream has a positive velocity component known as the "head" that is located at the end of the line closest to the SMC, as well as a negative velocity component known as the "tail", which is located at the other end of the line. The velocity of the head relative to the LSR is 210 km/s, while the velocity of the tail with respect

to the LSR is -370 km/s (Putman et al. 2002). Looking at Figure 5.2, it can be seen that the vast majority (13 out of 18) of the positive-latitude, negative-velocity lines are in the velocity range of the tail. Since the positions of these lines in the sky are also close to the tail, it is concluded that they must be OVI absorption from the Magellanic Stream. Thus, 14 lines were removed from the sample, leaving a total of 5 positive-latitude and 7 negative-latitude detections, the spectra of which can be seen in Figure 5.6.

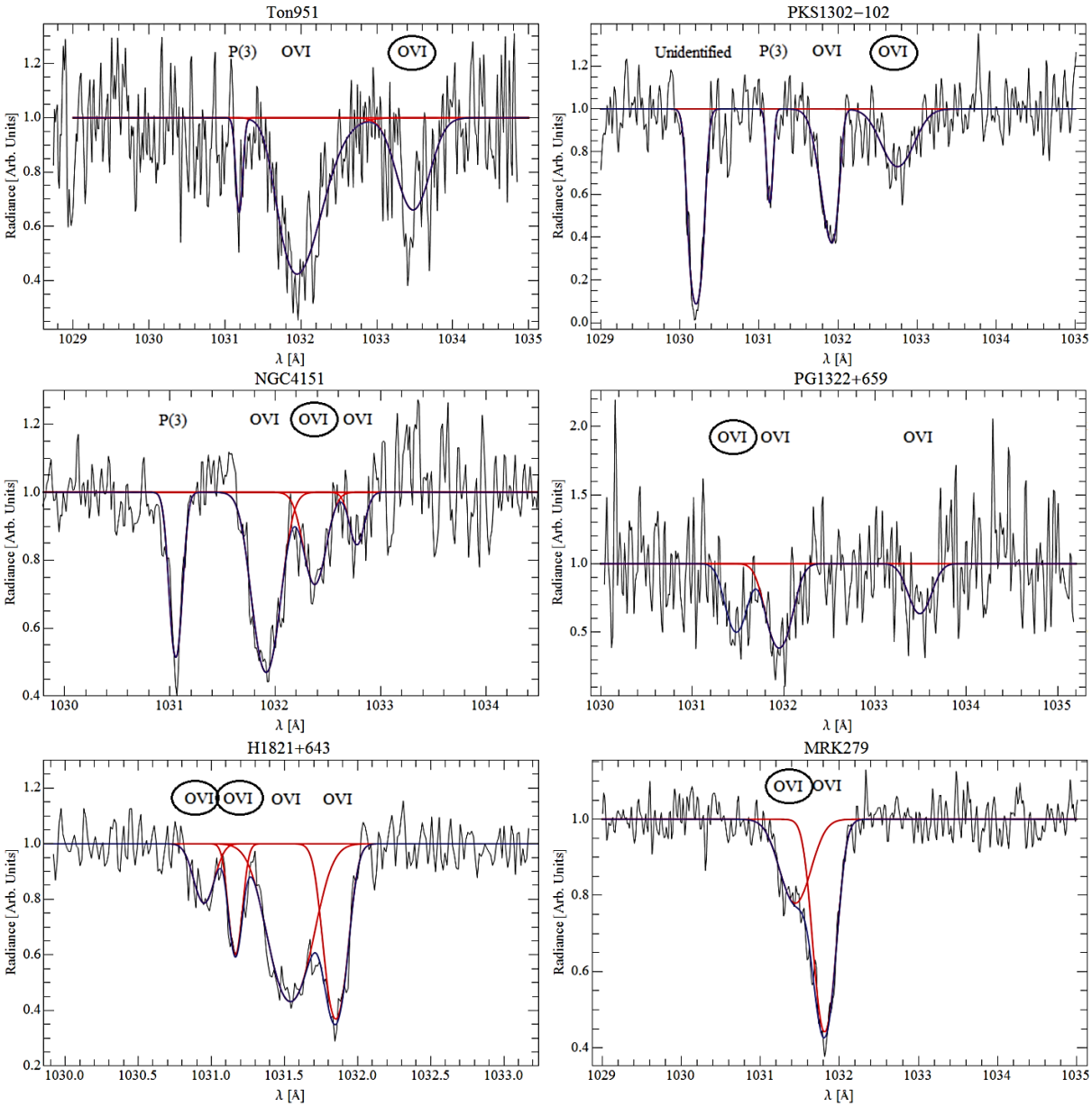

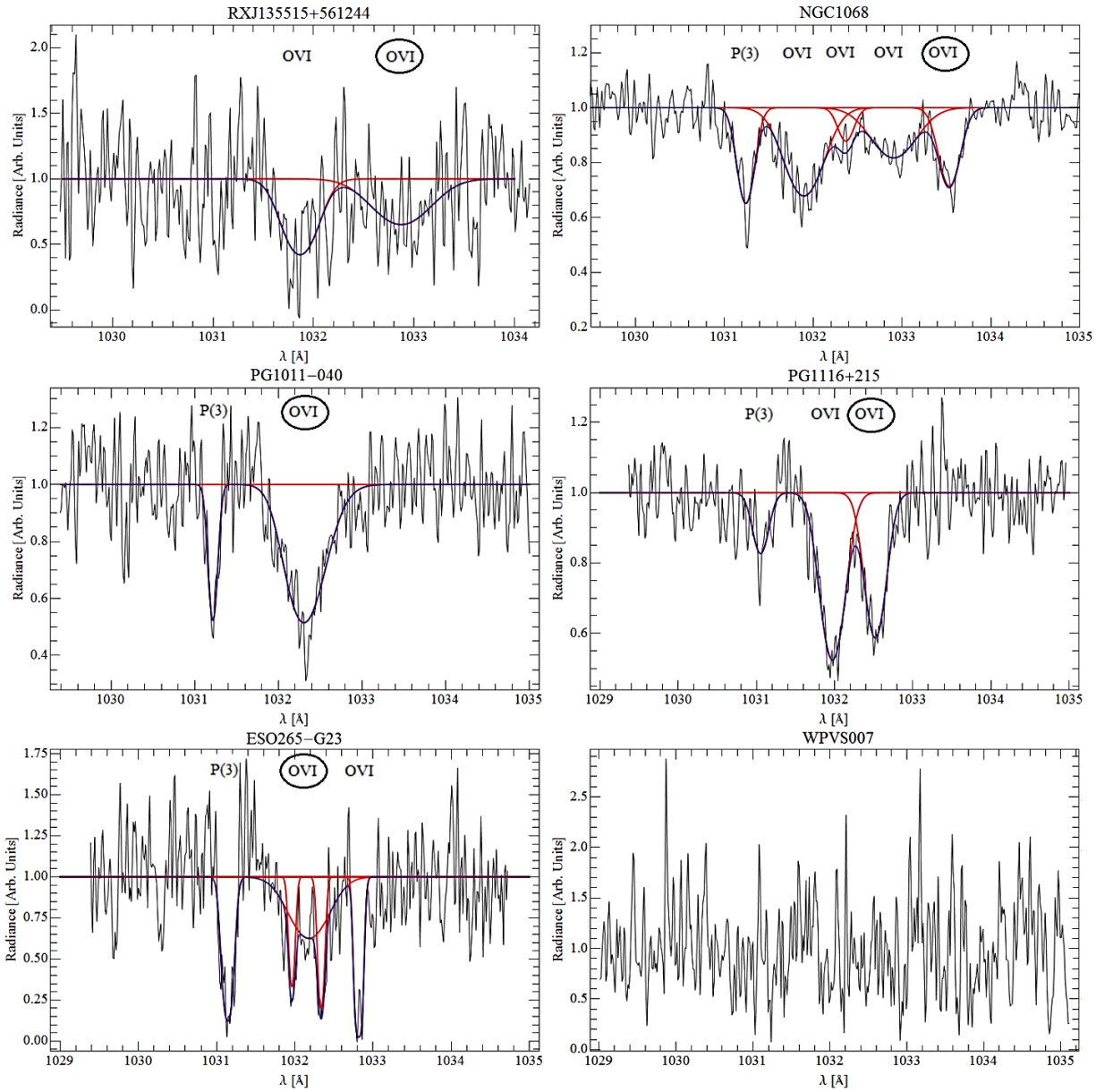

Figure 5.6: Final sample of 11 spectra with fits to their spectral features. For each spectrum, individual line profiles are in red, and the overall fit is displayed as a solid blue curve. The 12 OVI lines comprising the final sample are indicated by the circles around their respective labels. The wavelengths displayed in these spectra are those seen in the heliocentric reference frame, without the removal of the relative motions of the Sun through space.

To place all OVI line velocities in a frame of reference close to being at rest with respect to the Local Sheet, the motion of the centre of mass of the Local Group with respect to the Milky Way centre was subtracted from the line velocities in the frame of the Milky Way centre. The

apex of the Local Group with respect to the Milky Way centre has a magnitude of 47.2 km/s and is located at a latitude of -3.35º and longitude of 11.08º (McCall 2015, personal communication). Figure 5.7 plots the OVI line velocities before and after the Local Group motion was subtracted.

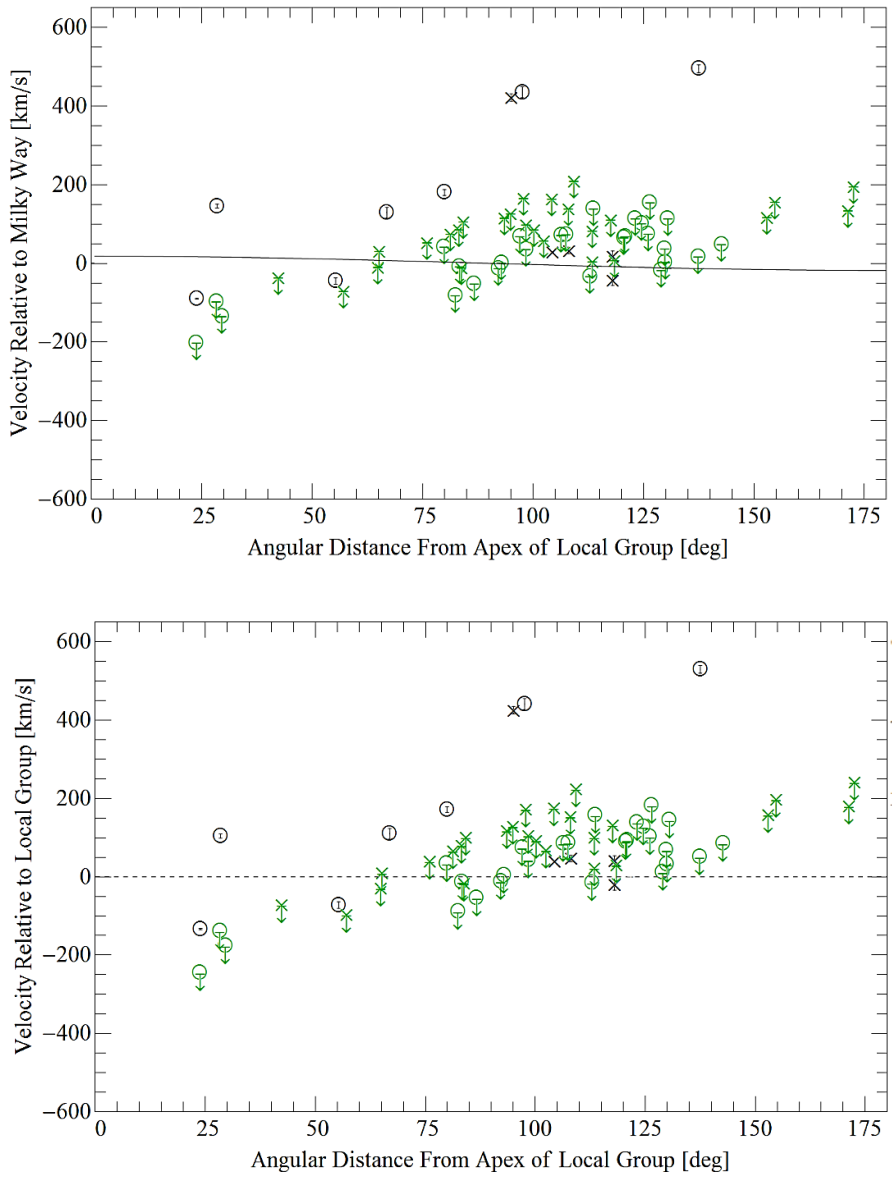

Figure 5.7: Velocities of the OVI absorption lines are plotted as a function of the angular distance of the target from the apex of the Local Group's motion with respect to the Milky Way centre before (top) and after (bottom) the relative motion of the Local Group is subtracted. The sinusoidal motion of the Local Group with respect to the Milky Way centre is also plotted in the top plot. Lines from positive Sheet latitudes are indicated by crosses and lines from negative Sheet latitudes are indicated by circles. Lines at latitudes within 30º of the Sheet plane that are likely to be associated with the LSR are coloured green and marked as upper limits. Error bars derived from the fits are shown for all points.

The motion of the Milky Way centre with respect to the centre of mass of the Local Group is relatively small (see Figure 5.4), so it is difficult to say for sure whether any of the lines near zero velocity are associated with the Local Group or beyond. Thus, these lines are retained for the analysis to follow.

Having identified and removed lines unlikely to be from the WHIM, the theoretical predictions of Chapter 2 can now be tested. In Section 2.2, it was predicted that the Hubble flow would not only broaden the absorption lines of the WHIM, but it would also redshift their minima, the effect being greatest at low Sheet latitudes. Therefore, for WHIM lines, there should be an increasing trend in velocity with $\csc(\theta')$. Such a trend could be used as a means to differentiate between the Local Group and the WHIM. The OVI line velocities are plotted in Figure 5.8 as a function of $\csc(\theta')$.

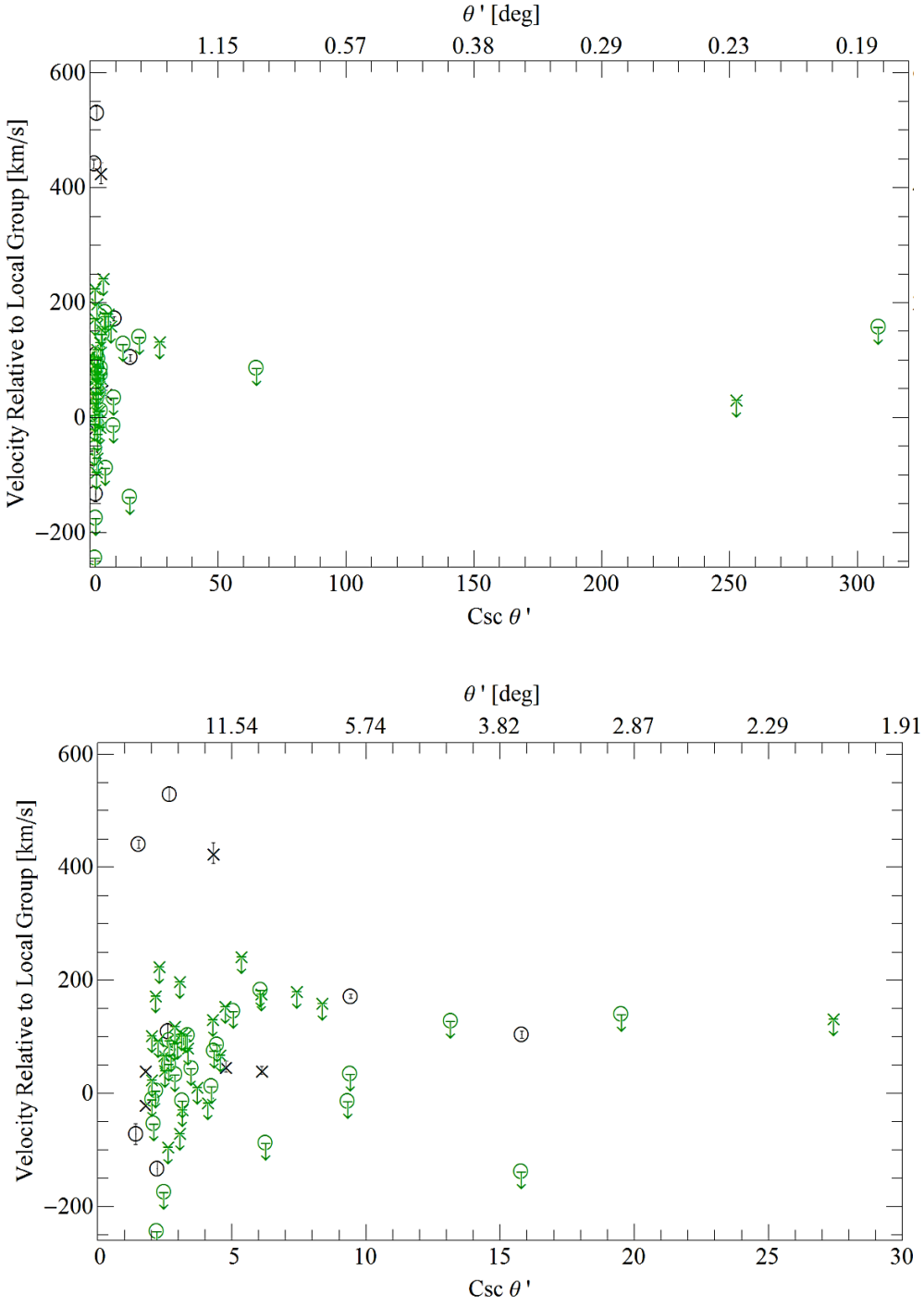

Figure 5.8: Velocity of OVI absorption lines as a function of the cosecant of the absolute value of the Sheet latitude of the target. The top plot shows the entire sample remaining, while the bottom plot shows the behaviour of the OVI lines at low csc(θ′). Lines from positive Sheet latitudes are indicated by crosses and lines from negative Sheet latitudes are indicated by circles. Lines at latitudes within 30° of the Sheet plane that are likely to be associated with the LSR are coloured green and marked as upper limits. Error bars derived from the fits are shown for all points.

There is no clear trend in velocity with csc(θ') to be seen in the data. This suggests that a large portion of the OVI lines being measured are not associated with the WHIM.

Also of interest are the predicted asymmetries in the OVI line properties with latitude due to the offset of the Sun from the plane of the Local Sheet. Most important, it should be possible to detect O^{5+} gas associated with the WHIM at negative Sheet latitudes, but not at positive latitudes. Of the remaining 14 OVI detections, 8 of them are from targets at negative Sheet latitudes, with the other 6 coming from positive Sheet latitudes. While the number of observations at positive latitudes is smaller than at negative ones, it is still in disagreement with the prediction that no WHIM OVI lines should be detectable at positive latitudes. Therefore, either the features at positive latitudes must be from the Milky Way, or the plane of the WHIM is located closer to the Sun than expected.

Line widths and shapes offer means of testing if the plane of the Local Sheet WHIM is positioned correctly, i.e., offset from the Sun. If the plane of the WHIM is offset from the Sun by the amount expected, then WHIM lines (only observable along negative Sheet latitudes) would be broadened, but not skewed by the Hubble flow. If, on the other hand, the plane of the WHIM were significantly closer to the Sun then is assumed, WHIM OVI lines would be detectable at both positive and negative latitudes. The Hubble flow would cause the lines to be both broadened and skewed. The size of the skew would be dependent on the offset of the Sun from the plane, being largest for an offset of zero. Average values for the full width at half minimum, the skew parameter, and the percentage of the lines with a non-zero skew are given in Table 5.2.

Table 5.2: Average values for key fit parameters defined separately for positive and negative heliocentric Sheet latitudes after removal of lines likely to be associated with the LSR.

Parameter	Lines from Positive Sheet Latitudes	Lines from Negative Sheet Latitudes
Full Width at Half Minimum (Å)	0.32 ± 0.06	0.36 ± 0.05
Skew Parameter (Dimensionless)	0	0.18 ± 0.10
Percentage of Lines with a Non-Zero Skew	0%	14.3%

There is no apparent asymmetry in the FWHM, suggesting that either there are no WHIM OVI line detections (and that all of the OVI lines are associated with the Milky Way) or the plane of the WHIM is closer to the Sun than expected. The lack of asymmetry was confirmed using a two-sample t-test, which compares the means, $\mu_1$and μ_2, of two samples, determining whether there is any statistically significant difference between the two. Given two sample means with standard deviations s_1 and s_2 and sample sizes n_1 and n_2, the two-sample t-test is given by

$$t = \frac{|\mu_1 - \mu_2|}{\sqrt{\frac{s_1^2}{n_1} + \frac{s_2^2}{n_2}}} \qquad [5.1]$$

Solving equation 5.1, t was found to have a value of 1.205. The number of degrees of freedom for the problem is given by the smaller of n_1-1 and n_2-1, which has a value of 4 in this case. Choosing a statistical significance of 0.05 and referring to a table of values for a two-sample t-test, a p-value of 2.132 was found to correspond to the number of degrees of freedom for the problem. This value is larger than t and therefore it can be said with statistical certainty that the two FWHM means do not differ from one another.

The presence of skew in the OVI lines would further support having the Sun closer to the plane of the WHIM, since it would not be observed otherwise, however there is only one line in the sample which has a non-zero skew (target PG1011-040). PG1011-040 is at a relatively high

latitude of -44.89° and its single OVI absorption feature has a relatively large equivalent width (0.29 Å ± 0.012 Å), suggesting that the OVI line is likely not WHIM in nature since the equivalent width is predicted to be very low at such high latitudes (see Figure 2.16). Thus it is considered an outlier and there appears to be no skew for either positive or negative latitude lines. The lack of skew would suggest that the Sun is not close to the plane of the WHIM, contradicting the conclusions made from the FWHM data. The only explanation for the observed symmetry in the FWHM data for positive and negative latitudes, along with the lack of skew is that the observed OVI lines are all from the Milky Way and that there is no WHIM O^{5+} gas observed. It is possible, however, that the skew in the OVI lines may be hidden by the noise of the spectrum, or that the contamination removal process may have affected the shape of the OVI lines, meaning that the presence of skew may have been missed. This leaves the possibility that, if the Sun is near to the plane of the WHIM, there may be some WHIM OVI lines in the sample for which the skews could not be measured. Similarly, it is possible that the similarity in FWHM values for positive and negative latitude observations is due to an overabundance of Milky Way absorption present in the detections, hiding the asymmetry in absorption lines that is expected if the Sun is offset from the plane of the Local Sheet WHIM. Therefore, at this point, it cannot be determined with absolute certainty whether the Sun lies in the plane of the Local Sheet WHIM or not and as such, both positive and negative latitude detections will be considered equally in what follows.

The most significant prediction from Chapter 2 is that the observed equivalent widths of the OVI lines should increase with the cosecant of the Sheet latitude. Using the final data set of 12 OVI absorption detections, 17 upper limits, and 53 upper limits from detections likely associated with the LSR, the equivalent width versus the cosecant of the absolute value of the Sheet latitude was plotted in Figure 5.9.

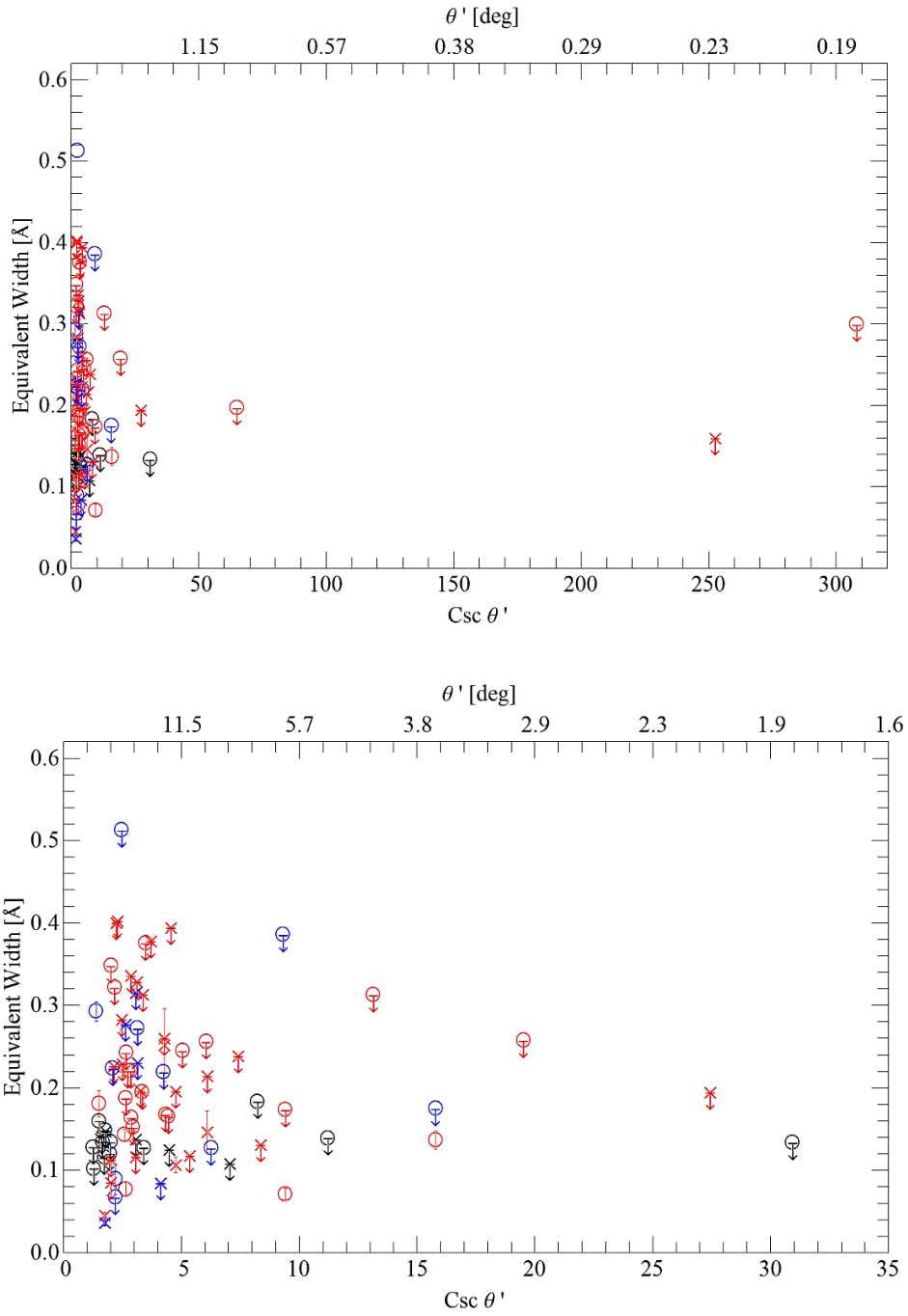

Figure 5.9: A plot of the equivalent width versus the cosecant of the absolute value of the Sheet latitude. The top plot shows all of the OVI lines, while the bottom plot shows the behaviour of the OVI lines at low csc(θ′). Lines from positive Sheet latitudes are indicated by crosses and lines from negative Sheet latitudes are indicated by circles. Line with positive and negative velocities are coloured red and blue respectively. Upper limits for spectra where no line is detected are coloured black, and upper limits designating a likely LSR associated detection are coloured according to the velocity of the detected feature. Error bars derived from the fits are shown for all points.

The OVI lines in Figure 5.9 are very scattered, with few real detections at high latitudes to be used to constrain the equivalent width to the cosecant of the absolute value of the heliocentric Sheet latitude relation. Nevertheless, it is possible to use the data to derive a meaningful upper limit to either the oxygen abundance or the hydrogen number density of the WHIM by comparing it with the theoretical trends from Chapter 2.

5.2 Constraining the Oxygen Abundance / Hydrogen Number Density of the WHIM

Observations do not clearly define whether the Sun lies in the plane of the Local Sheet WHIM or not. Thus, the relationship between the equivalent width and the cosecant of the absolute value of the Sheet latitude that was derived in Chapter 2 for both scenarios were considered equally. Recall that relationships for an 11 Mpc sheet and a 14 Mpc sheet were derived. Ideally, it should be possible to scale either relationship to fit the observational data and thereby constrain either the oxygen abundance (n_O/n_H) or the hydrogen number density (n_H) in the WHIM if needed.

Unfortunately, the observations show no clear correlation, but are instead very scattered. This is likely due to a large amount of contamination by absorption associated with the Milky Way. Nevertheless, the lines from the lowest Sheet latitudes can be utilized to define an upper boundary to any possible trend, since they are expected to have the greatest equivalent widths among the observed lines.

The observational data and the theoretically predicted trends are plotted in Figure 5.10. The spectra encompassing the two detections, along with the 6 upper limits from detections likely associated with the LSR and a single upper limit without an OVI line detection which define the upper boundary, are given in Figure 5.11.

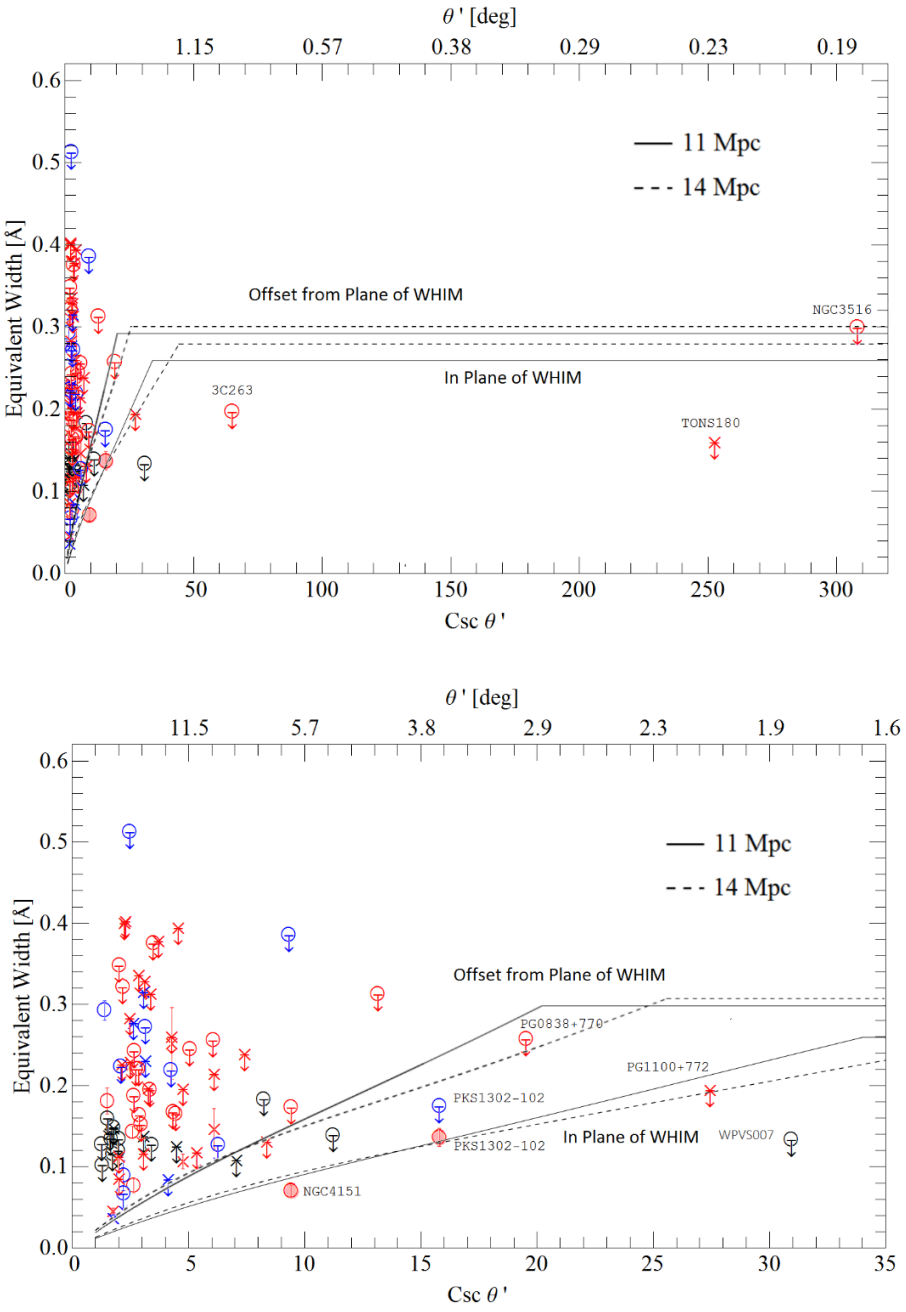

Figure 5.10: Plot of equivalent width versus the cosecant of the absolute value of the Sheet latitude. Also plotted are the theoretical relations for 11 and 14 Mpc sheets for the cases when the Sun is offset from the plane of the WHIM and when it is in the plane. The top plot shows all of the OVI lines, while the bottom plot shows the behaviour of the OVI lines at low csc(θ′). Lines from positive Sheet latitudes are indicated by crosses and lines from negative Sheet latitudes are indicated by circles. Lines with positive and negative velocities are coloured red and blue, respectively. Upper limits for spectra where no line is detected are coloured black, and upper limits designating a likely LSR detection are coloured according to the velocity of the feature. The two absorption lines that define the upper boundary to the observable trend are shaded. Error bars derived from the fits are shown for all points. The names are given for the 9 lines that define the upper bound.

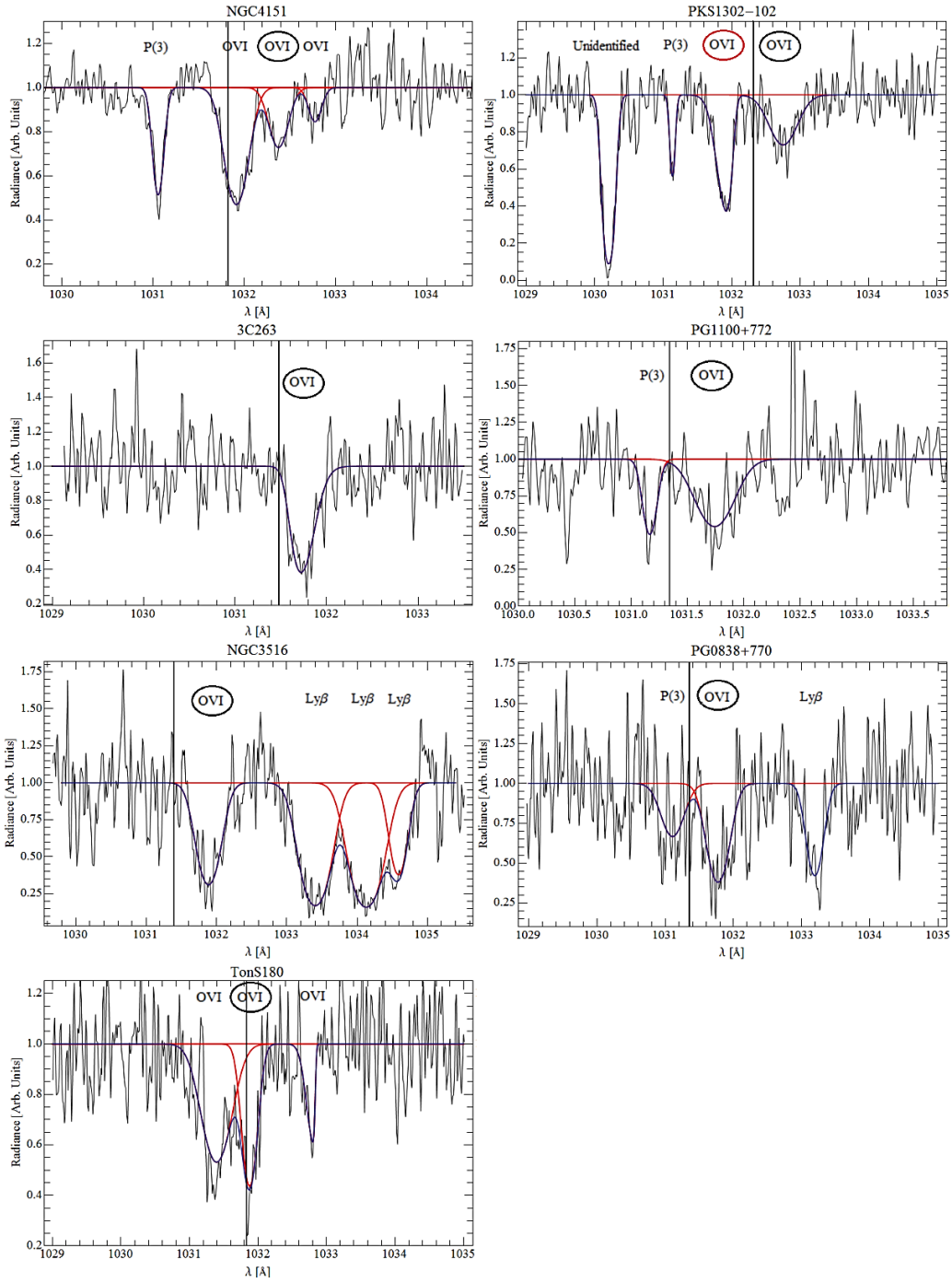

Figure 5.11: Spectra of two lowest latitude OVI line detections and 6 upper limits from detections likely associated with the LSR defining the upper boundary. For each spectrum, individual line profiles are in red, and the overall fit is displayed as a solid blue curve. The OVI line features of importance are indicated by the circles around their respective labels. The upper limit line in PKS1302-102 is circled in red. The wavelengths displayed in these spectra are those seen in the heliocentric reference frame, without the removal of the relative motions of the Sun through space. The wavelength corresponding to zero velocity after the removal of the relative motions of the Sun is marked by a vertical line.

For clarity, Figure 5.12 plots detected lines only.

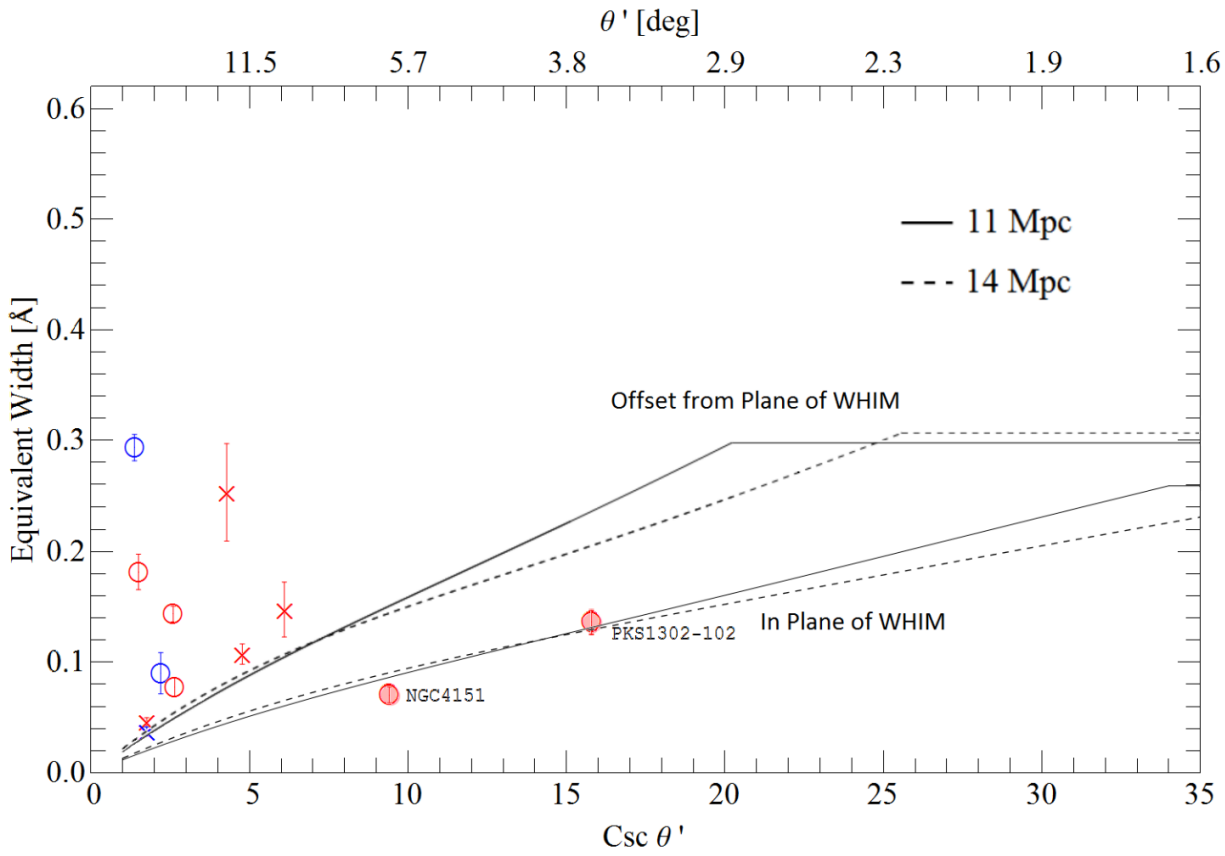

Figure 5.12: Plot of equivalent width versus the cosecant of the absolute value of the Sheet latitude. Also plotted are the theoretical relations for 11 and 14 Mpc sheets for the cases when the Sun is offset from the plane of the WHIM and when it is in the plane. Lines from positive Sheet latitudes are indicated by crosses and lines from negative Sheet latitudes are indicated by circles. Lines with positive and negative velocities are coloured red and blue, respectively. The two absorption lines that define the upper boundary are shaded for reference. Error bars derived from the fits are shown for all points. The names are given for the 2 detected lines that define the upper bound.

Since the theoretical profiles could only be calculated for $\theta > \theta_{min}$, it is unclear as to what the theoretical relation should look like at lower latitudes. It was assumed that there would be very little difference between the amount of absorption that occurred at θ_{min} when compared to that at lower latitudes, since it is expected that the gas would taper off quickly. For this reason, equivalent widths for latitudes less then θ_{min} were held at a constant value equal to the equivalent width at θ_{min}. This did not affect the fit, since the OVI lines were at latitudes greater

then θ_{min}, however it does give a better representation of the equivalent widths expected for upper limits at very low latitudes.

Figures 5.10 and 5.12 show that the theoretical trends for the case when the Sun is in the plane of the Local Sheet WHIM agree very well with the two detections observed at the lowest latitude (NGC4151 and PKS1302-102), as well as the PG1100+772 LSR associated upper limit. Due to the lack of detections at low latitudes and the fact that the 11 Mpc and 14 Mpc theoretical trends do not differ greatly, it is difficult to determine which one of the trends better fits the data. The fact that the trends fit the low latitude observations so well would suggest that not only were the original assumptions about the metallicity of the WHIM correct, but that the detected abundance of warm-hot matter in the Local Sheet is in agreement with the hydrodynamical simulations of Davé et al. (2001) and Klar and Mücket (2010). Thus, all of the warm-hot phase baryons associated with the Local Sheet are accounted for and there is no missing baryon problem in this context. This is, of course, only true if the Sun is indeed in the plane of the Local Sheet WHIM

If the Sun is in fact offset from the plane of the WHIM (as was originally predicted), then the theoretical trends for negative latitude observations have much steeper slopes. These trends do not agree well with the data, suggesting that there is an overestimation in the abundance of O^{5+} ions in the Local Sheet. If the ionization balance is correct, then either the oxygen abundance is lower than expected, or the hydrogen number density is lower than expected, or both. If the hydrogen number density is held at its theoretically-predicted value, then the oxygen abundance required to match the observational limit is 0.5 ± 0.1 times that assumed (0.1 $Z_{\odot}$). This means that the metallicity of the WHIM is at most 0.05 ± 0.01 $Z_{\odot}$. If instead the assumed metallicity of 0.1 $Z_{\odot}$ is adopted, then the hydrogen number density can be at most 0.64 ± 0.02 times that predicted.

It is apparent that whether or not the observations agree with the theoretically predicted trends depends entirely on the position of the Sun relative to the plane of the Local Sheet WHIM. Now that we have identified the two detections which define our upper boundary, we can examine their absorption line shapes in an attempt to further our understanding of the relative position of the Sun with respect to the plane of the Local Sheet WHIM. The theoretical line shape profiles for the NGC4151, PKS1302-102, and PG1100+772 lines were calculated using the method described in Chapter 2.2 for both the case in which the Sun is offset from the plane of the Local Sheet WHIM and the case when it is not. The resulting line profiles are plotted in Figure 5.13.

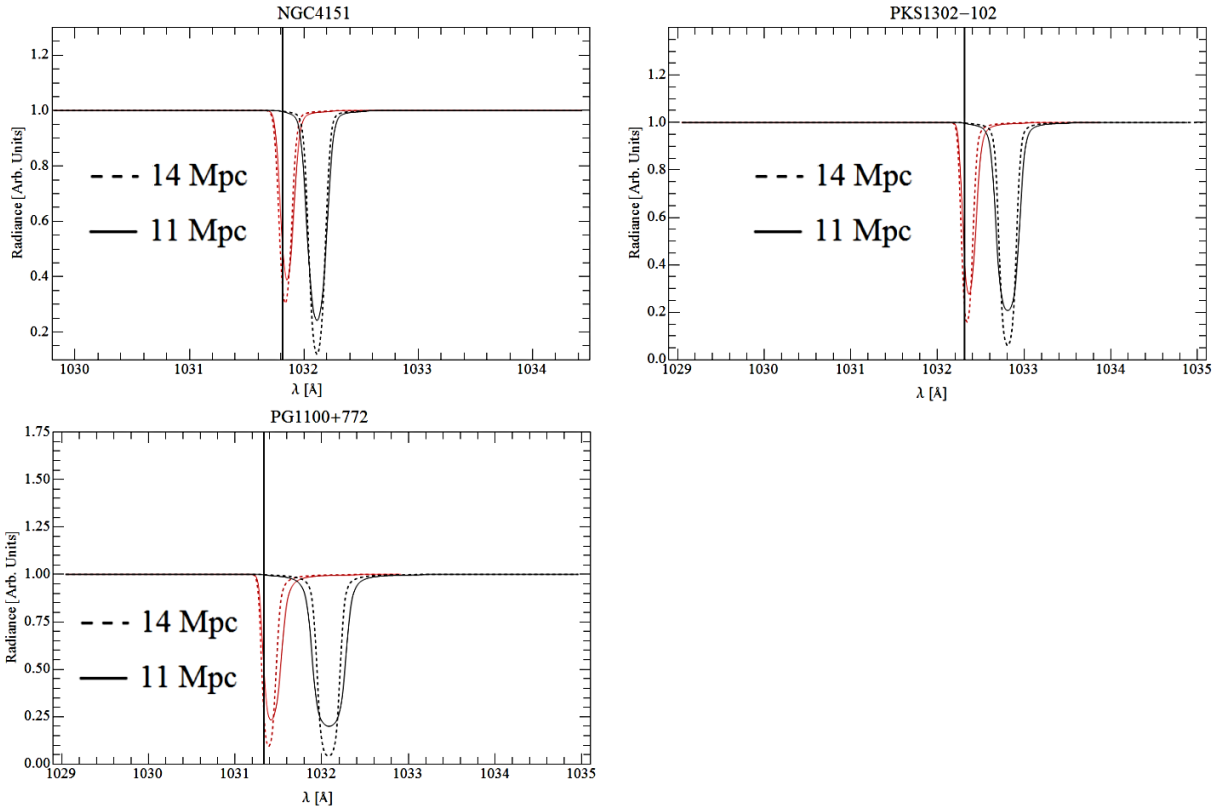

Figure 5.13: Theoretical line shape profiles are plotted for key targets constraining the oxygen abundance / hydrogen number density of the Local Sheet WHIM. The red lines represent observations where the Sun is located in the plane of the Local Sheet WHIM and the black lines represent observations where the Sun is offset from the plane of the Local Sheet WHIM. The wavelength corresponding to zero velocity after the removal of the relative motions of the Sun is marked by a vertical line.

By comparing Figure 5.13 to Figure 5.11, it can be seen that the theoretical line shape profiles derived from the case when the Sun is offset from the plane of the Local Sheet WHIM agree much better with the NGC4151 and PKS1302-102 detections then the case when the Sun is in the plane of the Local Sheet WHIM. Not only do the observations not show any skew, but they are also redshifted by an amount that is comparable to the theoretically predicted redshifts. Since PG1100+772 is at a positive latitude, it would only be observable in the case when the Sun is in the plane of the Local Sheet WHIM. This means that the only line shape that could fit the observed line would be the skewed line shape near a velocity of zero. The observed line does not have a skew, nor does it have a velocity very close to zero. This suggests that the OVI detection for this target is likely to be non-WHIM, possibly associate with the Milky Way. The fact that the theoretical lines for the case when the Sun is offset from the plane of the Local Sheet WHIM agree with observations for NGC4151 and PKS1302-102 (which are both at negative latitudes) and the lack of WHIM OVI absorption observed in PG1100+772 (which is at a positive latitude) would suggest that the Sun is indeed offset from the plane of the Local Sheet WHIM as was originally surmised. Thus, it is likely that either the oxygen abundance or hydrogen number density of the Local Sheet WHIM is lower than originally thought.

Chapter 6

Conclusions

6.1 Summary of Work

A search for the WHIM associated with the Local Sheet, has been conducted using spectral data for background sources (mostly AGNs) from FUSE. The goal was to corroborate the predicted structure and abundance of the WHIM predicted by the hydrodynamical simulations of Klar and Mücket (2010). The 1031.926 OVI absorption line was used to trace warm-hot gas at the temperatures predicted by the simulations.

FUSE spectra pre-processed using CalFUSE version 3.2.3 were analysed. Several sources of contamination were identified during the process, including two interstellar H_2 lines, absorption from intervening galaxies, and redshifted absorption from the targets themselves. After removal of the contamination, 100 OVI detections remained for which equivalent widths could be determined. For an additional 17 targets, upper limits to OVI equivalent widths were determined. The OVI absorption profiles were fit using a skew normal distribution when possible so as to

identify any skew from the asymmetric effects of Hubble broadening introduced by our position in the Local Sheet.

Upon analysing the velocities of the lines with respect to the LSR, it was found that many of the detections could be attributed to the hot-interstellar medium near to the Sun. The lines at Sheet latitudes greater than 30^{o} were removed from the sample, but 53 lines observed at lower latitudes were retained to express upper limits for WHIM absorption in those directions. A total of 30 lines not associated with the LSR were detected, 22 at positive latitudes and 8 at negative latitudes. After plotting the heliocentric Sheet coordinates of the positive-latitude lines, along with the LMC, SMC, and the Magellanic Stream, it was concluded that a large portion of the absorption features at these latitudes were actually associated with the segment of the Magellanic stream with $v_{LSR}<0$. These lines were removed from the sample, leaving 5 lines at positive latitudes and 7 at negative latitudes.

Hydrodynamical simulations of 11 and 14 Mpc sheets (indicative of the range of possible diameters for the Local Sheet) predict that OVI absorption line strengths should display an asymmetry in latitude, being much weaker in targets north of the Sheet. This asymmetry is brought upon by the offset of the Sun from the plane of the Local Sheet (as defined by its giants), by 128kpc. The asymmetry could reveal itself in either the shape of the OVI absorption lines (standard deviations or skews) or in the velocity of the lines. Examining the 7 observations at negative latitudes and the 5 observations at positive latitudes, it was concluded that there was no evidence for the existence of any asymmetry in the FWHM. Of the 12 OVI lines, only one was observed to have a non-zero skew, making it difficult to conclude whether the Sun is offset from the plane of the Local Sheet WHIM or not. It was concluded that the OVI absorption-line data were either heavily contaminated by gas in the immediate vicinity of the Milky Way, or that the plane of the WHIM was closer to the Sun than expected, or possibly both.

Hydrodynamical simulations also predict that the equivalent widths of the OVI absorption lines should vary with the cosecant of the absolute value of the Sheet latitude, having large equivalent widths at low latitudes. The observational data did not provide any clear evidence for such a relation at high latitudes, but was instead very scattered. The low-latitude observations, which were expected to traverse the greatest path through the WHIM, could be used to place constraints on either the oxygen abundance or the hydrogen number density in any WHIM associated with the Local Sheet. It was found that the theoretical equivalent width relation for the case when the Sun is in the plane of the Local Group WHIM agreed very well with observations at low latitudes, suggesting that the assumed metallicity and warm-hot baryon abundance were as predicted, and that there are no missing baryons in the Local Sheet WHIM.

In the case where the Sun is offset from the plane of the Local Group WHIM, the theoretical equivalent width relation with respect to the cosecant of the absolute vale of the Sheet latitude overestimates the O^{5+} abundance. If this is the case, then an upper limit to either the metallicity or the hydrogen number density could be defined from the observations. Assuming that simulations correctly predict the density of the WHIM, the upper limit derived for the metallicity of the WHIM was 0.05 ± 0.1 $Z_{\odot}$, i.e., 0.5 ± 0.1 times that of the generally assumed value of 0.1 $Z_{\odot}$. If instead it is assumed that the oxygen abundance is 0.1 $Z_{\odot}$, then the upper limit derived for the hydrogen number density was 0.64 ± 0.02 times that predicted for the 11 Mpc Sheet.

In order to determine which of these two scenarios best represents the Sun's actual position with respect to the Local Sheet WHIM, theoretical line shape profiles were constructed for three targets which follow the theoretical trend in equivalent width for the case when the Sun is in the plane of the Local Sheet WHIM. Upon examination, it was found that the theoretical line shape profiles for the case when the Sun is offset from the plane of the Local Sheet WHIM agreed well with observations for the two targets at negative latitudes. However, for the positive latitude

target it was found that the theoretical line shape profile did not fit the data well at all. From this, it was concluded that the Sun is likely offset from the plane of the Local Sheet WHIM and either the oxygen abundance or the hydrogen number density are less than predicted for the Local Sheet WHIM.

Assuming that the hydrogen number density is indeed that expected from the hydrodynamical simulations, then the limit on the oxygen abundance provides a significant constraint on the enrichment of the WHIM. Such information can help to identify the origin of the metals associated with the WHIM. If, however, the hydrogen number density is incorrect, the constraints would suggest 3/5 as many baryons present in the WHIM than expected, further compounding the missing baryon problem.

6.2 Future Endeavours

The original goal of this work was to directly identify WHIM associated with the Local Sheet through the unique signature brought upon by its thin, pancake-like structure. Unfortunately, it was not possible to observe the predicted relationship between the equivalent width and Sheet latitude using the FUSE data, and thus the WHIM associated with the Local Sheet was not definitively observed. It is believed that the inability to observe the predicted relationship stemmed from both the large amount of contamination from the gas associated with the Milky Way, combined with an oxygen abundance for the WHIM lower than predicted.

If indeed the oxygen abundance in the WHIM is as low as the data suggest, observations of higher sensitivity will be required in order to observe the WHIM, observations that cannot be made until the next far-UV telescope is launched. There is, however, a way to deal with the Milky Way contamination. If one were to look at analogues of the Local Sheet at sufficiently high redshifts, it would be possible to avoid the Milky Way OVI absorption simply because the OVI

associated with a distant Sheet would be redshifted with respect to its rest wavelength. The only limit to making such observations is the finite number of FUSE observations that exist. Having a distant analogue that only covers a small section of the sky means that only a few FUSE observations would be available to probe the OVI content. There is one recently observed nearby analogue, however, that may be feasible to probe using FUSE data because of its relatively large extent on the sky. This Sheet is known as Arkadia, and it spans several degrees. Without the Milky Way contamination, it is proposed that observations of targets that intersect Arkadia could provide an opportunity to detect the WHIM associated with a Sheet-like structure. Additionally, Arkadia observations could help to further constrain the oxygen abundance of the WHIM. This analysis should be possible once we have a better understanding of Arkadia and its structure.

Unfortunately, the future of far-UV space telescopes that cover a spectral range including the OVI absorption doublet is rather bleak. This makes it very difficult to study the Local Sheet WHIM with any more detail in the near future. Instead, it may be more valuable to look at analogues to the Local Sheet as more continue to be identified. For analogues much larger than the Local Sheet, the shock heating would result in very high temperatures, high enough to ionize a significant fraction of O^{6+} gas. Thus, for very large analogues, x-ray observations could be used to probe their structure.

Bibliography

P. A. R. Ade, N. Aghanim, M. I.R. Alves, et al. 2013, A&A 557, A53

M. Asplund, N. Grevesse, A. J. Sauval, et al. 2009, A&A, 47, 481

D. A. Buote, L. Zappacosta, T. Fang, et al. 2009, ApJ, 659, 1351

R. Cen and J. P. Ostriker 2006, ApJ, 650, 560

C. W. Danforth and J. M. Shull 2005, ApJ, 624, 555

R. Davé, R. Chen, J. P. Ostriker, et al. 2001, ApJ, 553, 473

W. V. Dixon, D. J. Shanow, P. E. Barrett, et al. 2007, PASP, 119, 527

A. G. Doroshkevich and S. F. Shandarin 1978, SvA, 22, 653

E. M. L. Humphreys, M. J. Reid, J. M. Moran, et al. 2013, ApJ, 775, 13

I. D. Karachentsev, D. I. Makarov, E. I. Kaisina 2013, AJ, 145, 101

J. S. Klar and J. P. Mücket 2010, A&A, 522, A114

J. S. Klar and J. P. Mücket 2012, MNRAS, 423, 304

M. L. McCall, O. Vaduverscu, F. Pozo Numez, A, Barr Dominguez, et al. 2012, A&A, 540, 49

M. L. McCall 2014, MNRAS, 440, 405

H. W. Moos, W. C. Cash, L. L. Cowie, et al. 2000, ApJ, 583, 1

D. C. Morton an H. L. Dinerstein 1975, ApJ, 204, 1

National Institute of Standards and Technology, 2014, Available:
http://physics.nist.gov/PhysRefData/ASD/lines_form.html

P. Norberg, S, Colee, C. M. Baugh, C. S. Frenk, et al. 2002, MNRAS, 336, 907

P. Norberg, C. S. Frenk, S. Cole 2008, MNRAS, 383, 646

J. X. Prochaska, B. Weiner, H. W. Chen, et al. 2011, ApJ, 740, 91

M. E. Putman, V. de Heij, L. Staveley-Smith, R. Braun, et al. 2002, AJ, 123, 873

A. G. Riess, L. Macri, S. Casertano, et al. 2011, ApJ, 730, 119

A. Riess, J. Fliri, D. Valls-Gabaud 2012, ApJ, 745, 156

K. R. Sembach, B. P. Wakker, B. D. Savage, et al. 2003, ApJS, 146, 165

J. M. Shull, B. D. Smith, C. W. Danforth 2012, ApJ, 759, 23

J. B. Tatum 2011, Oscillator Strengths and Related Topics, Available: astrowww.phys.uvic.ca/~tatum/stellatm/atm9.pdf

J. Tonry and M. Davis 1979, AJ, 84.1511

T. M. Tripp, D. V. Bowen, K. R. Sembach, et al. 2004, Submitted to: ASP Conf.Ser. astro-ph/0411151

B. R. Tully, E. J. Shaya, I. D. Karachentsev, et al. 2008, ApJ, 676, 184

B. P. Wakker, B. D. Savage, K. R. Sembach, et al. 2003, ApJS, 146, 1

B. E. Wood, J. L. Linsky, G. Hébrard, et al. 2002, ApJS, 140, 91

K. Yoshikawa, S. Sasaki 2006, ASJ, 58, 641

Appendices

Appendix A

Table A.1: FUSE target names and archive data information is given for both the 90 target sample and the 13 upper limits. Targets where only an upper limit to OVI absorption could be obtained are written in bold.

Target Name	Target Type	Data Set ID	No. of Exposures	Total Exposure Time (s)
TONS180	Galaxy	D0280101000	20	9136
		P1010502000	11	15419
TONS210	QSO	P1070302000	16	39835
		P1070301000	6	13486
3C57	QSO	P2100501000	5	12079
HE0226-4110	Galaxy	D0270101000	25	24649
		D0270102000	14	39920
		D0270103000	14	17382
		P1019101000	20	64214
		P1019102000	14	14494
		P1019103000	11	18980
		P1019104000	12	18159
		P2071301000	5	11047
NGC985	Galaxy	P1010903000	32	49968
IRAS_F22456-5125	Galaxy	Z9073901000	3	5721
		Z9073902000	12	31836
PKS2155-304	QSO	P1080701000	12	19171
		P1080703000	2	64354
		P1080705000	23	38624
NGC1068	Galaxy	A1390201000	9	19547
		A1390202000	9	19989
		A1390203000	7	18083
		A1390204000	9	18348
		A1390205000	9	19080
		P1110202000	9	21951
NGC7469	Galaxy	C0900101000	5	3596
		C0900102000	5	3354
		P1018703000	23	37360
FIRSTJ215501.4-092224	QSO	P1081001000	7	15507
		P1081002000	12	24255

		P1081003000	10	21779
		P2071101000	5	10902
2MASX-J21362313-6224008	Galaxy	D9030401000	10	36912
PKS0405-12	QSO	B0870101000	28	67169
MRK335	Galaxy	P1010203000	26	45895
		P1010204000	31	53389
PKS2005-489	QSO	P1073801000	5	11097
		C1490301000	7	24694
		C1490302000	5	13422
MRK509	Galaxy	P1080601000	29	60555
		X0170101000	13	20004
		X0170102000	23	33409
IIZW136	Galaxy	P1018301000	14	22611
		P1018302000	9	11800
		P1018303000	14	8231
		P1018304000	12	22097
PKS0558-504	QSO	C1490601000	13	48333
		P1011504000	15	46202
E141-55	Galaxy	I9040104000	21	40962
QSO0045+3926	QSO	Z0020401000	5	8243
		D1310101000	30	39715
		D1310102000	21	33126
		D1310103000	8	6674
		D1310104000	26	35577
		D1310105000	16	19960
		D1310106000	16	23955
		D1310107000	15	19582
AKN120	Galaxy	P1011201000	9	8383
		P1011202000	11	20192
		P1011203000	17	25646
ESO265-G23	Galaxy	A1210404000	2	1782
		A1210405000	3	4893
		A1210406000	5	8441
		A1210407000	14	21740
		A1210408000	11	11486
		A1210409000	8	6428
HS0624+6907	QSO	P1071001000	5	13935
		P1071002000	4	17708
		S6011201000	13	38714
		S6011202000	14	39903

		U1021001000	5	15847
MS07007+6338	Galaxy	P2072701000	4	7444
		D0550501000	35	82188
		S6011501000	5	16497
		U1021402000	4	6697
		U1021403000	6	16019
		U1021404000	14	22470
VIIZW118	Galaxy	S6011301000	12	49007
		U1021501000	3	5637
		U1021502000	9	22017
		P1011604000	26	74579
		P1011605000	10	26075
		P1011606000	5	9805
H1821+643	Galaxy	P1016402000	48	62585
		P1016403000	3	12213
		P1016404000	5	17897
		P1016405000	8	23066
		C0950201000	25	103240
		C0950202000	31	92312
		U1040802000	10	22980
		U1040803000	13	38262
1H0717+714	QSO	F0260302000	10	22567
MRK79	Galaxy	P1011701000	5	3147
		P1011702000	5	11702
		P1011703000	8	12498
MRK9	Galaxy	S6011601000	6	23869
		P1071101000	6	11829
		P1071102000	5	14275
		P1071103000	9	11989
PG0804+761	Galaxy	S6011001000	16	55188
		S6011002000	11	36450
		P1011901000	19	57409
		P1011903000	5	21106
TON951	QSO	P1012002000	18	30949
MRK501	QSO	C0810101000	14	18911
		P1073301000	5	11563
MRK876	Galaxy	D0280201000	15	6993
		D0280202000	15	8992
		D0280203000	29	77858
		U1036601000	3	5533

		P1073101000	11	52683
PG1011-040	Galaxy	B0790101000	58	85358
IR1143-1810	Galaxy	P1071901000	6	7243
MRK106	Galaxy	A1210202000	3	6297
		C1490501000	29	116202
MRK279	Galaxy	C0900201000	24	41900
		S6010501000	6	17464
		S6010502000	6	19955
		P1080303000	17	62846
		P1080304000	12	30746
		D1540101000	21	91040
		F3250102000	5	1331
		F3250103000	10	2288
		F3250104000	7	3228
		F3250106000	1	3546
MRK290	Galaxy	D0760101000	7	9239
		D0760102000	13	46770
		P1072901000	5	12769
3C263	QSO	E8480701000	3	7433
		G0440201000	8	17664
		G0440202000	7	14839
		G0440203000	7	15399
		D8081701000	1	3408
		F0050101000	30	83625
		F0050102000	2	2755
		F0050103000	10	16805
		F0050104000	15	39368
		F0050105000	7	21602
PG0953+414	QSO	P1012201000	19	33788
		P1012202000	21	37904
PG1351+640	Galaxy	S6010701000	14	49524
		P1072501000	23	70134
PKS1302-102	QSO	P1080201000	16	31696
		P1080202000	17	32309
		P1080203000	34	82060
MRK817	Galaxy	P1080401000	3	12116
		P1080402000	3	12910
		P1080403000	27	73154
		P1080404000	32	86985
MRK1383	Galaxy	P2670101000	14	38707

		P1014801000	16	25040
MRK153	Galaxy	A0940102000	26	40574
		A0940101000	32	65048
IZW92	Galaxy Pair	D1180101000	73	148256
		P1080104000	36	106329
		P1080105000	35	104316
		P1080106000	36	65116
		P1080107000	39	96035
		P1080108000	13	32740
		P1080109000	17	30468
		U1031801000	4	9542
		P1080101000	12	52357
		P1080102000	21	56247
		P1080103000	32	82171
3C273	QSO	P1013501000	32	41588
MRK421	Galaxy	Z0100101000	11	26791
		Z0100102000	9	24154
		Z0100103000	5	12159
		P1012901000	8	21802
PG1116+215	QSO	P1013102000	6	10792
		P1013103000	7	8032
		P1013104000	6	10918
		P1013105000	21	33490
		P1013101000	7	11047
PG1211+143	Galaxy	P1072001000	38	52274
NGC4151	Galaxy	P1110505000	10	21520
		C0920101000	35	48935
		P2110201000	12	13631
		P2110202000	5	5968
MKN59	Galaxy	A0360202000	3	9830
MR_2251-178	Galaxy	P1111010000	20	52933
MRK1044	Galaxy	D0410101000	10	12635
PG2349-014	QSO	P1074201000	5	12470
		E5260401000	10	4316
		E5260402000	18	26442
FAIRALL9	Galaxy	P1010601000	18	34827
NGC7714	Galaxy	A0860606000	3	6025
		A0230404000	4	5796
		B0040301000	10	15839
		C0370201000	29	51926

		C0370202000	5	10119
		C0370203000	1	1960
		C0370204000	10	18691
		C0370205000	4	5964
		C0370206000	11	11034
MRK586	Galaxy	D0550102000	18	19758
		D0550102000	35	45710
FAIR1116	Galaxy	D8060601000	9	12755
MRK618	Galaxy	P1070901000	4	2691
		P1070902000	3	6293
MRK304	Galaxy	P1073901000	5	12387
MRK352	Galaxy	P1070201000	8	16644
IRAS09149-62	Galaxy	S7011002000	5	13461
		S7011003000	8	14405
		U1072201000	3	7554
		U1072202000	10	36007
		U1072203000	12	23721
		A0020503000	4	13119
MRK10	Galaxy	Z9072801000	6	23219
MRK506	Galaxy	P1073401000	8	10473
PG0838+770	Galaxy	G0200101000	3	1992
		G0200104000	12	25287
		G0200105000	10	25700
		G0200106000	9	19235
		G0200107000	9	17149
T1247-232	Galaxy	Q1050101000	10	19795
		Q1050102000	3	4425
MRK487	Galaxy	P1073001000	5	14444
PG0947+396	QSO	A0600101000	5	10902
TON28	QSO	P2073101000	6	11215
MKN142	Galaxy	D8061101000	14	20520
TON1187	Galaxy	P1071502000	5	8257
RXJ135515+561244	Galaxy	D8061601000	13	47766
PG1444+407	QSO	P1072701000	4	10090
MRK734	Galaxy	P1071702000	5	4587
MRK478	Galaxy	P1110909000	10	14183
PG1415+451	QSO	A0601111000	6	12284
PG1411+442	Galaxy	A0601010000	4	7358
NGC5548	Galaxy	D1550101000	10	22678
		D1550102000	5	7913

		P1014601000	17	25973
PG1307+085	QSO	P1072401000	9	10494
PG1402+261	Galaxy	P1072601000	6	8157
MRK54	Galaxy	A0520101000	16	27114
PHL2525	QSO	E1300101000	17	29378
HE0238-1904	QSO	D1030201000	11	15607
		D1030202000	10	10903
		D1030203000	8	4224
		D1030204000	15	17315
		D1030205000	12	13562
		D1030206000	31	50587
		P2071401000	5	10345
I_ZW_1	Galaxy	P1110101000	10	13584
		P1110102000	16	25187
PG1322+659	QSO	A0600808000	3	5516
		G0440401000	16	38079
PG1004+130	QSO	A0350101000	48	84537
PG1553+113	QSO	E5260501000	12	12561
		E5260502000	15	20526
		E5260503000	10	14277
NGC3516	Galaxy	G9170101000	8	28687
		G9170102000	6	16847
		P2110102000	9	20686
		P2110103000	6	16901
		P2110104000	9	16329
		P1110404000	12	16335
PG1100+772	QSO	P1071603000	39	72055
		S6010901000	8	29868
		U1027501000	6	13370
		U1027502000	10	17349
		U1027503000	4	2031
		P1071601000	5	11447
		P1071602000	4	9411
PG1259+593	QSO	P1080104000	36	106329
		P1080105000	35	104316
		P1080106000	36	65116
		P1080107000	39	96035
		P1080108000	13	32740
		P1080109000	17	30468
		U1031801000	4	9542

		P1080101000	12	52357
		P1080102000	21	56247
		P1080103000	32	82171
RXJ010027-511346	Galaxy	D8060301000	3	6460
WPVS007	Galaxy	D8060201000	19	48380
RXJ2241.8-4405	Galaxy	Z9070301000	7	20115
NGC1399	Galaxy	A0880304000	5	11602
		A0880303000	6	16524
Q0026+1259	QSO	Q2060101000	11	20343
EUVEJ0349-537	Galaxy	E8970301000	10	28811
SBS0335-052	Galaxy	A0360404000	9	24411
ESO31-8	Galaxy	D9110201000	6	17235
HE0450-2958	Galaxy	P2071501000	6	15995
PG0052+251	QSO	P1070101000	13	17656
IRASL06229-6434	Galaxy	D9030301000	21	45334
		D9030302000	8	21618
		D9030303000	5	10441
		D9030304000	8	8538
		U1071001000	3	9329
		U1071002000	5	15429
		U1071003000	3	5094
HE1115-1735	Galaxy	P2071801000	7	11734
PG1626+554	Galaxy	C0370101000	38	89996
		P1073201000	3	9368
1H0707-495	Galaxy	B1050101000	7	20301
		B1050102000	10	24259
		B1050103000	14	22559
		E1190101000	17	50310
TON1480	QSO	A0580101000	12	29696
IR07546+3928	Galaxy	E0870101000	37	53219
		P1071201000	10	15290
		S6011801000	20	27857
AKN564	Galaxy	B0620101000	30	60786

Table A.2: Target and OVI line information for uncontaminated OVI lines.

Target Name (1)	Target Type	Supergalactic L (deg)	Supergalactic B (deg)	Sheet L (deg)	Sheet B (deg)	Noise (σ)	Equivalent Width (Å)	Heliocentric Velocity (km/s) (2)	Skew Parameter	FWHM (Å)	J	Target Redshift (z)
TONS180	Galaxy	274.96	-6.44	229.72	0.23	0.18	0.26 ± 0.021	-139.54 ± 9.51	0	0.47 ± 0.055	<3	0.062
							0.16 ± 0.014	2.917 ± 12.38	0	0.24 ± 0.029		
IRAS_F22456-5125	Galaxy	238.94	6.04	193.87	13.98	0.25	0.089 ± 0.011	-101.75 ± 13.89	0	0.12 ± 0.021	3	0.10
							0.085 ± 0.011	40.70 ± 13.64	0	0.11 ± 0.024		
ESO265-G23	Galaxy	157.48	-27.76	116.54	-26.68	0.37	0.068 ± 0.032	26.17 ± 13.10	0	0.082 ± 0.026	3	0.057
							0.090 ± 0.019	136.64 ± 13.38	0	0.086 ± 0.023		
NGC7714	Galaxy	293.11	19.54	250.66	24.37	0.27	0.33± 0.027	-247.11 ± 8.27	0	0.60 ± 0.069	3	0.0093
PG2349-014	QSO	290.93	14.84	247.85	19.94	0.35	0.34 ± 0.044	-238.39 ± 0.39	0	0.73 ± 0.073	3	0.17
MRK1044	Galaxy	293.7408	-25.1865	246.1667	-20.14652002	0.32	0.16 ± 0.022	14.54 ± 8.44	0	0.35 ± 0.056	<3	0.016
PKS0558-504	QSO	221.26	-53.52	179.31	-46.00	0.14	0.24 ± 0.0087	46.51 ± 1.34	-1.08 ± 0.72	0.51 ± 0.094	3	0.14
MRK509	Galaxy	253.76	52.21	211.50	59.94	0.077	0.21 ± 0.0090	-229.67 ± 12.59	0	0.51 ± 0.031	4	0.034
NGC1068	Galaxy	304.26	-25.84	256.18	-21.98	0.12	0.19 ± 0.013	8.72 ± 9.83	0	0.58 ± 0.12	3	0.0038
							0.078 ± 0.0086	485.50 ± 12.18	0	0.27 ± 0.33		
PG1116+215	QSO	88.46	-15.42	44.71	-22.48	0.095	0.14 ± 0.0071	188.97 ± 13.82	0	0.30 ± 0.020	3	0.18
TONS210	QSO	274.96	-13.15	224.65	-6.15	0.13	0.051 ± 0.0077	-180.25 ± 5.15	0	0.20 ± 0.043	<3	0.12
							0.39 ± 0.013	-2.91 ± 10.94	-1.49 ± 0.57	0.58 ± 0.080		
3C57	QSO	270.29	-19.01	242.69	-13.56	0.69	0.22 ± 0.045	-17.44 ± 7.65	0	0.23 ± 0.056	3	0.67
NGC985	Galaxy	289.39	-26.23	246.53	-21.24	0.17	0.22 ± 0.011	52.33 ± 5.13	-2.72± 1.3	0.40 ± 0.059	3	0.043
PKS2155-304	QSO	258.03	26.22	205.99	34.08	0.060	0.047 ± 0.0064	-244.20 ± 6.36	0	0.29 ± 0.058	<3	0.12

							0.060 ± 0.0058	23.26 ± 3.23	-2.88 ± 0.61	0.44 ± 0.035		
							0.22 ± 0.0045	-148.27 ± 3.17	0	0.21 ± 0.030		
NGC7469	Galaxy	294.25	29.17	257.08	33.36	0.14	0.11 ± 0.023	-311.07 ± 6.37	0	0.31 ± 0.053	4	0.016
							0.10 ± 0.035	-183.15 ± 3.94	0	0.21 ± 0.031		
							0.097 ± 0.028	-17.44 ± 2.20	0	0.14 ± 0.016		
FIRSTJ215501.4-092224	QSO	238.94	38.86	228.74	45.74	0.11	0.12 ± 0.017	-290.72 ± 9.88	0	0.43 ± 0.080	4	0.19
							0.17 ± 0.013	-125.01 ± 2.61	0	0.20 ± 0.020		
							0.24 ± 0.011	20.35 ± 8.30	2.51 ± 1.21	0.42 ± 0.060		
MRK335	Galaxy	250.27	16.50	270.78	18.85	0.10	0.072 ± 0.0084	-308.16 ± 5.26	0	0.22 ± 0.038	4	0.026
							0.13 ± 0.013	-197.69 ± 8.00	0	0.41 ± 0.066		
							0.12 ± 0.0071	-14.55 ± 2.40	0	0.24 ± 0.019		
IIZW136	Galaxy	304.26	51.29	257.02	55.77	0.22	0.27 ± 0.015	-290.72± 3.12	0	0.33 ± 0.023	4	0.063
							0.25 ± 0.010	0.00 ± 8.44	2.28 ± 1.03	0.42 ± 0.060		
							0.19 ± 0.0085	407.01 ± 3.13	-3.45 ± 1.48	0.26 ± 0.031		
E141-55	Galaxy	297.97	15.43	163.53	22.14	0.18	0.28 ± 0.013	8.72 ± 2.44	0	0.33 ± 0.019	4	0.036
QSO0045+3926	QSO	270.09	11.22	291.34	10.69	0.24	0.29 ± 0.036	-252.93 ± 16.13	0	0.84 ± 0.13	3	0.13
							0.12 ± 0.019	8.72 ± 6.32	0	0.24 ± 0.049		
AKN120	Galaxy	223.99	-61.07	268.01	-59.42	0.26	0.14 ± 0.011	61.05 ± 2.63	-36.99 ± 51.26	0.31 ± 0.050	4	0.033
HS0624+6907	QSO	295.92	-5.09	338.51	-11.37	0.29	0.25 ± 0.011	-8.72 ± 3.30	-6.27 ± 3.11	0.30 ± 0.031	4	0.37
MS07007+6338	Galaxy	313.36	-10.71	341.51	-17.25	0.20	0.20 ± 0.010	-23.26 ± 13.01	1.73 ± 1.18	0.38 ± 0.087	4	0.15
H1821+643	Galaxy	219.67	41.04	349.16	34.08	0.079	0.037 ± 0.0041	-267.46 ± 2.82	0	0.16 ± 0.024	3	0.30
							0.046 ± 0.0034	-206.41 ± 1.29	0	0.10 ± 0.011	3	
							0.21 ± 0.0087	-95.94 ± 2.26	0	0.31 ± 0.019	3	
							0.13 ± 0.0056	-5.81± 1.43	0	0.16 ± 0.0098	3	
1H0717+714	QSO	253.76	-2.83	343.13	-9.47	0.25	0.26 ± 0.011	29.07± 3.43	-11.18 ± 6.78	0.42 ± 0.043	3	0.30
MRK9	Galaxy	293.09	-15.03	345.71	-21.89	0.22	0.24n± 0.018	-5.81 ± 20.80	-1.12 ± 1.18	0.39 ± 0.11	4	0.040

PG0804+761	Galaxy	221.26	2.48	345.89	-4.35	0.088	0.31 ± 0.0051	-37.79 ± 4.01	-1.47 ± 0.27	0.45 ± 0.025	4	0.10
TON951	QSO	209.98	-32.88	8.11	-40.75	0.20	0.400 ± 0.014	23.26 ± 11.61	2.01 ± 0.74	0.67 ± 0.079	3	0.064
							0.18 ± 0.016	468.06 ± 7.11	0	0.047 ± 0.055		
MRK501	QSO	334.80	54.31	22.11	46.40	0.20	0.270 ± 0.012	0.00 ± 2.22	-33.91 ± 33.52	0.48 ± 0.044	<3	0.034
MRK876	Galaxy	326.67	33.29	1.24	25.65	0.087	0.40 ± 0.0060	17.44 ± 2.28	-9.22 ± 1.96	0.69 ± 0.025	4	0.13
PG1011-040	Galaxy	157.48	-39.76	69.39	-44.89	0.19	0.29 ± 0.012	127.92 ± 18.49	1.24 ± 0.75	0.58 ± 0.10	3	0.058
IR1143-1810	Galaxy	24.217	-20.96	88.67	-23.64	0.33	0.51 ± 0.022	43.61± 9.59	4.12 ± 1.74	0.73 ± 0.079	3	0.013
MRK106	Galaxy	27.64	-12.63	0.96	-20.29	0.17	0.22 ± 0.0095	17.44 ± 1.94	-1.57 ± 0.86	0.41 ± 0.072	3	0.12
MRK279	Galaxy	27.78	19.79	3.31	12.06	0.076	0.11 ± 0.0092	-125.01 ± 9.95	0	0.44 ± 0.058	3	0.030
							0.20 ± 0.0061	-17.44 ± 2.21	0	0.30 ± 0.012		
MRK290	Galaxy	31.18	34.03	11.23	26.12	0.17	0.40 ± 0.012	-87.22 ± 9.39	3.16 ± 1.00	0.80 ± 0.074	3	0.030
3C263	QSO	28.60	6.89	4.56	-0.88	0.27	0.20 ± 0.012	-43.61 ± 9.43	1.77 ± 1.11	0.31 ± 0.062	3	0.065
PG0953+414	QSO	34.79	-19.21	15.98	-27.16	0.17	0.32 ± 0.0069	2.91 ± 6.43	2.41 ± 0.57	0.62 ± 0.046	<3	0.023
PG1351+640	Galaxy	32.06	20.48	8.98	12.60	0.15	0.400 ± 0.010	-87.22 ± 6.02	5.69 ± 2.08	0.78 ± 0.050	3	0.088
PKS1302-102	QSO	30.96	-0.35	82.57	-3.63	0.19	0.180 ± 0.0056	14.54 ± 3.55	-2.70 ± 0.87	0.27 ± 0.026	3	0.28
							0.14 ± 0.011	255.83 ± 5.95	0	0.46 ± 0.046		
MRK817	Galaxy	53.96	26.42	13.19	18.49	0.12	0.33 ± 0.0091	-52.33 ± 17.43	0.62 ± 0.49	0.53 ± 0.068	<3	0.031
MRK1383	Galaxy	68.096	22.97	74.24	18.84	0.14	0.32 ± 0.0068	-20.35 ± 3.47	2.26 ± 0.44	0.40 ± 0.024	<3	0.087
MRK153	Galaxy	44.99	-5.33	12.92	-13.26	0.14	0.17 ± 0.0096	14.54 ± 3.21	0	0.33 ± 0.024	3	0.0080
IZW92	Galaxy Pair	108.84	28.19	18.51	20.24	0.34	0.34 ± 0.025	-26.16 ± 26.04	1.26 ± 1.21	0.53 ± 0.15	<3	0.038
MRK421	Galaxy	130.60	-10.57	26.89	-18.40	0.12	0.270 ± 0.0058	-8.72 ± 7.02	1.87 ± 0.48	0.56 ± 0.046	<3	0.030
NGC4151	Galaxy	46.59	1.63	30.86	-6.08	0.13	0.170 ± 0.0077	11.63± 2.05	0	0.28 ± 0.016	3	0.0033
							0.072 ± 0.0070	148.27 ± 3.70	0	0.24 ± 0.031		
MR_2251-178	Galaxy	47.77	22.35	226.24	29.33	0.23	0.086 ± 0.014	-78.49 ± 4.19	0	0.14 ± 0.032	<3	0.064
							0.11 ± 0.023	0.00 ± 13.24	0	0.32 ± 0.10		

FAIRALL9	Galaxy	55.77	-17.10	194.06	-9.16	0.46	0.13 ± 0.025	43.61 ± 5.46	0	0.17 ± 0.045	<3	0.047
MRK586	Galaxy	49.47	-16.71	257.40	-12.92	0.19	0.17 ± 0.023	5.81 ± 8.52	0	0.42 ± 0.078	3	0.16
FAIR1116	Galaxy	61.02	-43.32	208.61	-35.56	0.23	0.088 ± 0.017	37.79 ± 3.84	0	0.12 ± 0.028	<3	0.059
MRK618	Galaxy	53.63	-55.86	247.28	-51.27	0.37	0.11 ± 0.020	17.44 ± 5.84	0	0.19 ± 0.044	4	0.036
MRK304	Galaxy	127.32	41.26	263.45	44.84	0.36	0.14 ± 0.034	8.72 ± 8.01	0	0.20 ± 0.059	4	0.066
MRK352	Galaxy	57.98	7.20	283.60	7.71	0.49	0.24 ± 0.043	-31.98 ± 15.83	0	0.55 ± 0.13	3	0.015
IRAS09149-62	Galaxy	121.84	-37.21	146.17	-32.39	0.17	0.47 ± 0.048	40.96± 5.27	0	0.37 ± 0.043	3	0.057
MRK10	Galaxy	58.01	-12.64	346.81	-19.57	0.60	0.15 ± 0.032	-16.32 ± 4.35	0	0.13 ± 0.032	4	0.029
MRK506	Galaxy	63.63	64.02	28.46	56.28	0.66	0.24 ± 0.047	-31.91 ± 6.27	0	0.19 ± 0.047	3	0.043
PG0838+770	Galaxy	58.49	4.00	347.50	-2.93	0.31	0.26 ± 0.025	-28.00± 5.41	0	0.34 ± 0.041	3	0.13
MRK487	Galaxy	112.71	35.37	13.80	27.43	0.67	0.23 ± 0.042	-3.14 ± 8.89	0	0.28 ± 0.065	<3	0.022
PG0947+396	QSO	71.53	-21.30	16.55	-29.25	0.59	0.35 ± 0.048	-2.68 ± 7.34	0	0.27 ± 0.057	<3	0.21
MKN142	Galaxy	88.46	-8.62	11.18	-16.54	0.52	0.38 ± 0.048	-10.92 ± 11.40	0	0.54 ± 0.085	<3	0.045
TON1187	Galaxy	100.10	-20.37	22.94	-28.27	0.57	0.22 ± 0.027	-29.07 ± 15.21	3.89 ± 0.089	0.40 ± 0.12	<3	0.080
RXJ135515+561244	Galaxy	75.78	21.36	16.67	13.41	0.45	0.26 ± 0.035	-2.91 ± 8.54	0	0.38 ± 0.064	<3	0.12
							0.25 ± 0.044	290.72 ± 18.25	0	0.64 ± 0.14		
PG1444+407	QSO	82.80	31.24	32.02	23.59	0.55	0.28 ± 0.043	-41.08 ± 10.49	0	0.39 ± 0.078	<3	0.27
MRK478	Galaxy	269.39	30.69	37.71	23.30	0.35	0.23 ± 0.024	-46.83 ± 6.08	0	0.34 ± 0.045	<3	0.079
PG1415+451	QSO	293.74	25.46	28.07	17.67	0.56	0.20 ± 0.033	-4.09 ± 7.16	0	0.25 ± 0.053	<3	0.11
PG1411+442	Galaxy	290.93	24.93	29.09	17.17	0.41	0.31 ± 0.029	-20.24 ± 5.63	0	0.35 ± 0.041	<3	0.090
NGC5548	Galaxy	238.97	25.07	48.89	18.40	0.38	0.23 ± 0.026	-62.25 ± 6.23	0	0.32 ± 0.046	<3	0.017
PG1402+261	Galaxy	293.11	22.31	47.95	15.56	0.43	0.38 ± 0.040	-16.57 ± 8.38	0	0.46 ± 0.046	<3	0.16
PHL2525	QSO	304.26	9.31	236.37	15.49	0.41	0.58 ± 0.033	-156.99± 21.18	2.56	0.91 ± 0.15	<3	0.20
I_ZW_1	Galaxy	255.04	3.75	264.27	6.83	0.34	0.13 ± 0.023	-5.79 ± 6.90	0	0.26 ± 0.053	4	0.059

PG1322+659	QSO	301.12	17.24	7.08	9.41	0.39	0.15 ± 0.025	-113.38 ± 7.13	0	0.25 ± 0.055	<3	0.17
							0.22 ± 0.027	23.26 ± 6.14	0	0.29 ± 0.047		
PG-1004+130	QSO	301.80	-34.52	46.13	-41.55	0.30	0.46 ± 0.028	-4.30 ± 4.50	0	0.49 ± 0.35	3	0.24
PG1553+113	QSO	327.56	46.25	65.58	41.32	0.20	0.26 ± 0.019	-11.63 ± 9.86	0	0.26 ± 0.026	3	0.36
NGC3516	Galaxy	186.76	7.30	357.22	-0.19	0.35	0.30 ± 0.021	5.11 ± 3.85	0	0.35 ± 0.028	<3	0.0088
PG1100+77	QSO	32.94	9.38	353.43	2.09	0.22	0.20 ± 0.031	-37.37 ± 7.57	0	0.37 ± 0.57	3	0.31

1) The FUSE designations are given for target names.

2) *Heliocentric velocities include the motion of the Sun through space*.

Table A.3: Target and OVI line information for contaminated OVI lines.

Target Name (1)	**Target Type**	**Supergalactic L (deg)**	**Supergalactic B (deg)**	**Sheet L (deg)**	**Sheet B (deg)**	**Noise (σ)**	**Equivalent Width (Å)**	**Heliocentric Velocity (km/s) (2)**	**Skew Parameter**	**FWHM (Å)**	**J**	**Target Redshift (z)**
TONS180	Galaxy	274.96	-6.44	229.72	0.23	0.18	0.061 ± 0.0054	270.37 ± 13.08	-6.57 ± 6.62	0.15 ± 0.033	<3	0.062
VIIZW118	Galaxy	27.78	-9.66	341.74	-16.21	0.167	0.20 ± 0.011	-23.26± 9.05	-0.86 ± 1.13	0.39 ± 0.12	4	0.080
PG1259+593	QSO	58.49	14.21	13.57	6.28	0.083	0.22 ± 0.0039	14.54 ± 13.16	-4.54 ± 0.87	0.57 ± 0.028	<3	0.48
3C273	QSO	112.71	-5.67	68.60	-10.63	0.12	0.38± 0.0072	8.72 ± 12.81	1.68 ± 0.27	0.45 ± 0.023	3	0.16
MKN59	Galaxy	82.80	9.70	37.51	2.27	0.15	0.18 ± 0.0094	-40.70± 4.13	1.16 ± 0.94	0.29 ± 0.067	<3	0.0026
TON28	QSO	72.19	-26.16	28.06	-33.9685	0.45	0.34 ± 0.040	34.09 ± 9.70	0	0.50 ± 0.072	<3	0.33
MRK734	Galaxy	97.95785	-18.53	54.87	-24.87	0.519	0.44 ± 0.041	35.05 ± 25.70	1.76 ± 1.49	0.62 ± 0.17	<3	0.050
PG1307+085	QSO	109.39	5.77	64.08	0.40	0.33	0.25 ± 0.023	-20.00 ± 4.83	0	0.32 ± 0.036	3	0.16
MRK54	Galaxy	85.08	8.75	39.80	1.44	0.44	0.16 ± 0.027	-21.61 ± 6.78	0	0.23 ± 0.050	<3	0.045
MRK79	Galaxy	34.79	-23.65	347.88	-30.68	0.45	0.19 ± 0.030	2.91 ± 0.94	1.26 ± 1.86	0.21 ± 0.092	4	0.022
PG1116+215	QSO	88.46	-15.42	44.71	-22.48	0.095	0.19 ± 0.0075	29.07± 14.01	0	0.35 ± 0.019	3	0.18
PG1211+143	Galaxy	100.10	-5.70	55.87	-11.90	0.18	0.15 ± 0.0066	34.89 ± 11.12	-3.45 ± 1.58	0.32 ± 0.042	3	0.081

T1247-232	Galaxy	138.96	-7.26	95.07	-8.94	0.42	0.51 ± 0.048	59.31 ± 13.74	0	0.86 ± 0.10	<3	0.048
HE0226-4110	Galaxy	258.03	-27.72	212.07	-20.07	0.097	0.20 ± 0.0084	5.81 ± 53.18	-4.88 ± 1.61	0.44 ± 0.030	<3	0.49
							0.12 ± 0.010	203.50 ± 7.55	-5.65 ± 3.52	0.50 ± 0.13		
IRAS_F22456-5125	Galaxy	238.94	6.04	193.87	13.98	0.25	0.48 ± 0.0091	212.22 ± 2.76	-2.15 ± 0.13	0.94 ± 0.18	3	0.10
NGC1068	Galaxy	304.26	-25.84	256.18	-21.98	0.12	0.15 ± 0.021	290.72 ± 1.60	0	0.58 ± 0.12	3	
2MASX-J21362313-6224008	Galaxy	223.99	5.74	178.58	13.30	0.18	0.33 ± 0.0096	40.70± 11.65	5.97 ± 2.05	0.58 ± 0.045	<3	0.0038
PKS0405-12	QSO	295.92	-49.34	244.33	-44.31	0.20	0.19 ± 0.0093	23.26 ± 8.09	4.02 ± 2.11	0.49 ± 0.070	3	0.57
PKS2005-489	QSO	219.67	23.38	173.10	30.70	0.14	0.46 ± 0.020	49.42± 2.40	-1.04 ± 0.51	0.58 ± 0.076	<3	0.071
MRK509	Galaxy	253.76	52.21	211.50	59.94	0.077	0.40 ± 0.013	313.98 ± 5.22	0.97 ± 0.42	0.55 ± 0.058	4	0.034
PKS0558-504	QSO	221.26	-53.52	179.31	-46.00	0.14	0.094 ± 0.0041	290.72 ± 12.23	0	0.30 ± 0.032	3	0.14
ESO265-G23	Galaxy	157.48	-27.76	116.54	-26.68	0.37	0.24 ± 0.034	90.12 ± 1.295	0	0.56 ± 0.090	3	0.057
							0.14 ± 0.020	276.18 ± 14.66	0	0.092 ± 0.014		
MRK1044	Galaxy	293.74	-25.19	246.17	-20.15	0.32	0.13 ± 0.023	360.49 ± 5.03	0	0.38 ± 0.087	<3	0.016
PG2349-014	QSO	290.93	14.84	247.85	19.94	0.35	0.16 ± 0.034	66.87 ± 0.60	0	0.44 ± 0.012	3	0.17
NGC7714	Galaxy	293.11	19.54	250.66	24.37	0.27	0.20 ± 0.028	58.14± 1.03	0	0.52 ± 0.13	3	0.0093
HE0238-1904	QSO	283.34	-29.49	235.78	-23.43	0.23	0.22 ± 0.036	20.35± 4.82	0	0.52 ± 0.14	3	0.63
							0.16 ± 0.025	206.41 ± 6.44	0	0.38 ± 0.090		

1) The FUSE designations are given for target names.

2) Heliocentric velocities include the motion of the Sun through space.

Table A.4: Target information for upper limit targets.

Target Name (1)	Target Type	Supergalactic L (deg)	Supergalactic B (deg)	Sheet L (deg)	Sheet B (deg)	Noise (σ)	Equivalent Width Upper Limit (Å)	Target Redshift (z)
RXJ010027-511346	Galaxy	246.431	-13.0261	201.3282	-5.10209	0.456876	0.139445	0.062
WPVS007	Galaxy	245.7364	-9.7822	200.6802	-1.8512	0.436358	0.133942	0.029
RXJ2241.8-4405	Galaxy	244.1738	11.01267	199.266	18.95525	0.452772	0.13835	0.55
NGC1399	Galaxy	262.546	-42.0774	215.419	-34.592	0.372016	0.116261	0.0048
Q0026+1259	QSO	307.6412	9.633385	264.0902	12.79196	0.406035	0.125691	0.14
EUVEJ0349-537	Galaxy	239.2114	-37.693	194.4355	-29.75	0.438865	0.134618	0.13
SBS0335-052	Galaxy	303.3307	-40.4556	252.9258	-36.3383	0.440459	0.135047	0.014
ESO31-8	Galaxy	222.2029	-24.458	178.1848	-16.9417	0.412912	0.127575	0.028
HE0450-2958	Galaxy	264.2836	-58.5482	215.3152	-51.0986	0.415885	0.128387	0.25
PG0052+251	QSO	321.0341	6.708157	277.0537	8.117694	0.345628	0.108819	0.15
IRASL06229-6434	Galaxy	210.9565	-40.8006	168.9286	-33.8625	0.493594	0.149134	0.13
HE1115-1735	Galaxy	128.7752	-27.3092	87.8534	-30.1544	0.386625	0.120333	0.22
PG1626+554	Galaxy	53.40234	41.3722	9.242043	33.49754	0.488875	0.1479	0.13
1H0707-495	Galaxy	202.4785	-56.0428	163.6778	-49.6114	0.323249	0.102418	0.041
TON1480	QSO	81.98783	0.496225	37.14402	-6.96019	0.63196	0.183889	0.62
IR07546+3928	Galaxy	40.9459	-33.0191	353.7311	-40.3983	0.53656	0.160218	0.096
AKN564	Galaxy	322.0737	36.20375	282.9644	37.13687	0.463777	0.141282	0.025

1) The FUSE designations are given for target names.

Appendix B

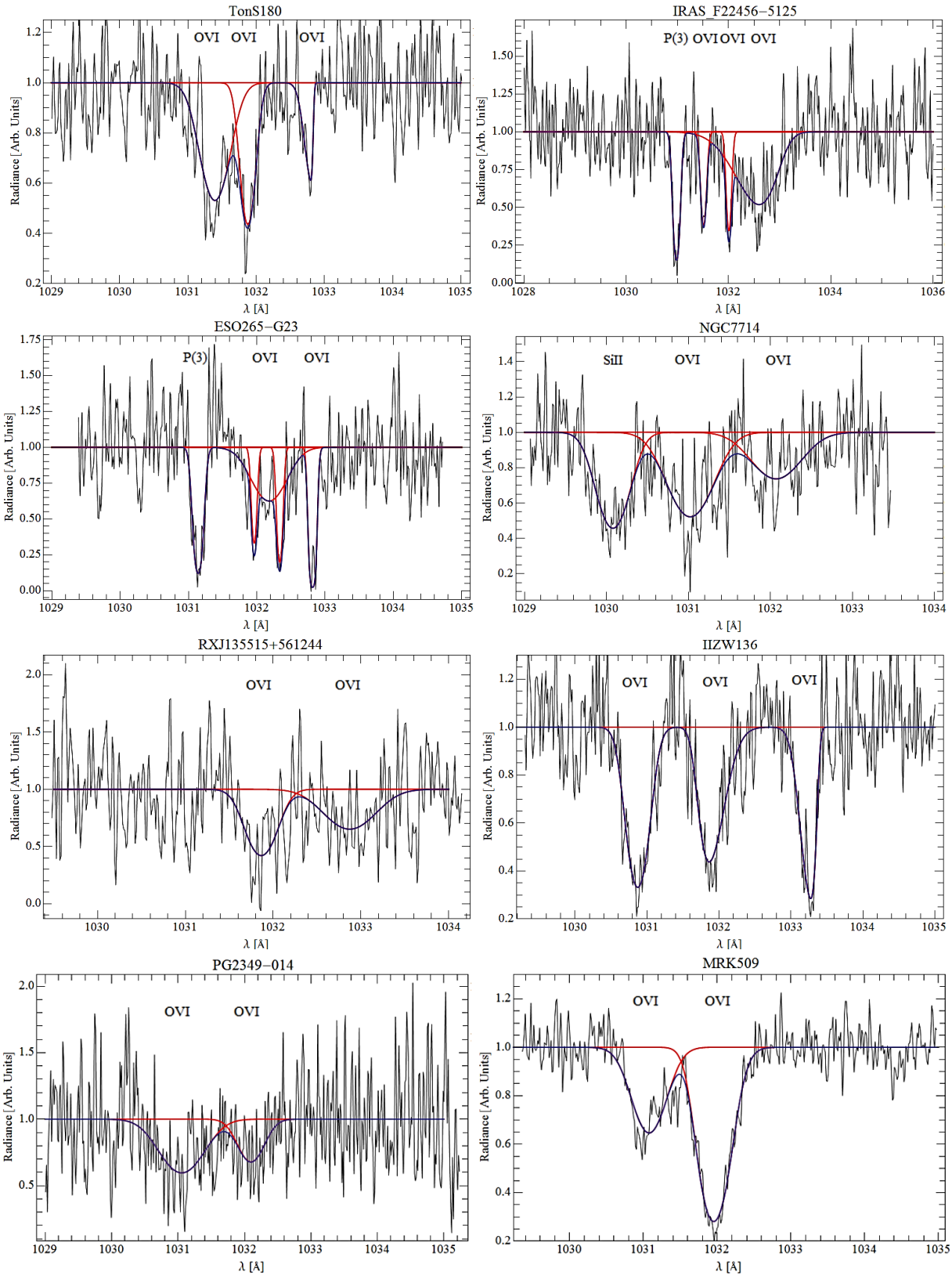
TonS180
OVI OVI OVI
IRAS_F22456−5125
P(3) OVI OVI OVI
ESO265−G23
P(3) OVI OVI
NGC7714
SiII OVI OVI
RXJ135515+561244
OVI OVI
IIZW136
OVI OVI OVI
PG2349−014
OVI OVI
MRK509
OVI OVI
Radiance [Arb. Units]
λ [Å]

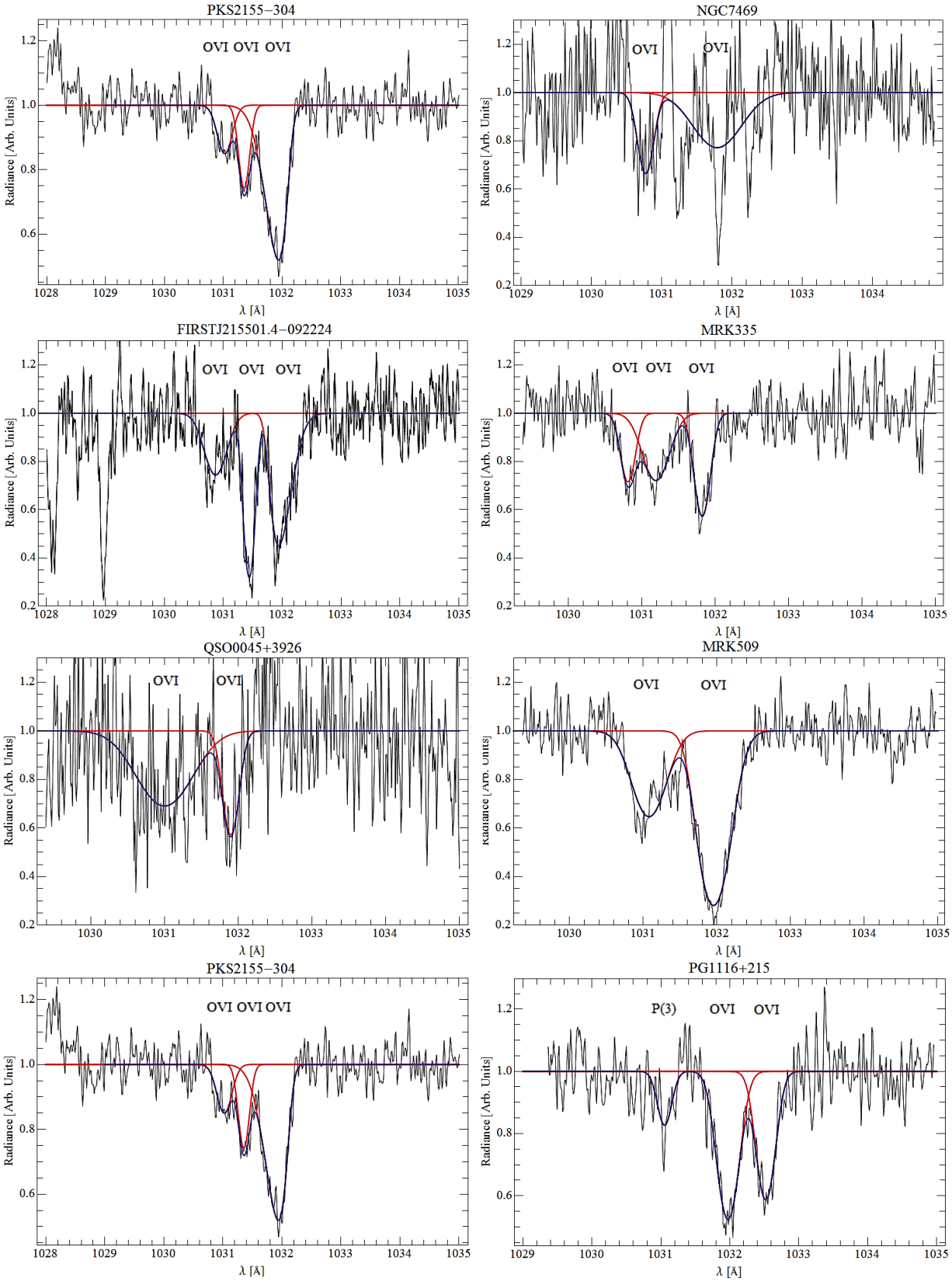
PKS2155−304
OVI OVI OVI
NGC7469
OVI
OVI
FIRSTJ215501.4−092224
OVI OVI OVI
MRK335
OVI OVI OVI
QSO0045+3926
OVI
OVI
MRK509
OVI
OVI
PKS2155−304
OVI OVI OVI
PG1116+215
P(3)
OVI
OVI
Radiance [Arb. Units]
λ [Å]

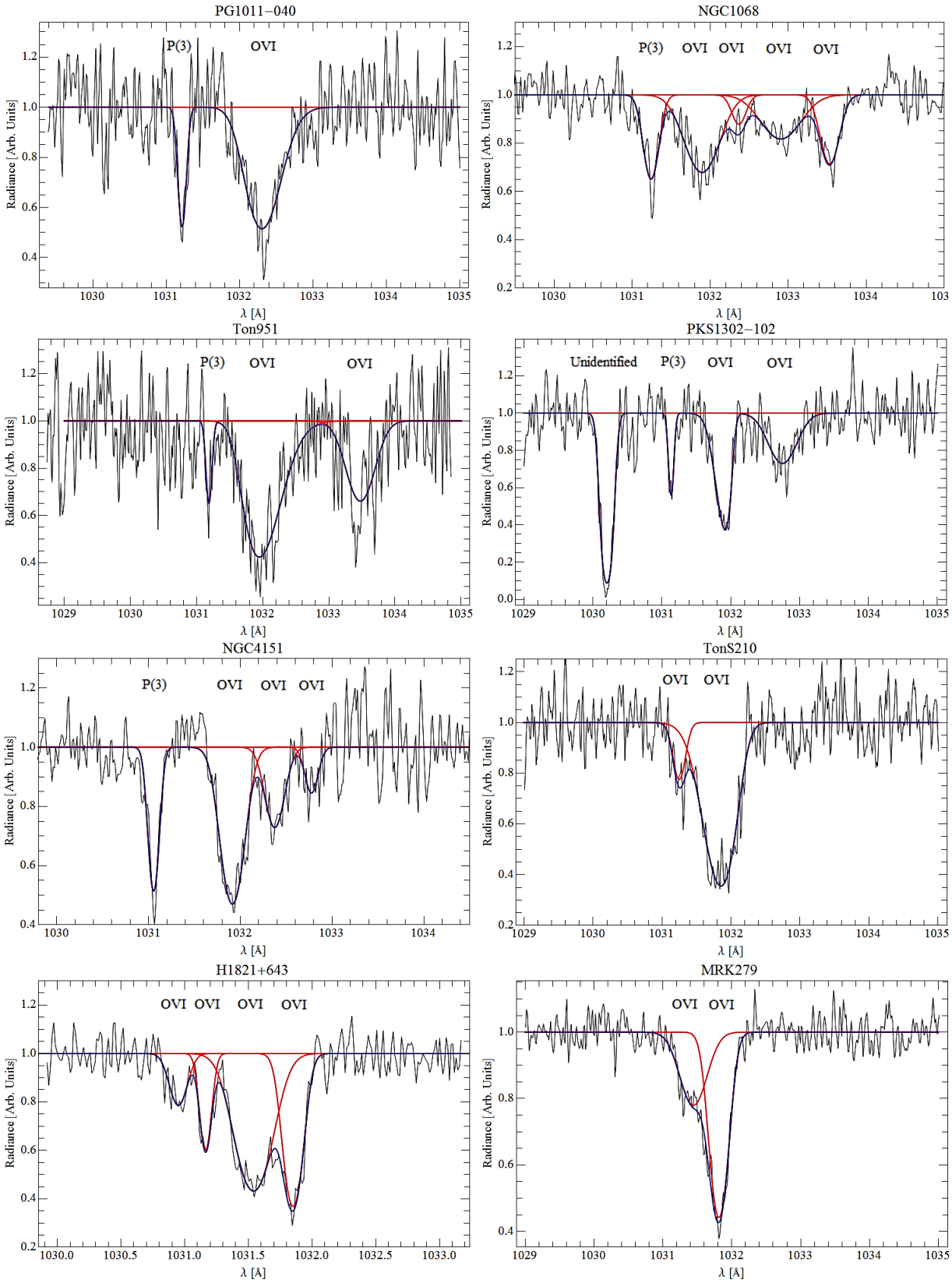
PG1011−040
P(3)
OVI
NGC1068
P(3)
OVI
OVI
OVI
OVI
Ton951
P(3)
OVI
OVI
PKS1302−102
Unidentified
P(3)
OVI
OVI
NGC4151
P(3)
OVI
OVI
OVI
TonS210
OVI
OVI
H1821+643
OVI
OVI
OVI
OVI
MRK279
OVI
OVI
Radiance [Arb. Units]
λ [Å]

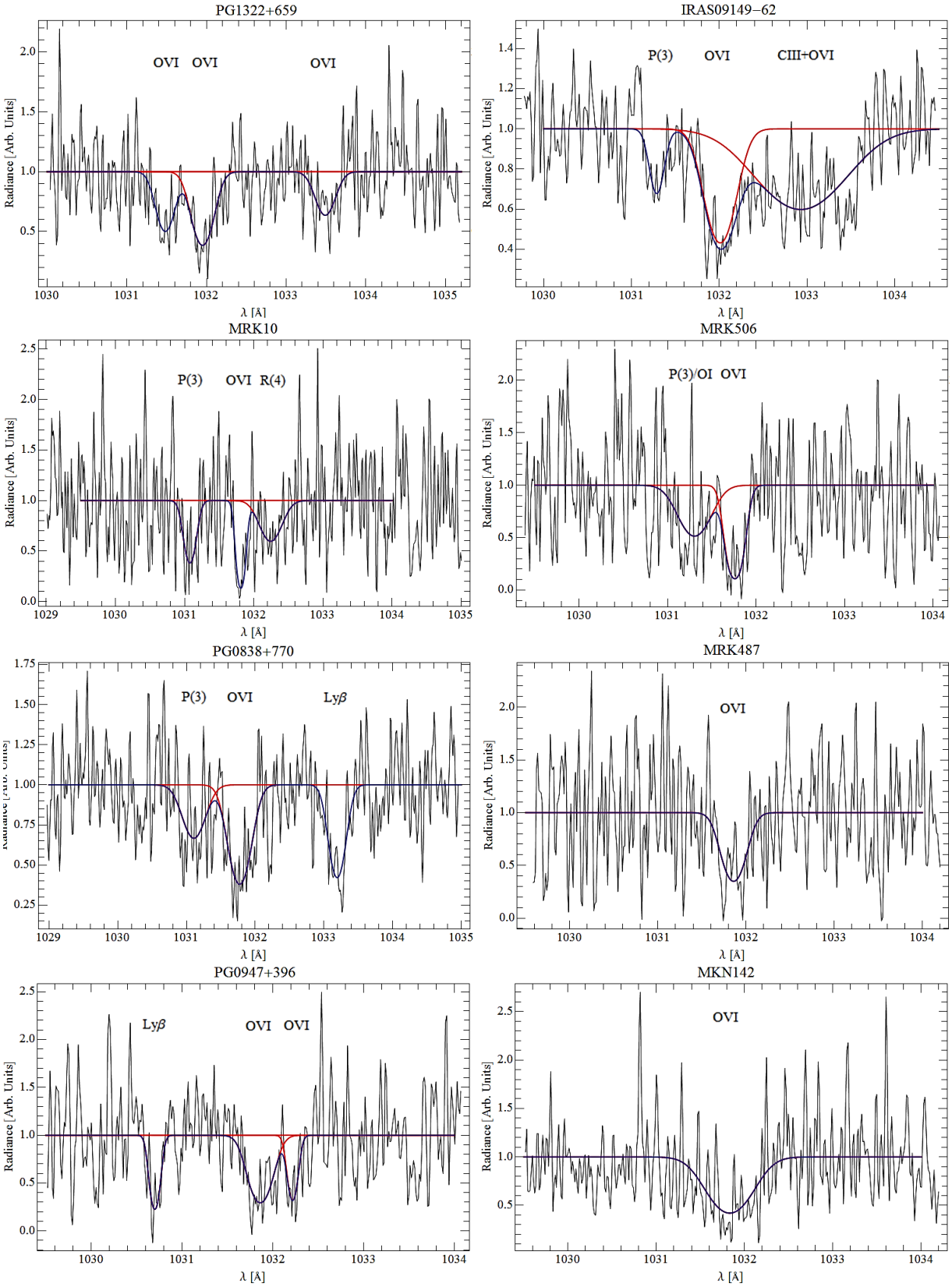
PG1322+659
OVI OVI OVI
IRAS09149−62
P(3) OVI CIII+OVI
MRK10
P(3) OVI R(4)
MRK506
P(3)/OI OVI
PG0838+770
P(3) OVI Lyβ
MRK487
OVI
PG0947+396
Lyβ OVI OVI
MKN142
OVI
Radiance [Arb. Units]
λ [Å]

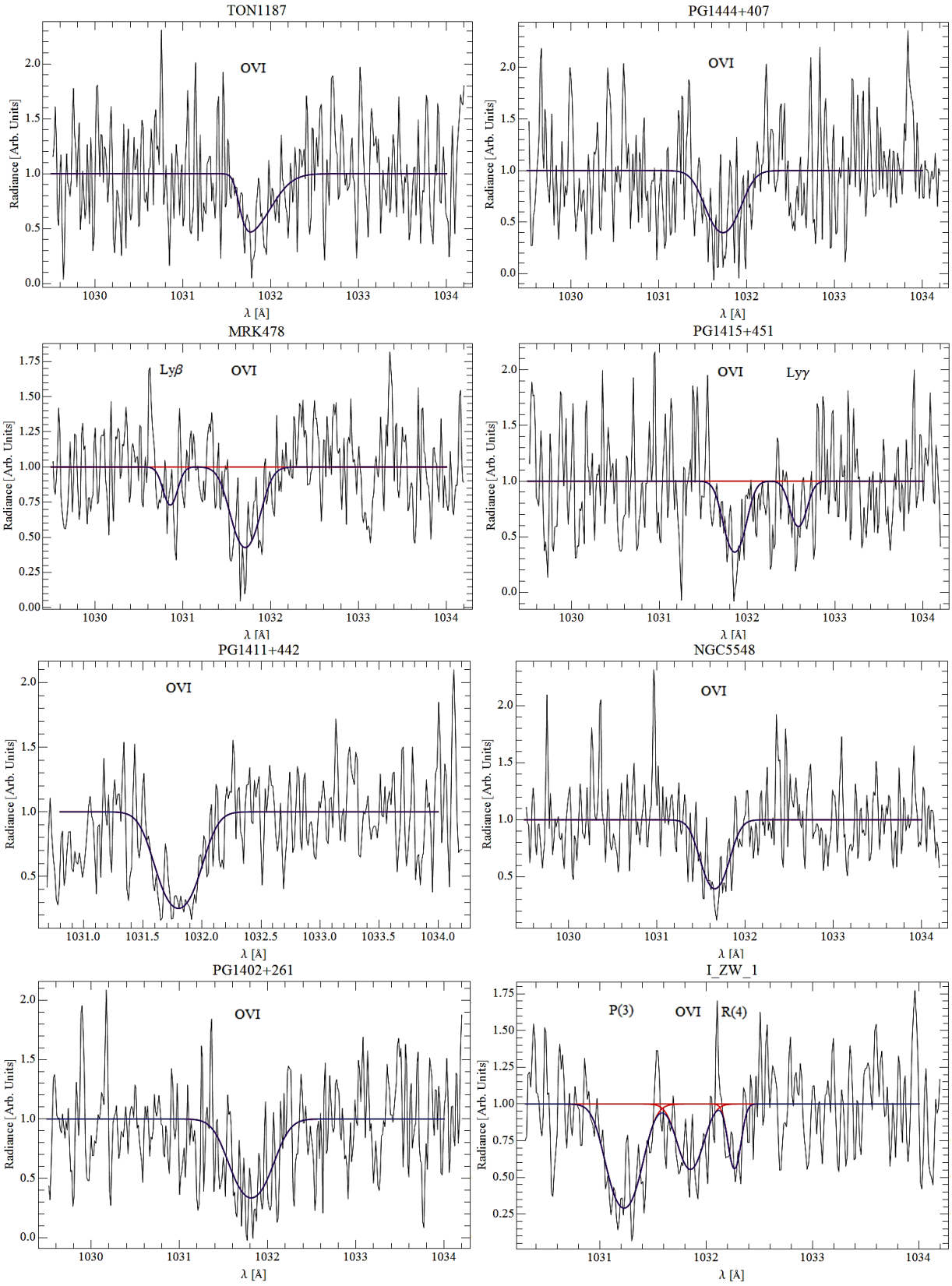
TON1187
OVI
PG1444+407
OVI
MRK478
Lyβ
OVI
PG1415+451
OVI
Lyγ
PG1411+442
OVI
NGC5548
OVI
PG1402+261
OVI
I_ZW_1
P(3)
OVI
R(4)
Radiance [Arb. Units]
λ [Å]

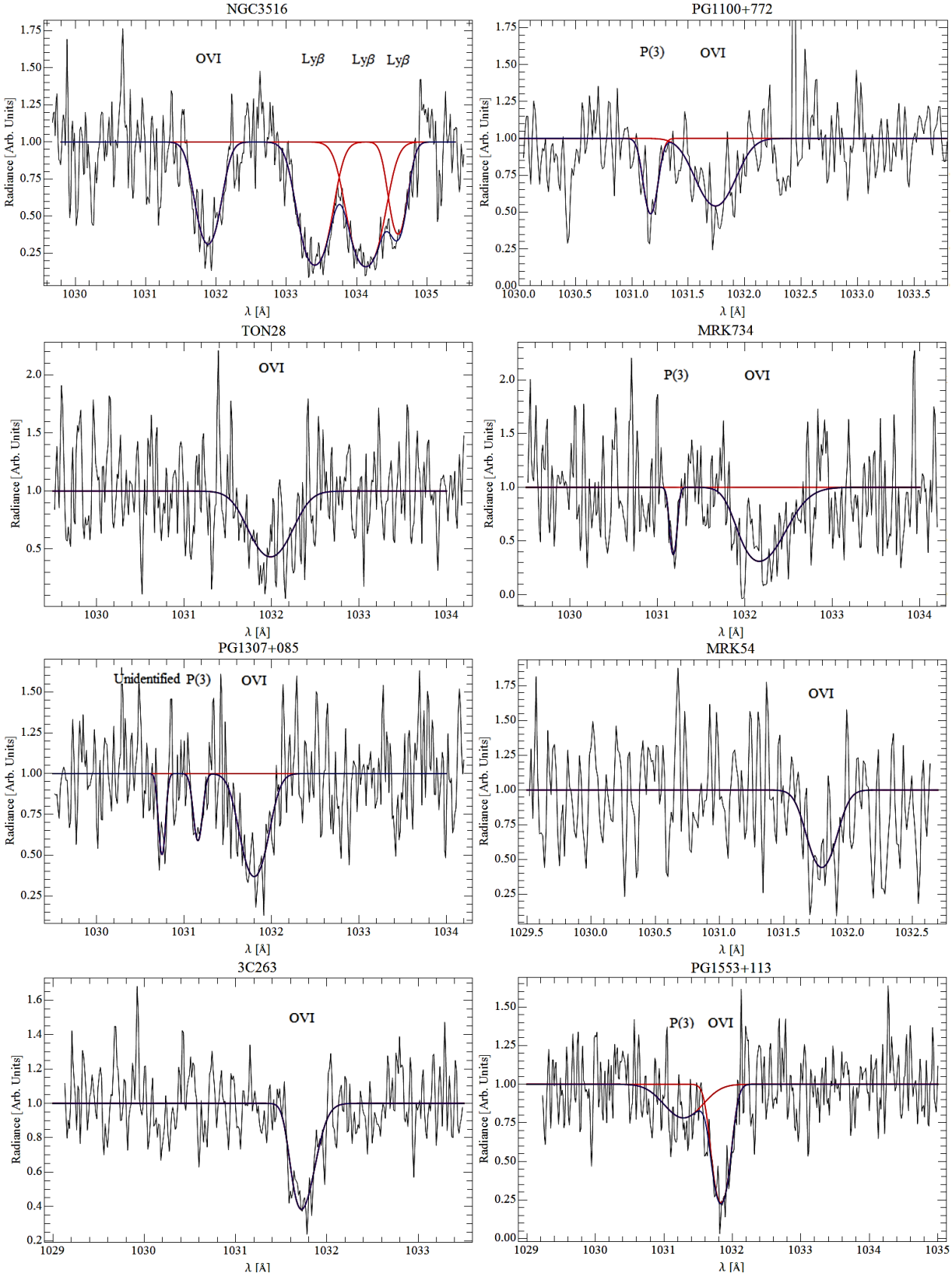
NGC3516
OVI
Lyβ
Lyβ
Lyβ
PG1100+772
P(3)
OVI
TON28
OVI
MRK734
P(3)
OVI
PG1307+085
Unidentified P(3)
OVI
MRK54
OVI
3C263
OVI
PG1553+113
P(3)
OVI
Radiance [Arb. Units]
λ [Å]

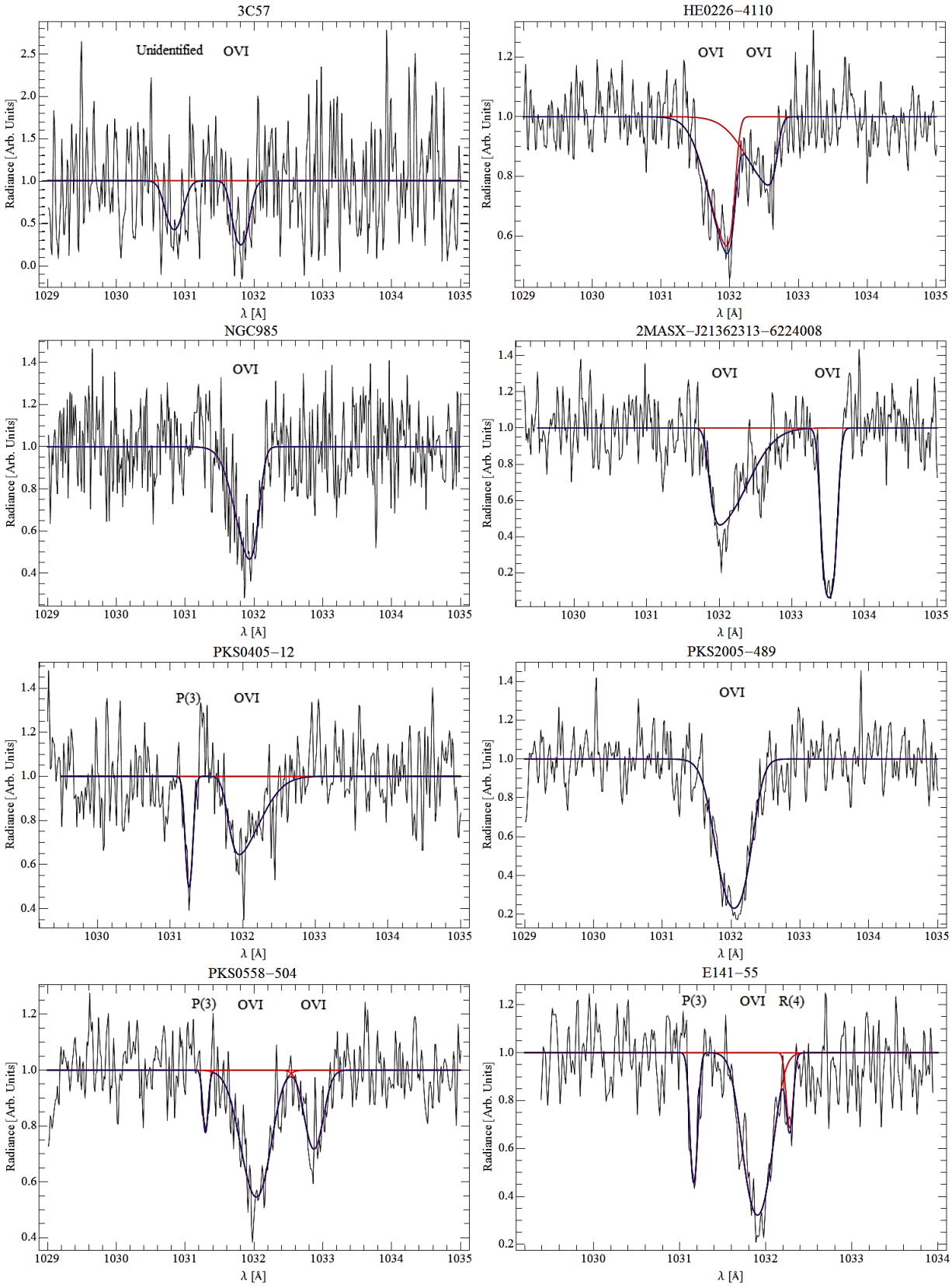
3C57
Unidentified
OVI
HE0226−4110
OVI
OVI
NGC985
OVI
2MASX−J21362313−6224008
OVI
OVI
PKS0405−12
P(3)
OVI
PKS2005−489
OVI
PKS0558−504
P(3)
OVI
OVI
E141−55
P(3)
OVI
R(4)
Radiance [Arb. Units]
λ [Å]

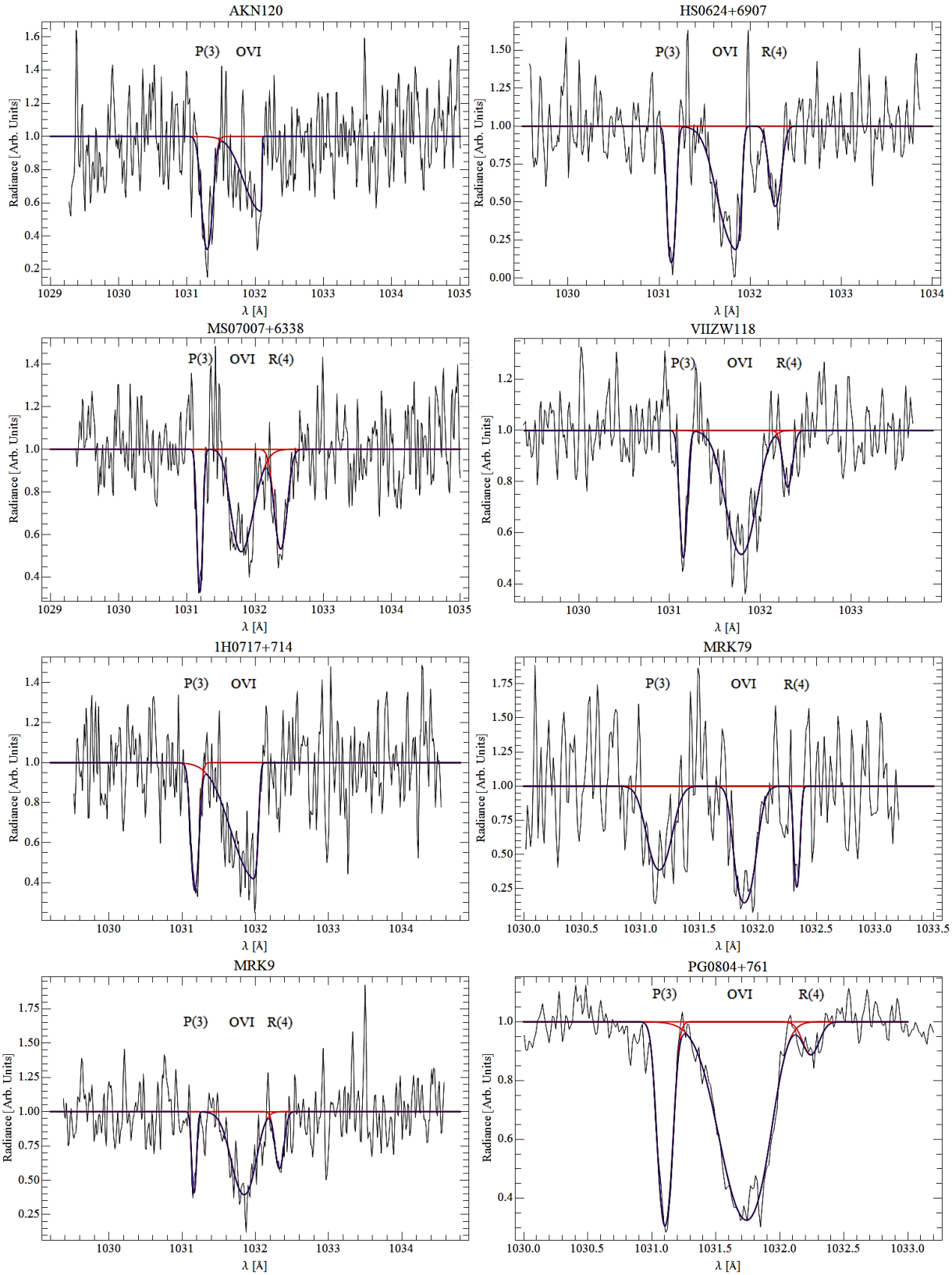
AKN120
P(3) OVI
HS0624+6907
P(3) OVI R(4)
MS07007+6338
P(3) OVI R(4)
VIIZW118
P(3) OVI R(4)
1H0717+714
P(3) OVI
MRK79
P(3) OVI R(4)
MRK9
P(3) OVI R(4)
PG0804+761
P(3) OVI R(4)
Radiance [Arb. Units]
λ [Å]

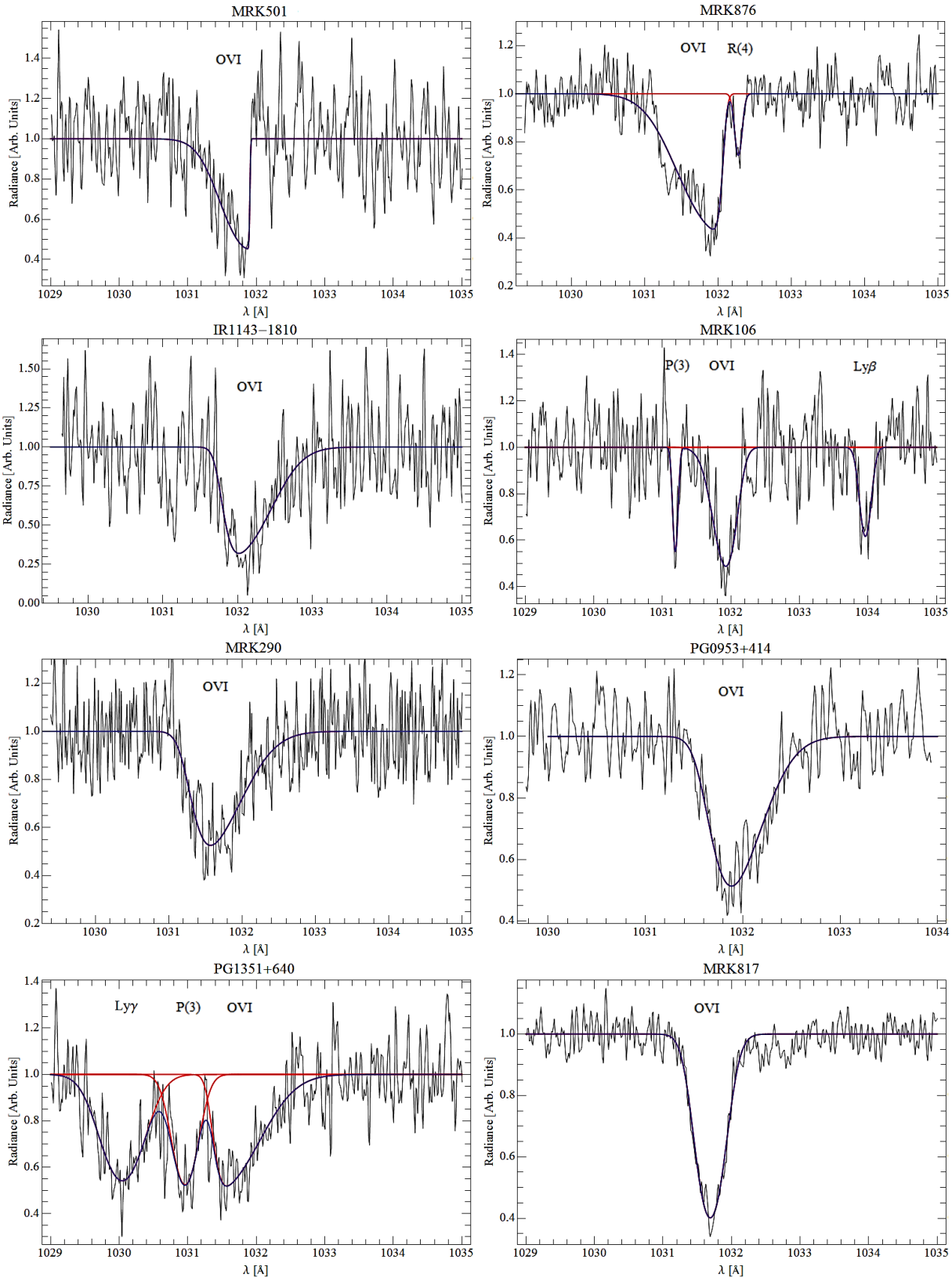
MRK501
OVI
MRK876
OVI R(4)
IR1143−1810
OVI
MRK106
P(3) OVI Lyβ
MRK290
OVI
PG0953+414
OVI
PG1351+640
Lyγ P(3) OVI
MRK817
OVI
Radiance [Arb. Units]
λ [Å]

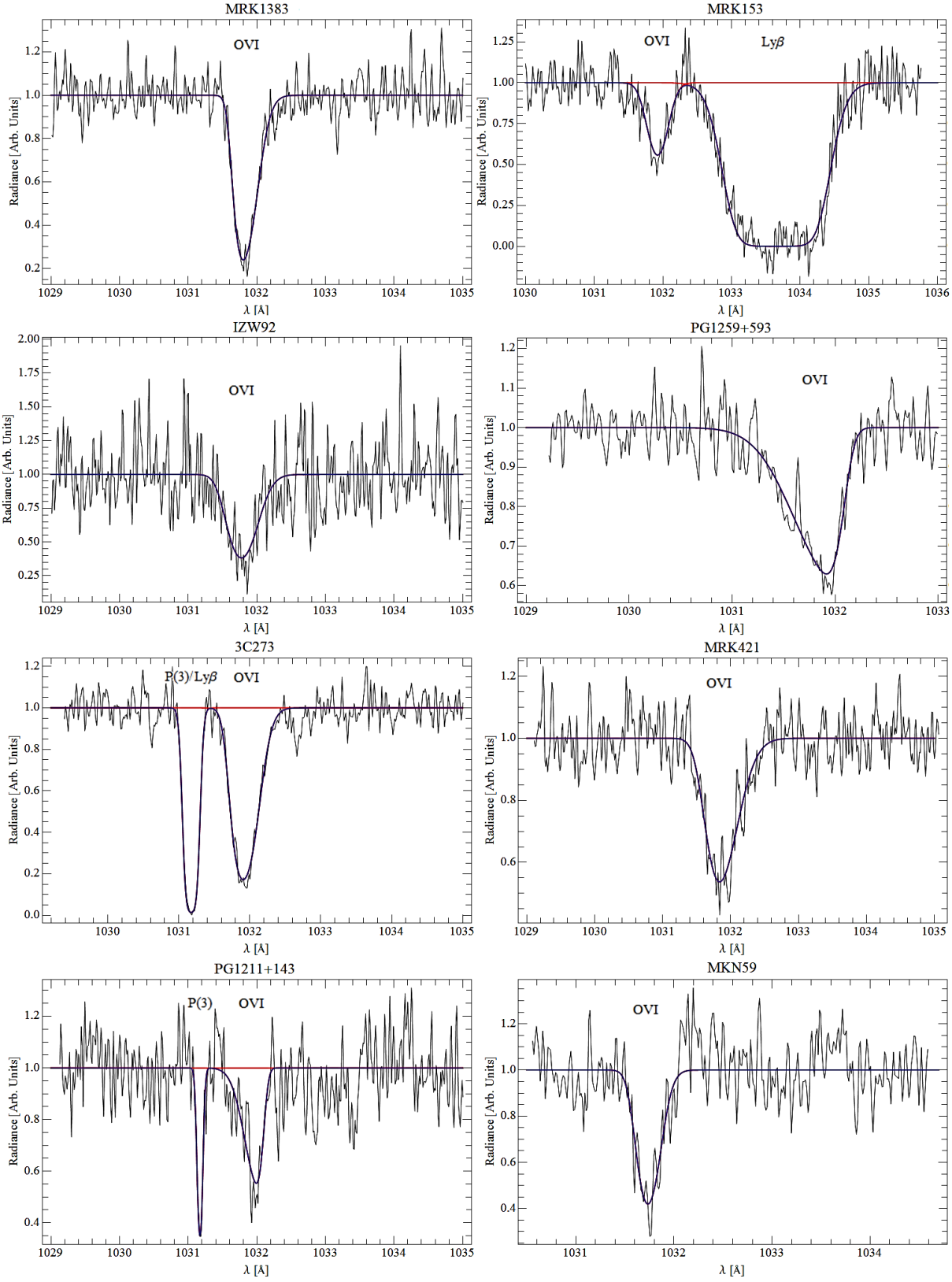
MRK1383
OVI
MRK153
OVI
Lyβ
IZW92
OVI
PG1259+593
OVI
3C273
P(3)/Lyβ
OVI
MRK421
OVI
PG1211+143
P(3)
OVI
MKN59
OVI
Radiance [Arb. Units]
λ [Å]

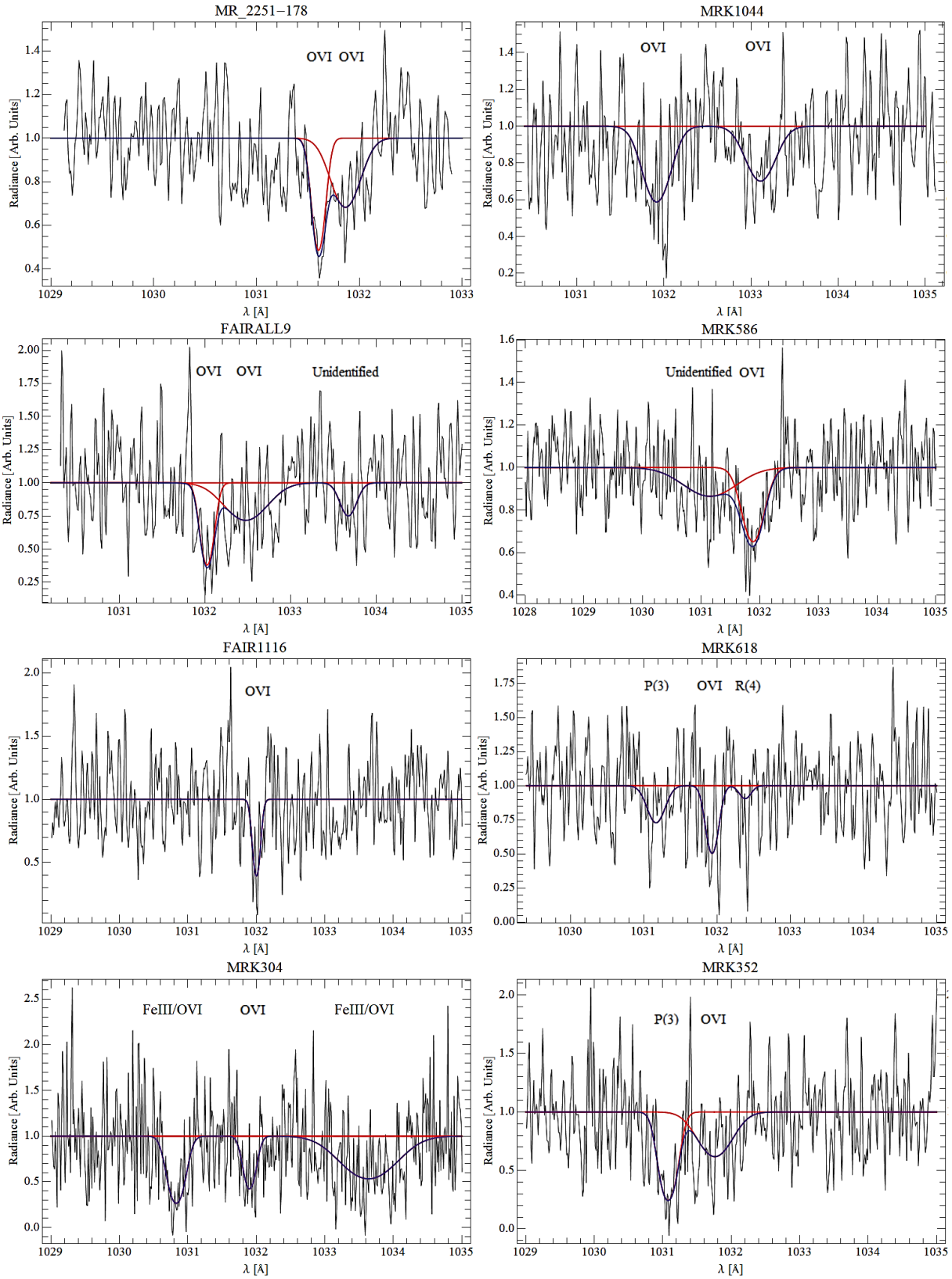
MR_2251−178
OVI OVI
MRK1044
OVI
OVI
FAIRALL9
OVI OVI
Unidentified
MRK586
Unidentified OVI
FAIR1116
OVI
MRK618
P(3) OVI R(4)
MRK304
FeIII/OVI
OVI
FeIII/OVI
MRK352
P(3) OVI
Radiance [Arb. Units]
λ [Å]

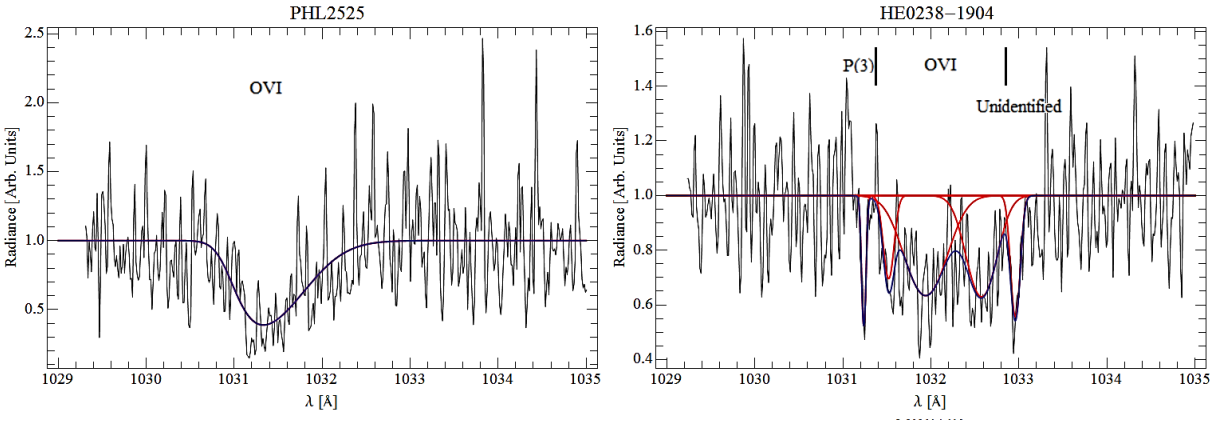

Figure B.1: 90 targets with identified OVI absorption lines. The wavelengths displayed in these spectra are those seen in the heliocentric reference frame, without the removal of the relative motions of the Sun through space.